論文 / 著書情報
Article / Book Information

題目(和文)	
Title(English)	Study on Control of Chemical Durability and Electrical Properties of Ag Thick-Film Conductors Containing Borosilicate or Tellurite Glass Frits
著者(和文)	橘勇介
Author(English)	Yusuke Tachibana
出典(和文)	学位:博士（工学）, 学位授与機関:東京工業大学, 報告番号:甲第11774号, 授与年月日:2022年3月26日, 学位の種別:課程博士, 審査員:吉本 護,舟窪 浩,北本 仁孝,和田 裕之,松田 晃史
Citation(English)	Degree:Doctor (Engineering), Conferring organization: Tokyo Institute of Technology, Report number:甲第11774号, Conferred date:2022/3/26, Degree Type:Course doctor, Examiner:,,,,
学位種別(和文)	博士論文
Type(English)	Doctoral Thesis

Doctoral Thesis

Study on Control of Chemical Durability and Electrical Properties of Ag Thick-Film Conductors Containing Borosilicate or Tellurite Glass Frits

Tokyo Institute of Technology
School of Materials and Chemical Technology

March 2022

Yusuke Tachibana

Contents

List of Tables

Chapter 1

Chapter 3

Chapter 4

Chapter 5

List of Figures

Chapter 1

Chapter 2

Chapter 3

Chapter 4

Chapter 5

Chapter 1

General Introduction

1.1. History and Significance of Thick-Film Conductors

Over the past 50 years, thick-film materials, which are viscus pastes produced by mixing and dispersing glass frits, metal powders, and/or metal oxides with an organic vehicle, have been used as thick-film conductors, resistors, dielectrics, and insulators for electric circuits. Organic materials in the thick-film paste are collectively referred to as an organic vehicle because it works as a carrier to transport the functional materials to substrates in the thick-film formation process [1–4]. The thick film is generally formed by printing the paste onto the substrate through a finely-woven screen with an etched pattern of desired geometry and annealing the printed pattern [1–4].

The Pt/Au thick-film conductor was used as a solderable material in initial microcircuits [2,5]. Since the solder leach resistance of Pt in the Sn/Pb solder and the solder wettability of Au were high, excellent solder adhesion was obtained [2]. The Pt/Au thick-film conductor was actually used for the hybrid integrated circuit in the 360 computer produced by International Business Machines Corporation in 1960s, which attracted a great deal of attention and made thick-film technology popular [5,6]. To reduce the cost, Pd/Au and high Pd content Pd/Ag thick-film conductor were focused on in the early 1970s [2,5]. However, the adhesion of soldered thick-film conductors containing Ag was found to decrease significantly after storage at 125°C or higher temperature. There are some reports about the failure mechanism. The interdiffusion of solder and Ag formed intermetallics (e.g., Ag_3Sn and Ag_5Sn), as a result, the volume change associated with the formation disrupted the glass-bond between the thick-film conductor and substrate [5]. The adhesion degradation was related to Sn mobility along the glass and metal surface phases, and the formation of intermetallic compounds made gradual fracture of the glass-bond on the substrate [5]. Sn from the Sn/Pb solder was found to have replaced the Ag at the interface of Ag and glass phases, and the diffusion of Sn was related to the porosity of the thick-film conductor. [5,7]. On the other hand, it is reported that Ag alloys with 10–30% Pd reduced the risk of solder leaching of Ag [4,8].

In initial thick-film conductors, only glass was used as a binder, but the addition of metal oxide to the glass binder, referred to as a mixed binder, was started to report from the middle of 1970s. For example, CuO reacted with the Al_2O_3 substrate and formed $CuAlO_2$

and $CuAl_2O_4$ which were the driving force for the interaction of the binder and substrate at high temperature [2,4,5]. Since Bi_2O_3-Al_2O_3 eutectic temperature was 820°C and the transient liquid was formed, Bi_2O_3 wetted the metal surface and improved the efficiency of the glass binder on the Al_2O_3 substrate above the eutectic temperature [2,4,8]. In addition, there is a report that Bi_2O_3 could be reduced to Bi metal by the Sn/Pb solder, which made good solder wettability during the soldering process [5].

In addition to the adhesion and solder leach resistance, Ag migration resistance was gradually focused on. There have been numerous reports on the Ag migration mechanism, and it is known that the Ag migration effectively improved as increasing the ratio of Pd to Ag since Pd formed a barrier layer at the conductor surface and slowed down silver dendrite formation [4,5,8]. However, recently, the concerns of Ag migration became low since the risk can be minimized by the proper circuit layout, encapsulation, and fabrication process of electronic components and circuits, as a result, low Pd content Pd/Ag and Ag thick-film conductor became major solderable thick-film conductors.

Cu thick-film conductors have attracted a great deal of attention since 1970s because of the low cost, high migration and solder leach resistance in compared to Ag [8]. However, Cu is easily oxidized in air so it needs to be fired under inert gas (e.g., N_2) [8]. In addition, the organic vehicle can become the strong reducing agent during the firing process, and it causes the problem. For example, PbO_2 and Bi_2O_3 in the Cu conductor paste were reduced by the decomposed organic vehicle, which caused weak adhesion to the substrate [8]. Since Cu thick-film conductors are not easy handling, those are not widely used in compared to Ag thick-film conductors.

Au thick-film conductors are generally non-solderable because of rapid dissolution in solders, and those have been historically connected to electronic components and circuits by the wire bonding techniques: the thermocompression bonding of Au wire and the ultrasonic bonding of Al wire [1–4]. Since the corrosion resistance of Au is high, Au thick-film conductors have been used for high reliability applications (e.g., space devise) from the early stage of thick-film history.

The subsequent sections of Chapter 1 present the general background of thick-film conductors including the electrical properties, chemical durability, circuit formation process, substrates, glass frits in thick-film conductors, and market, and the purpose of this study.

1.2. Thick-Film Conductors Containing Glass Frits

1.2.1. General Electrical and Magnetic Properties

Substances are classified to insulator, semiconductor, and conductor by resistivity (ρ) with a unit of Ω·cm or conductivity (σ) with a unit of S/cm which is the reciprocal of resistivity. There is no clear definition but the substance of which resistivity is approximately higher than 10^{10} Ω·cm is insulator, whereas that of which resistivity is lower than approximately 10^{-4} Ω·cm is conductor [9]. The resistivity of semiconductor is between these values. **Figure 1-1** illustrates the comparison of the band structure of insulator, semiconductor, and conductor. In a band theory, the band gap of the insulator between the top level of the valence band and the bottom of the conduction band is high, and the electrons in the valence band basically cannot move to the conduction band. On the other hand, the band gap of the semiconductor is small, and the electrons in the valence band can jump to the conduction band when applying small energy. The valance band and conduction band of the conductor are overlapped, and the Fermi level is within the bands. Therefore, the electrons in the valence band become free electrons, and the electrons flow from the valence band to the conduction band easily, as a result, the resistivity of the conductor is very low.

Dielectric belongs in insulator, but it possesses polarization behavior. The behavior of dielectric polarization in response to an external electric field can be illustrated using a capacitor model, as shown in **Fig. 1-2**. In the absence of the electric field, the electric dipoles are oriented randomly, as shown in **Fig. 1-2(a)**. However, when the dielectric is placed in the electric field, polar molecules partially aligned with the electrical field, and relative positive charges are directed towards the electric field, and negative charges shift in the opposite direction, as shown in **Fig. 1-2(b)**. As a result, the opposite charges on adjacent dipoles neutralize each other, and there is no net charge within the dielectric, whereas a net charge is generated on the dielectric surface, as shown **Fig. 1-2(c)**. This polarization property is expressed by physical quantity called permittivity. The permittivity of dielectric is high, whereas that of insulator relatively low. Both dielectric and insulator do not allow the flow of electron under direct current but the dielectric allows it under alternating current due to the high polarization [12]. The dielectric polarization starts from: 1) distortion of the negatively-charged electron cloud against the positively-charged nuclei, 2) displacement of cations and anions, or 3) orientation of permanent dipoles [10,12,13]. The dielectrics which get polarized only in the presence of the electric field are referred to as paraelectric. The dielectrics except paraelectric are generally classified to piezoelectric, pyroelectric, and ferroelectric. Pyroelectric is a part of piezoelectric, and ferroelectric is included in pyroelectric, as illustrated in **Fig. 1-3**. Piezoelectric does not have the center of symmetry in the crystal structure, and the dielectric polarization happens by the asymmetric displacement of ion [12,13]. It possesses the property of converting mechanical energy generated by the applied external stress and deformation in the crystal into electrical energy [12,13]. Pyroelectric is spontaneously polarized but the surface is neutralized by adsorbed ions or molecules [12,13]. However, the polarization charge appears when it is heated or cooled [12,13]. Ferroelectric exhibits the spontaneous polarization switchable by the external electric field [12,13]. **Figure 1-4** shows the relationship between the electric field and dielectric polarization of paraelectric and ferroelectric. The dielectric polarization of paraelectric increases as increasing the electric field, and it follows the same path when decreasing the electric field. The polarization of ferroelectric is affected by the history of the applied electric field, and it will trace out a loop called hysteresis loop due to the existent of domain which has different polarization directions.

Physical properties of dielectric are affected by the electric dipole, whereas those of magnetic are affected by the magnetic dipole. Dielectric and magnetic have a lot in common. The electric dipole, dielectric polarization, permittivity, electric susceptibility, and electric displacement of dielectric are corresponding to the magnetic dipole, magnetization, permeability, magnetic susceptibility, and magnetic flux density of magnetic. The relationship between these physical quantities is also close. For example, the electric displacement ($\boldsymbol{D}$) is expressed by [12,13]

$$\boldsymbol{D} = \varepsilon_0(1 + \chi_\mathrm{e})\boldsymbol{E}, \tag{1-1}$$

where ε_0 is a dielectric constant of vacuum, χ_e is the electric susceptibility, and $\boldsymbol{E}$ is the electric field. On the other hand, the magnetic flux density ($\boldsymbol{B}$) is expressed by [13]

$$\boldsymbol{B} = \mu_0(1 + \chi_\mathrm{m})\boldsymbol{H}, \tag{1-2}$$

where μ_0 is a magnetic constant of vacuum, χ_m is the magnetic susceptibility, and $\boldsymbol{H}$ is the magnetic field. Substances on the basis of magnetism are generally classified to paramagnetic, diamagnetic, and ferromagnetic. The difference is mainly caused by the interaction of unpaired electrons, as illustrated in **Fig. 1-5**. Paramagnetic has some unpaired electrons, and those are randomly arranged. The magnetization of paramagnetic is weak and parallel to the direction of the applied external magnetic field. Diamagnetic does not have unpaired electrons. The magnetization of diamagnetic is very weak and is opposite to the direction of the applied magnetic field. Ferromagnetic has unpaired electrons, and those are all aligned. The magnetization of ferromagnetic is strong and parallel to the direction of the applied external magnetic field. **Figure 1-6** shows the relationship between the magnetic field and magnetization of paramagnetic, diamagnetic, and ferromagnetic. The magnetization of paramagnetic increases, and that of diamagnetic decreases as increasing the magnetic field, and each magnetization follows the same path when decreasing the magnetic field. The magnetic properties of paramagnetic and diamagnetic disappear when the magnetic field is removed. On the other hand, those of ferromagnetic are retained even after removing the magnetic field. The magnetization of ferromagnetic is affected by the history of the applied magnetic field, and it will trace out a loop called hysteresis loop due to the existence of magnetic domains.

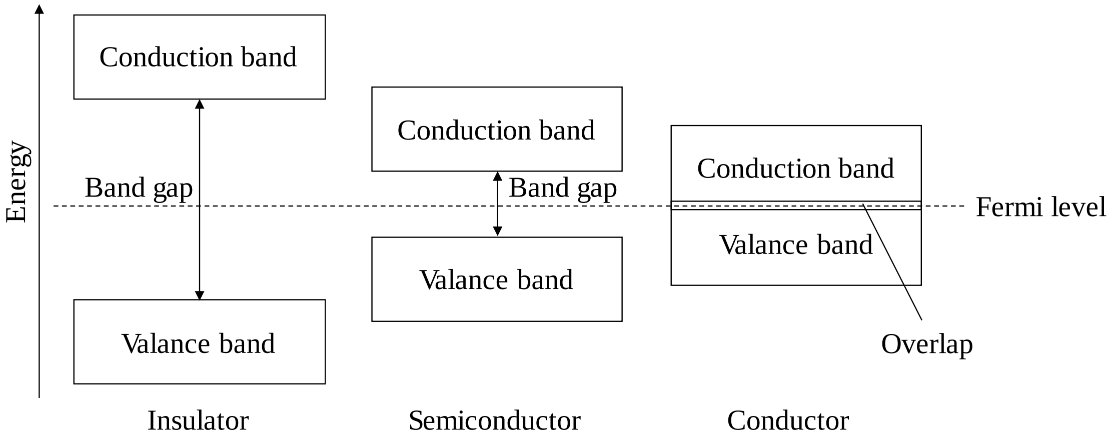

Figure 1-1. Band structure of insulator, semiconductor, and conductor [9].

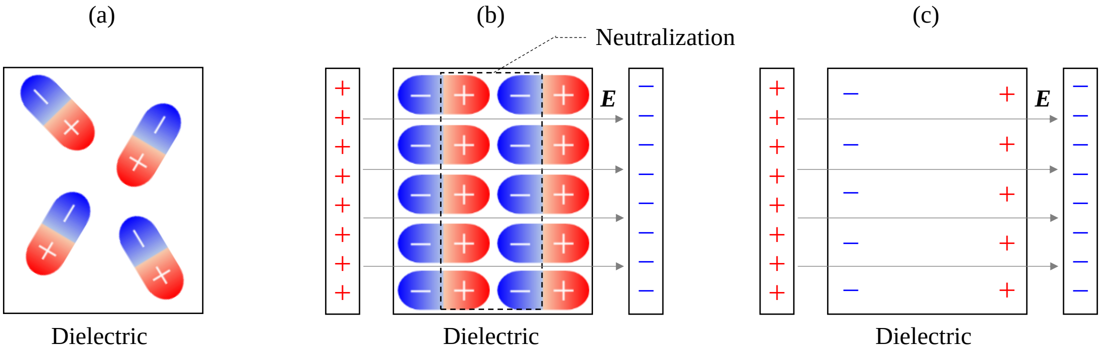

Figure 1-2. Schematic depiction of dielectric polarization using parallel-plate capacitor model: dielectric (a) in the absence and (b) in the presence of an electric field, and (c) resulting charge on the surface of dielectric [10–12]. (***E***: electric field)

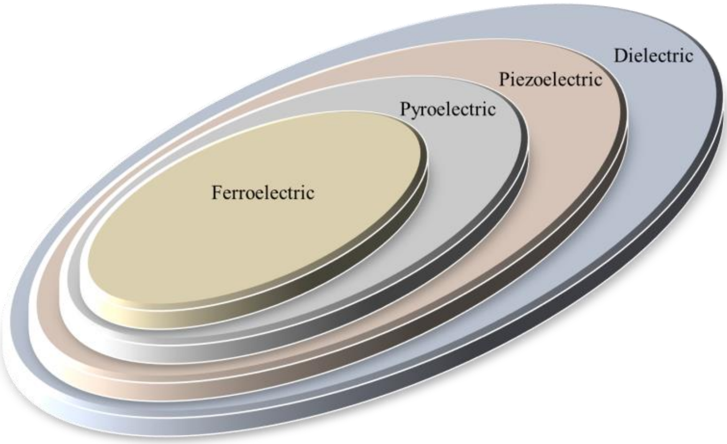

Figure 1-3. Relationship between piezoelectric, pyroelectric, and ferroelectric in dielectric [12,13].

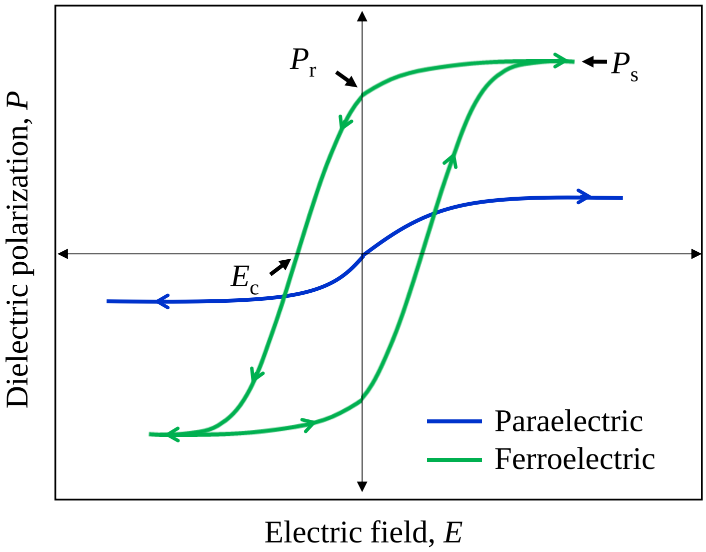

Figure 1-4. Representative dielectric polarization behavior of paraelectric and ferroelectric when an external electric field is applied [12,13]. (E_c: coercive field, P_r: remanent polarization, P_s: spontaneous polarization)

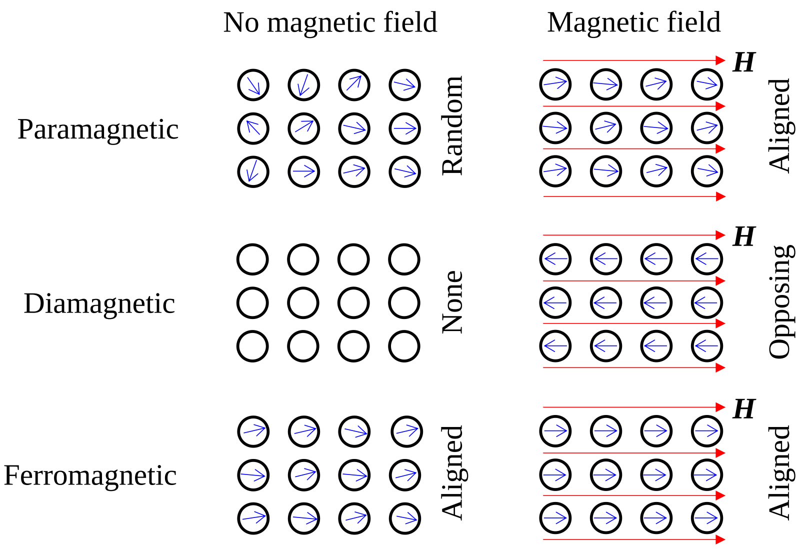

Figure 1-5. Schematic depiction of magnetic dipole arrangements of paramagnetic, diamagnetic, and ferromagnetic in the absence and in the presence of a magnetic field [14]. (***H***: magnetic field)

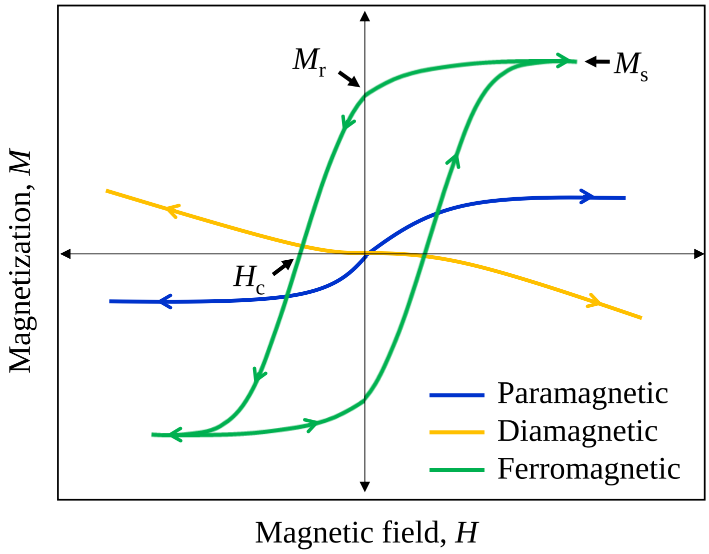

Figure 1-6. Representative magnetization behavior of paramagnetic, diamagnetic, and ferromagnetic when an external magnetic field is applied [13,14]. (H_c: coercive force, M_r: residual magnetization, M_s: saturation magnetization)

1.2.2. Classification of Thick-Film Materials

Thick-film pastes contain various materials, and the classification according to the electrical function is the most common. Those are generally classified to insulator, dielectric, resistor, and conductor paste [1–4]. Insulator and dielectric pastes consist of glass frits and/or metal oxides with an organic vehicle, and those are also referred to as glass pastes. Insulator pastes are mainly used as overcoats and crossovers [15]. The main function of overcoats is to prevent unwanted current flow as a barrier layer and protect circuits from hostile environment [1–4,15]. The main function of the crossovers is to insulate one conductor layer from the next with a minimum of capacitive coupling and support the top conductor [1–4,15]. In case that several layers are formed, it is referred to as multi layering rather than crossover. For the insulator pastes used as overcoats and crossovers, materials which have high resistivity, low permittivity, and high chemical durability are suitable [1–4,15]. The resistivity of most glasses is approximately higher than 10^{10} $\Omega\cdot$cm or the conductivity is approximately less than 10^{-10} S/cm at room temperature, as shown in **Figs. 1-7** and **1-8** [16,17]. In addition, the permittivity of most glasses is less than 10 [16]. Therefore, glasses are basically an excellent insulator, and those are main materials of the insulator pastes used as overcoats and crossovers. However, there are ion conductivity glasses, in which ions (e.g., Ag, Li, Cu, Na, or F ion) work as a conductive carrier, and electron conductivity glasses (e.g., chalcogenide glass), in which electrons or holes work as a conductive carrier [17]. The conductivity of these glasses is much high in comparison to that of practical glasses, as shown in **Fig. 1-8**. These high conductivity glasses are not used for the insulator pastes. Dielectric pastes are mainly used as dielectrics in capacitors, and the main function is to maximize the capacitance per unit area by separating a top and bottom conductor [2–4,15]. Therefore, ferroelectric materials (e.g., $BaTiO_3$) which have high permittivity and high resistivity are typically employed with glass frits for the dielectric pastes used as dielectrics in the capacitor [2–4]. In case that the formed thick-film insulator or dielectric is fired several times in the fabrication process of electronic components and circuits, crystallization glasses or mixtures of glass and metal oxide (e.g., Al_2O_3 and SiO_2) are typically used to prevent the flow of glass [4].

Resistor pastes consist of glass frits, metal powders and/or metal oxides with an organic vehicle. The glass forms the insulation phase in the thick-film resistor, whereas the metal and/or metal oxide form the conductive phase, as shown in **Fig. 1-9**. **Table 1-1** shows the resistivity of conductive materials used for resistor pastes. The ratio of the insulating phase to the conductive phase determines the final resistivity and the temperature coefficient of resistance (TCR). The resistor pastes with standard decade resistance are generally blended to obtain the target resistance [2]. For example, 10 Ω/sq. and 100 Ω/sq. resistor paste can be mixed in all proportions to produce the resistors yielding intermediate values of the resistor pastes. The resistor pastes enable to provide wide resistance range from approximately 1 Ω/sq. to 10^9 Ω/sq. [1–4]. TCR with a unit of ppm/°C is defined as the fractional change in resistance over a given temperature range, and that is expressed by [1]

$$\mathrm{TCR} = \frac{\Delta R/R}{\Delta T}, \tag{1-3}$$

where $\Delta R/R$ is a relative change in resistance, and ΔT is a change in temperature. Metals generally show an increase in resistance with increasing temperature, and the TCR is positive [1]. On the other hand, the resistance of the thick-film resistor does not change linearly against temperature and mostly shows the minimum value at a certain temperature, as shown in **Fig. 1-10**. Therefore, it is common practice to refer to the hot TCR calculated with the resistance values at 25°C and 125°C, and the cold TCR calculated with the resistance values at 25°C and -55°C [2]. Each TCR is expressed by [2]

$$\mathrm{TCR_{hot}}\ (\mathrm{ppm/^\circ C}) = \frac{(R_{125}-R_{25})/R_{25}}{100} \times 10^6, \tag{1-4}$$

$$\mathrm{TCR_{cold}}\ (\mathrm{ppm/^\circ C}) = \frac{(R_{25}-R_{-55})/R_{25}}{80} \times 10^6. \tag{1-5}$$

Since the main function of the resistor is to control current and voltage in circuits, the resistance control and the hot and cold TCR as close as possible to zero are required for the resistor paste.

Conductor pastes mainly consist of metal powders, small amount of glass frits, and/or metal oxides with an organic vehicle. **Table 1-2** shows the resistivity and melting point of metals used for conductor pastes. Precious metals (e.g., Ag, Au, Pd, and Pt) are extensively used for the conductor paste because those are stable at high temperature in air, and the resistivity is low [1–5,19]. Ag is the major material for the conductor paste due to the lowest resistivity, and it is also often used with other precious metals since the migration resistance and solder leach resistance are low. It is also known that Ag is easy to form alloys with other precious metals. For example, Ag alloys with Pd or Au in the entire composition range, as shown in **Figs. 1-11(a)** and **1-11(b)**. Base metals with low bulk resistivity (e.g., Cu, Al, and Ni) are also used for the conductor paste [1–4]. There is no room for doubt that Cu is used for the conductor paste because the bulk resistivity is the second lowest. In addition, the migration resistance of Cu is high in comparison to that of Ag or the alloys, as shown in **Fig. 1-12**. The disadvantage is that Cu needs to be fired under inert gas (e.g., N_2) since it is oxidized in air. Al is widely used for back-side electrodes of p-type crystalline silicon photovoltaic cells because of forming a back-surface field and improving the photo-conversion efficiency of the cells [21,22]. Ni was previously used for electrodes in plasma display panels because it does not form the amalgam with Hg [4]. The base metals have abovementioned unique advantages and are suitable for some applications in addition to the low cost. In the conductor paste, the glass frit generally promotes the sintering of the metal powder during the firing process and binding of the metal film to the substrate [2–5,19]. In addition to the resistivity and the adhesion to the substrate, the glass frit affects the solderability, platability, suitability of wire bonding, compatibility with other circuit materials, and/or long-term stability (e.g., resistance to migration) which are common functions required for the conductor paste [3,4].

There are thick films which adhere to the substrate by the polymer matrix instead of the glass matrix. Those are referred to as a polymer thick film (PTF). Three types of polymers are generally used for PTFs: thermoplastic, thermosetting, and ultraviolet (UV)-curable polymer [1]. Thermoplastic polymers are formed by monomers and/or oligomers linked by van der Waals forces [23]. These types of polymers become soft when it is heated by glass transition temperature or melting temperature, and those become hard when it is cooled. The PTF made from the thermoplastic polymers is relatively not resistant to elevated temperature. Acrylic, polyester, and vinyl are the typical thermoplastic polymers used for the PTF [1]. Thermosetting polymers are formed by the chemical bond of monomers, and those have crosslinked structure [23]. These types of polymers are irreversibly hardened by heat. The PTF made from the thermosetting polymers has the strong and stable polymer matrix, and the risk of re-melting is small, which leads to the improved film stability. Epoxy and phenolic are the typical thermosetting polymers used for the PTF [1]. UV-curable polymers are polymerized by radical or cation generated with an UV light radiation. **Table 1-3** shows major materials and properties of typical UV-curable polymer systems. The polymerization mechanism of radical polymerization is that the radical is generated by the decomposition of initiator or the hydrogen abstraction reaction between the initiator and other molecules with the UV light radiation, and the radical reacts with the monomers and/or oligomers, as a result, the sequential polymerization with the monomers and/or oligomers occurs [24,25]. The polymerization mechanism of cationic polymerization is that Brønsted acid or Lewis acid is generated by the decomposition of initiator with the UV light radiation, and the acid reacts with the monomers and/or oligomer [25–27]. The radical polymerization type is widely used for the PTF due to the fast curing in comparison to the cationic polymerization type. Compared with the glass-bond thick film, the process temperature of the PTF and the cost are low. **Figure 1-13** shows the classification of thick-film materials. In this thesis, the glass-bond thick-film conductors are focused on.

Table 1-1. Resistivity of conductive materials used for resistor pastes [4,18]

Precious metal and the compound	Resistivity (μΩ·cm)	Base metal and the compound	Resistivity (μΩ·cm)
Ag/Pd	1.47–10.0	Ta	12.3
Ru	7.5	TaN	180–250
RuO_2	35	Ta_2N	135
$Bi_2Ru_2O_7$	150–2300	LaB_6	15
$Pb_2Ru_2O_6$	270–2000	WC	80
$SrRuO_3$	2000	$MoSi_2$	21.5
$CaRuO_3$	3700	$TaSi_2$	35–70
$BaRuO_3$	18000	SnO_2	41

Table 1-2. Resistivity and melting point of metals used for conductor pastes [4,18]

Metal	Resistivity (μΩ·cm)	Melting point (°C)
Ag	1.47	952
Au	2.05	1064
Pd	10.0	1552
Pt	9.81	1772
Cu	1.55	1083
Al	2.50	660
Ni	6.2	1453

Table 1-3. Major materials and properties of typical UV-curable polymer systems [24–27]

Polymerization type	Radical polymerization	Cationic polymerization
Photopolymerization monomer and oligomer	Urethane acrylate Epoxy acrylate Acrylic acrylate Polyester acrylate	Cycloaliphatic epoxy Vinyl ether Oxetane (cyclic ether)
Photopolymerization initiator	Benzophenone Acetophenone Benzoin Ether Thioxanthone	Sulfonium salt Iodonium salt
Curing contraction	High	Low
Curing inhibition by oxygen	Inhibited	Not inhibited
After pausing UV irradiation	Curing stop	Curing continues
Photopolymerization rate	Fast	Slow

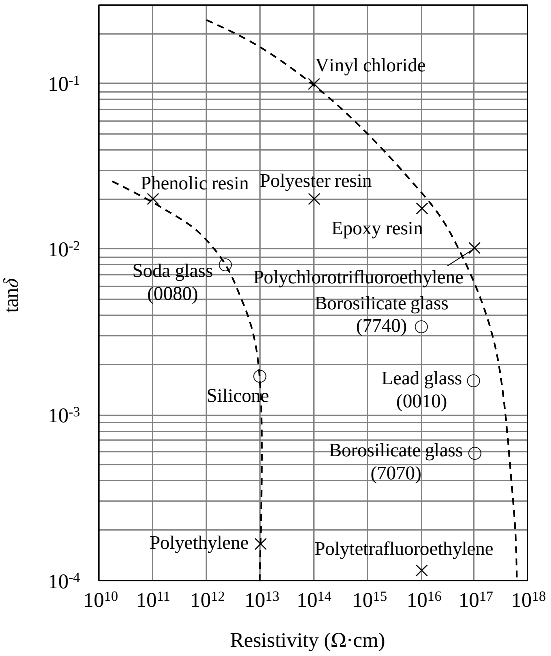

Figure 1-7. Relationship between resistivity and tanδ of insulation materials [16]. The glass code is the product name of Corning.

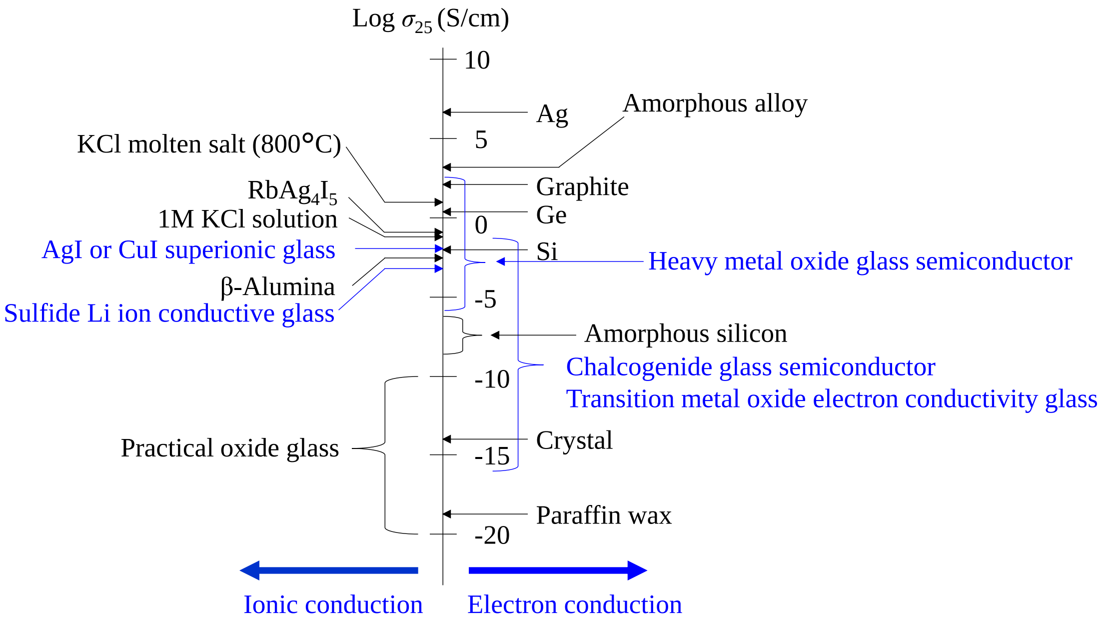

Figure 1-8. Conductivity of glasses at room temperature [17].

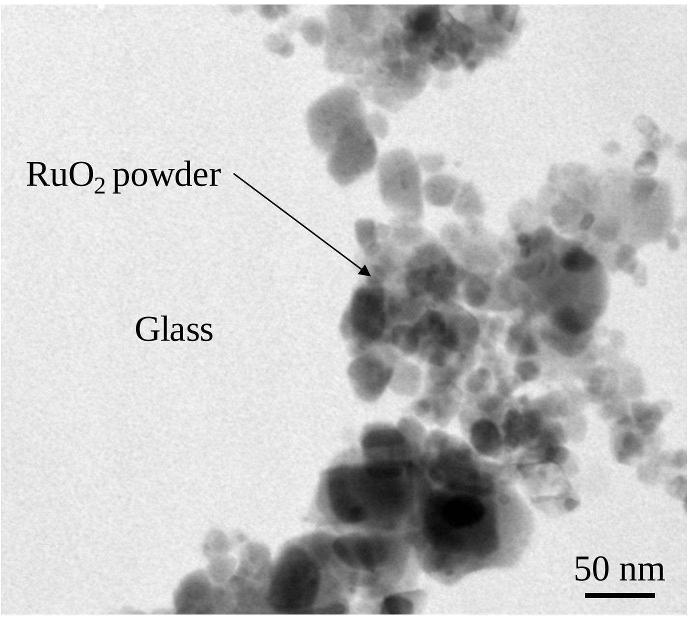

Figure 1-9. STEM image of conductive paths formed by RuO_2 powder in a glass phase of thick-film resistor.

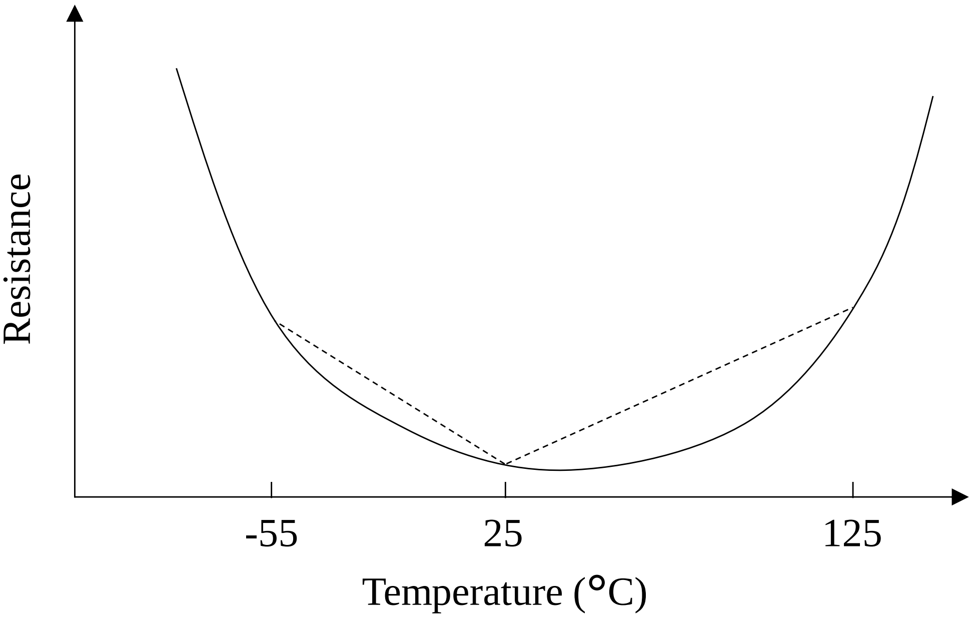

Figure 1-10. Resistance-temperature behavior of a thick-film resistor [2].

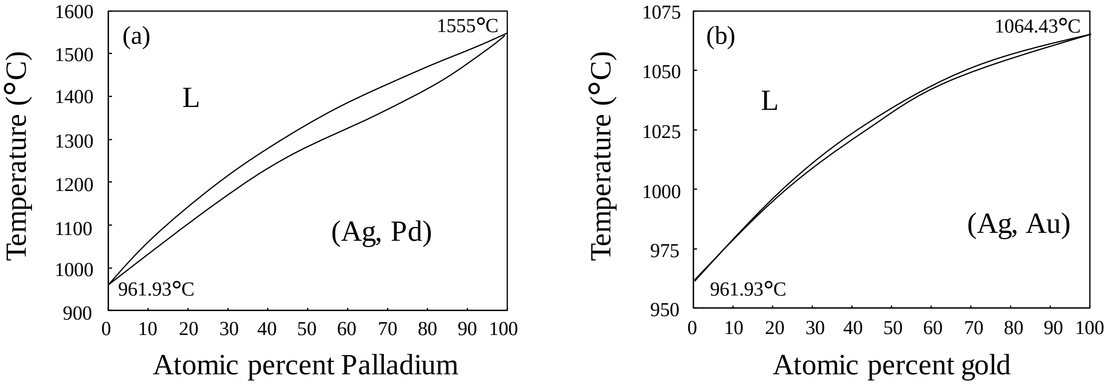

Figure 1-11. Phase diagrams of Ag alloys: (a) Ag-Pd and (b) Ag-Au [20].

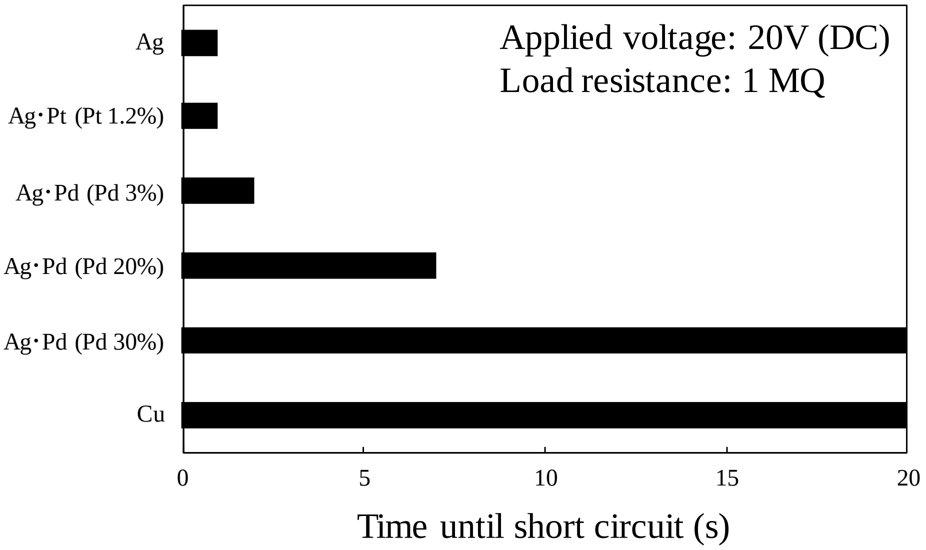

Figure 1-12. Time until short circuit is detected after dropping water on thick-film conductor circuit patterns with 1 mm line space showing migration resistance [4].

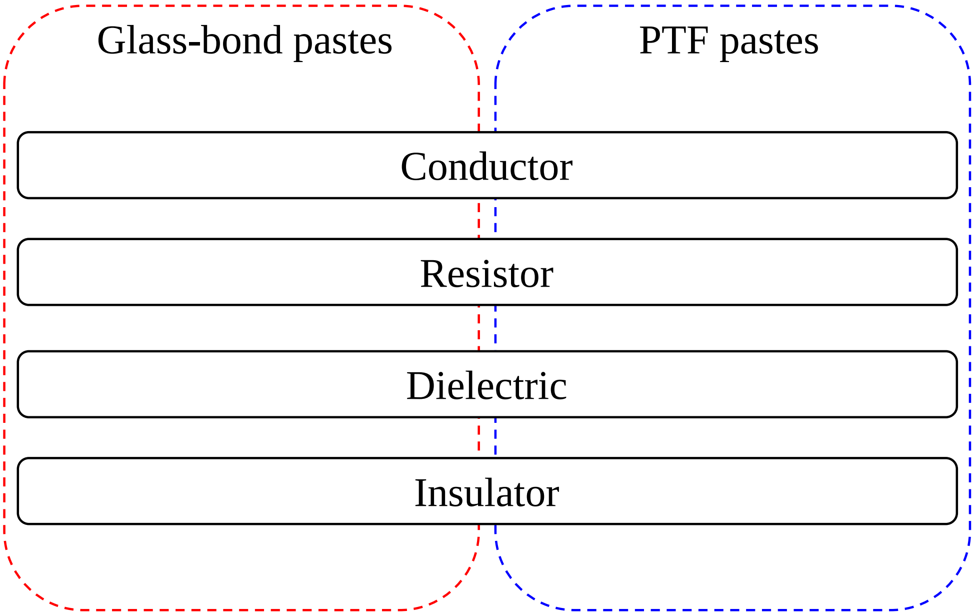

Figure 1-13. Classification of thick-film materials.

1.2.3. Electrical Properties of Thick-Film Conductors

Thick-film conductors are widely used for various applications, as shown in **Table 1-4**. In either case, the main function is to form the conductive circuit and provide the interconnection with electronic components and circuits electrically. The bulk resistivity (ρ) with a unit of Ω·cm for the thick-film conductor is expressed by [1]

$$\rho = R \times \frac{WT}{L}, \tag{1-6}$$

where R is the resistance, L is the length, W is the width, and T is the thickness. In addition, the sheet resistance with a unit of Ω/sq. defined as the bulk resistivity at a given thickness is often used since the resistance of the circuit can be calculated by simply multiplying the sheet resistance by the aspect ratio of the thick-film conductor [1]. On the other hand, the contact resistivity between the thick-film conductor and substrate is also discussed in case that the substrate is conductive. The detail is discussed in Subsection 2.3.3.

Table 1-4. Application examples of thick-film pastes [1–4,15,21,28–34]

Application		Thick-film paste		
		Conductor	Resistor	Glass
Passive component	Ceramic capacitor	○		○
	Mica capacitor	○		
	Tantalum electrolytic capacitor	○		
	Chip resistor	○	○	○
	Network resistor	○	○	○
	Carbon film resistor	○	○	
	Inductor	○		
Functional component	Filter	○		
	Piezoelectric element	○		○
	Crystal oscillator	○		
	Heater	○	○	○
Semiconductor	Varistor	○		
	Thermistor	○		
	Light Emitting diode	○		
	Laser diode	○		
	Photovoltaic	○		
Display	Plasma display	○	○	○
	Liquid crystal display	○		
Circuit board	Thermal head	○	○	○
	Hybrid integrated circuit	○	○	○
	Multilayer ceramic substrate	○	○	
	Printed circuit board	○	○	

1.2.4. Chemical Durability of Thick-Film Conductors

Thick-film conductors are generally interconnected with electronic components and circuits by the wire bonding, the direct soldering, or the soldering after the plating. For example, the thick-film conductor formed on the substrate in the hybrid integrated circuits is wire-bonded and/or soldered directly [3,35,36]. The thick-film conductor used as the busbar of the crystalline silicon photovoltaic cells is directly soldered, and that used as the electrode termination of the surface-mount chip components is plated and then soldered [37,38] In the wire bonding and the direct soldering process, the interdiffusion of metals and the formation of intermetallics can occur between the thick-film conductor and the wire or the solder. It is reported that Au and Al formed brittle $AuAl_2$ in the wire joint area [35]. The diffusion between Au and Al caused the Kirkendall void in the wire joint area [39]. The solder leach occurred due to the mutual solubility of metals [3,8,36]. It is known that Nernst-Brunner's equation shows a dissolution rate (d_n/d_t) of a solid metal into a liquid metal, and that is expressed by [40]

$$\frac{d_n}{d_t} = K\frac{A}{V}(n_s - n), \tag{1-7}$$

where n is concentration of the solute at the time (t), n_s is saturated concentration, V is volume of the liquid, A is interfacial area of the reaction, and K is a reaction rate constant. Equation 1-7 estimates the simple dissolution rate, and the actual dissolution rate should be more complex since the formation of intermetallics affects the dissolution rate [5,40]. Equation 1-7 also indicates that the dissolution rate is proportional to the concentration of solute $(n_s - n)$, and the dissolution rate decreases by the addition of metal included in the soldered metal to the solder in advance. For example, it is known that the dissolution rate of Ag into the Sn/Pb/Ag solder was much slower than that into the Sn/Pb solder, as shown in **Fig. 1-14** [4,40]. The interdiffusion of metals is also affected by the solder wettability and soldering temperature [40]. Therefore, it is needed to control the interdiffusion of metals for the thick-film conductors wire-bonded or soldered directly by the choice of metal powders and glass frits in addition to the choice of suitable wires and/or solders. On the other hand, plating process requests different chemical durability for the thick-film conductor. Ni and Sn are typically electroplated on the thick-film conductor used as the electrode termination of the surface-mount chip components [28,38]. Ni is used as the intermediate layer, and it prevents the thick-film conductor from the solder leach [38]. Sn is used as the external layer, and it improves the solder wettability [38]. As a result, excellent solder adhesion is obtained in the surface-mount process. Although there are various electroplating conditions, Ni is electroplated under the weak acidic condition, and Sn is electroplated under the strong acidic condition in many cases [41,42]. Neutral pH is ideal but the stability of the plating bath becomes difficult, and the watts Ni bath and Sn acid bath (e.g., sulfuric acid bath and metasulfonic acid bath) are commonly used [41,42]. Therefore, it is needed to control the acid durability for the plated thick-film conductors by the choice of metal powders and glass frits.

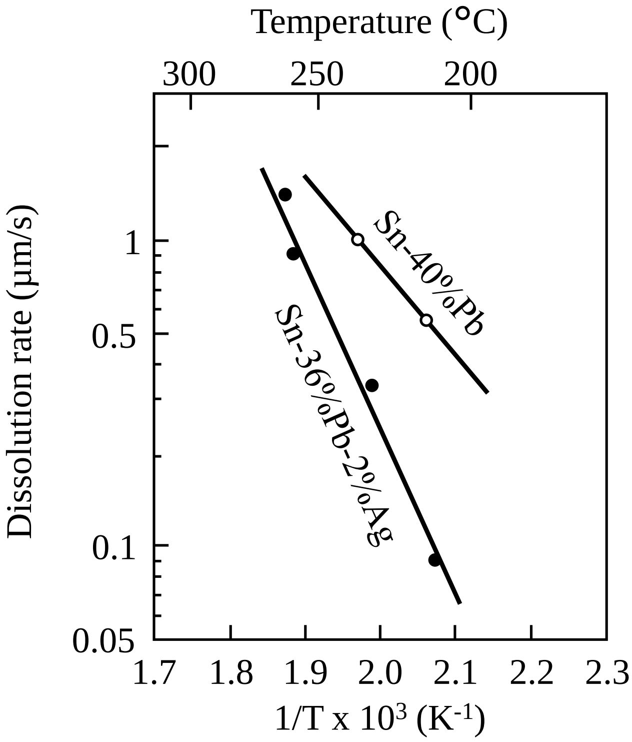

Figure 1-14. Temperature dependence of Ag dissolution rate in solders [40].

1.3. Thick-Film Conductor Formation Process

1.3.1. Circuit Formation Technology

Chemical vapor deposition (CVD) and physical vapor deposition (PVD) are extensively used for the thin-film formation. CVD deposits a layer of material by the reaction of one or more volatile precursors and the decomposition on the substrate surface, whereas PVD deposits a layer of material by gasifying the solid deposition material and condensing it on the substrate surface (e.g., sputtering and vacuum deposition) [43]. The strain in the film generally becomes high as increasing the film thickness, and the film is finally peeled off at the critical thickness. Since the critical thickness of thin films is several microns in most cases, these gas-phase methods are not used for the thick-film formation [44]. Although the definition of the thick film and thin film by the thickness is not clear, it is said that the thick film generally targets on the thickness between 5 μm and 25 μm, whereas the target thickness of thin film is approximately less than 5 μm [28,45].

The thick film is mainly formed using the screen-printing technology. **Figure 1-15** shows a comparison of the screen-printing technology and etching technology using metal foils. The screen printing forms the thick film by transferring the paste onto the substrate through the screen with an etched pattern of desired geometry, so the deposition and the patterning are completed simultaneously [1–4]. After the print process, the annealing is needed to develop electrical properties. On the other hand, in the etching technology, the thick film is formed through the process of resist-coating, patterning, development, etching, and resist-removing, and the waste liquid is generated. Although the material options of substrates in the etching technology are a few, the screen printing enables to form the thick film on various substrates (e.g., ceramics, glasses, and textiles). In addition to the abovementioned advantages, the screen printing enables to form the large circuit formation such as 3 m square, and it is possible to overprint the thick film. The definition of patterning was a major disadvantage of the screen printing, but there is a report of the conductor circuit formation of 10 μm line width at a laboratory scale and of 50–80 μm line width at a manufacturing scale [46]. Since the screen printing is simple, environmental-friendly, and low cost, the technology has been used for the thick-film formation. Dispenser, dipping, gravure, flexographic, and spray technology also have been used for the formation of thick film but the screen-printing technology is still the most widely used [28]. The detailed thick-film formation process using the screen printing is explained in Subsection 1.3.2 and 1.3.3.

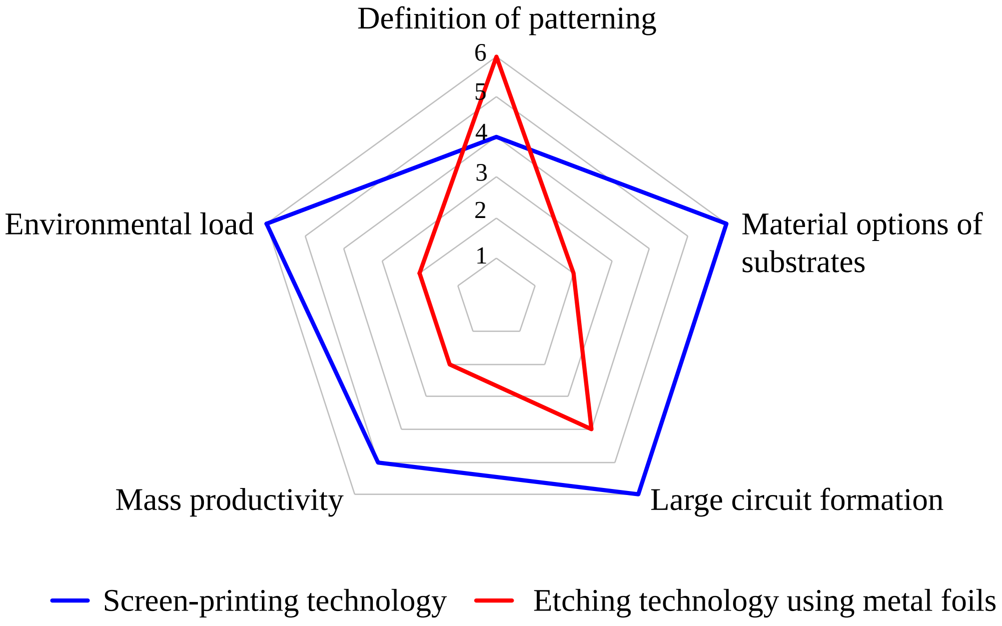

Figure 1-15. Comparison of screen-printing technology and etching technology using metal foils [46]. The higher the number is, the better performance is.

1.3.2. Screen-Printing Process

The screen printing is the process of transferring the paste onto the substrate through open pattern areas of the screen. **Figure 1-16** shows the typical process of the printing screen preparation. The open pattern areas are generally formed using an UV reactive emulsion on the mesh [3,47,48]. There are “off contact” and “in contact” screen-printing technique, and the “off contact” mode of the screen printing is used more widely [3]. **Figure 1-17** illustrates the basic “off contact” screen-printing process. After the paste is placed on the surface of the screen, a flexible squeegee traverses across the screen under pressure, as shown in **Fig. 1-17(a)**. The passage of the squeegee presses the screen into contact with the substrate and transfers the paste through the open meshes of the screen at the same time, as shown in **Fig. 1-17(b)**. The elasticity of the screen materials peels off the screen from the substrate naturally after the squeegee passes, and the screen goes back to the original position, while the printed pattern leaves on the substrate, as shown in **Fig. 1-17(c)**. In case of the “in contact” mode of the screen printing, the screen and substrate remain contacted throughout the printing stroke, and those are separated mechanically after the completion of the squeegee traverse. It is known that the “in contact” mode of the screen printing has been widely used for printing a solder paste through a metal screen in the surface-mount process [47,50]. The metal screen enables to form the thick thick-film because of the non-mesh screen but the paste spreads to the back side of the metal screen under the “off contact” printing condition. Therefore, the “in contact” mode of the screen printing was mainly optimized for printing the solder paste using the metal screen.

The printing behavior of the paste is affected by the viscosity, surface tension, and dependence of these properties on shear rate and time [3]. The viscosity can be explained with the liquid body model as being made up exceedingly thin layers of area (A) stacked one above the other, as shown in **Fig. 1-18**. When force $(\boldsymbol{F})$ is applied to the top layer, shear stress (τ) is defined as [3,4,51]

$$\tau = \frac{\boldsymbol{F}}{A}. \tag{1-8}$$

As the top layer moves under the applied τ, it pulls the underneath layer, and this action continues throughout the stacks, as a result, the velocity gradient between the layers $(\mathrm{d}v/\mathrm{d}x)$ defined as the shear rate (D) occurs. The viscosity (η) of the fluid is then defined as [3,4,51]

$$\eta = \frac{\tau}{\mathrm{d}v/\mathrm{d}x} = \frac{\tau}{\mathrm{D}}, \tag{1-9}$$

$$\tau = \eta \mathrm{D}. \tag{1-10}$$

Figure 1-19 shows the shear stress versus the shear rate diagram, which illustrates the flow characteristics of three groups: Newtonian, dilatant, and pseudoplastic fluid. The Newtonian fluid shows a linear relationship between the applied τ and D. On the other hand, the dilatant and pseudoplastic fluid are non-Newtonian fluid, and the relationship between the applied τ and D is expressed by [4,51]

$$\text{Dilatant fluids: } \tau = \eta \mathrm{D}^{\mathrm{n}} \ (\mathrm{n} > 1), \tag{1-11}$$

$$\text{Pseudoplastic fluids: } \tau = \eta \mathrm{D}^{\mathrm{n}} \ (0 < \mathrm{n} < 1), \tag{1-12}$$

where n is a viscosity index. When τ on the fluid increases, the apparent viscosity of the dilatant fluid increases, and that of the pseudoplastic fluid decreases. Most thick-film pastes show the pseudoplastic behavior [3]. The pseudo-plasticity is frequently confused with the thixotropy. A thixotropic fluid is one in which the apparent viscosity reduces with time under constantly applied D, and most thick-film pastes have the thixotropic behavior in addition to the pseudoplastic behavior [3,4]. These rheological behaviors are complex, and the paste viscosity changes during the screen-printing process, as shown in **Fig. 1-20**. The viscosity of the paste reduces by as much as two to three orders of magnitude as it passes through the screen since the combination of squeegee pressure, velocity, and screen tension increases the shear rate. The viscosity reduction makes the paste flow more readily, as shown in **Figs.1-21(a)** and **1-21(b)**. Since the viscosity of the paste remains low shortly after being deposited on the substrate, the paste flows under the influence of gravity and surface tension, while the rough surface caused by the mesh wire becomes smooth, as shown in **Figs. 1-21(c)** and **1-21(d)**. The process of leaving the parts for a few minutes to make the surface smooth is referred to as leveling. Although the viscosity does not return immediately to its initial value after the shear rate goes back to the initial value, it gradually increases.

The surface tension is other important property of the paste which affects the printing behavior. It is known that Young's equation shows a contact angle of a hemispherical liquid droplet on a solid, and that is expressed by [51]

$$\gamma_{\mathrm{s}} = \gamma_{\mathrm{SL}} + \gamma_{\mathrm{L}}\cos\theta, \tag{1-13}$$

where γ_{s} is surface tension of the solid, γ_{L} is surface tension of the liquid, γ_{SL} is interfacial surface tension between the solid and liquid, and θ is a wetting angle of the liquid on the solid, as shown in **Fig. 1-22**. Therefore, $\gamma_{\mathrm{L}}\cos\theta$ means the wetting tension. If γ_{L} is smaller than γ_{s} and the wetting angle is close to zero, the liquid droplet tends to wet and spread over the surface of the solid. The surface energy of thick-film pastes is generally low in comparison to that of ceramics (e.g., Al_2O_3), so the flow is controlled by the viscosity in many cases [3].

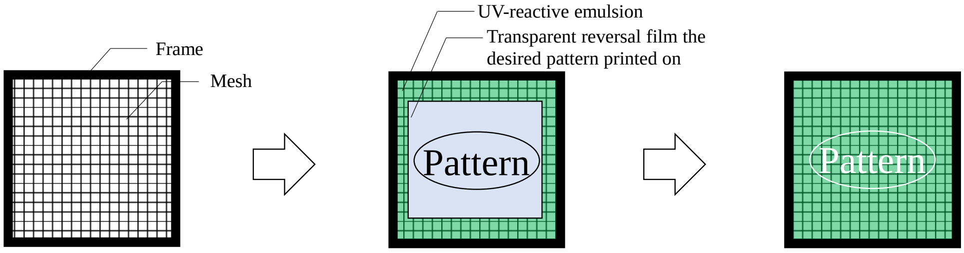

The mesh is stretched on the frame.

The mesh screen is coated by the UV-reactive emulsion which hardens with the UV light radiation. Next, it is exposed to the UV light through the transparent reversal film the desired pattern printed on.

After removing the reversal film, the unhardened emulsion is rinsed away, and the mesh screen is finally dried.

Figure 1-16. Basic process of printing screen preparation [3,47].

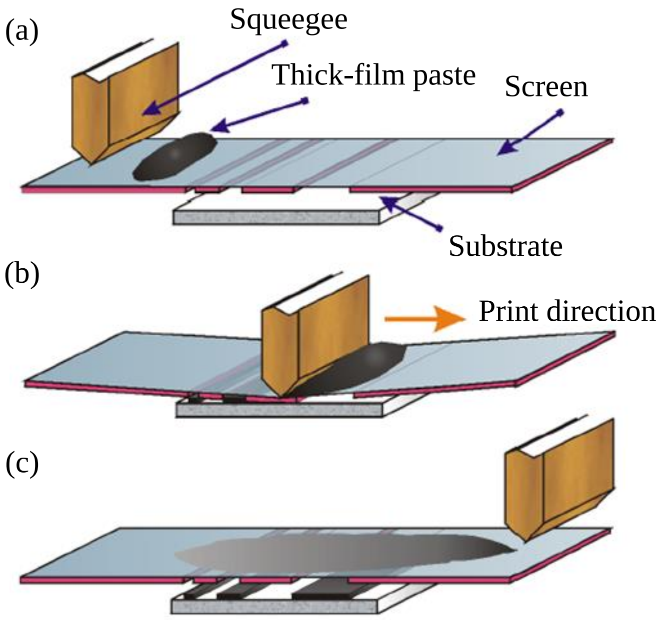

Figure 1-17. Basic “off contact” screen-printing process: (a) before, (b) during, and (c) after printing [49].

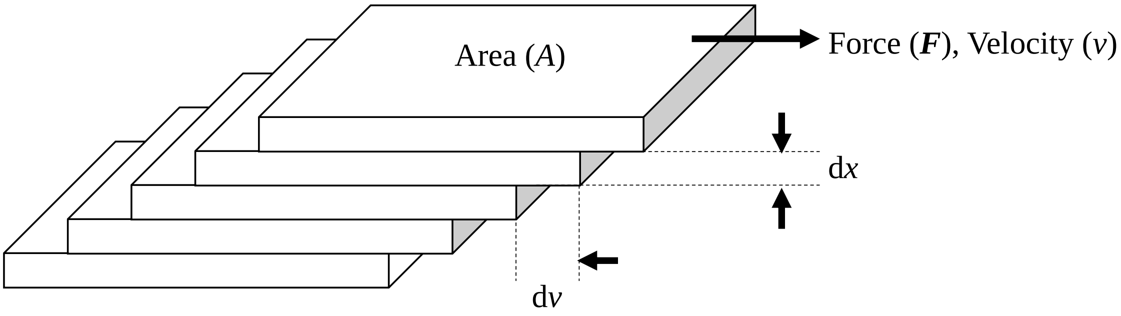

Figure 1-18. Classical model for illustrating viscosity [3,51].

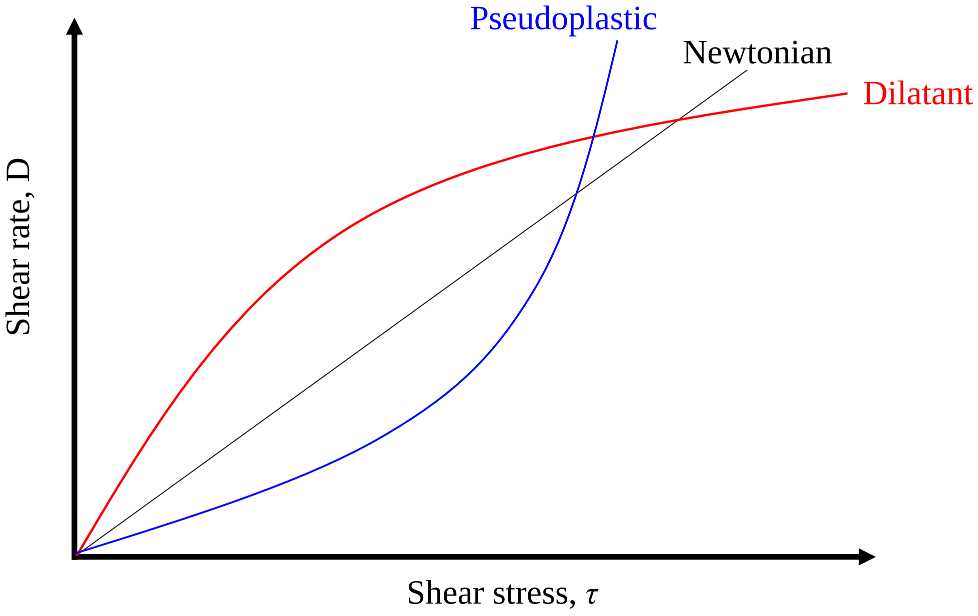

Figure 1-19. Rheological behavior of Newtonian, dilatant, and pseudoplastic fluid [2–4].

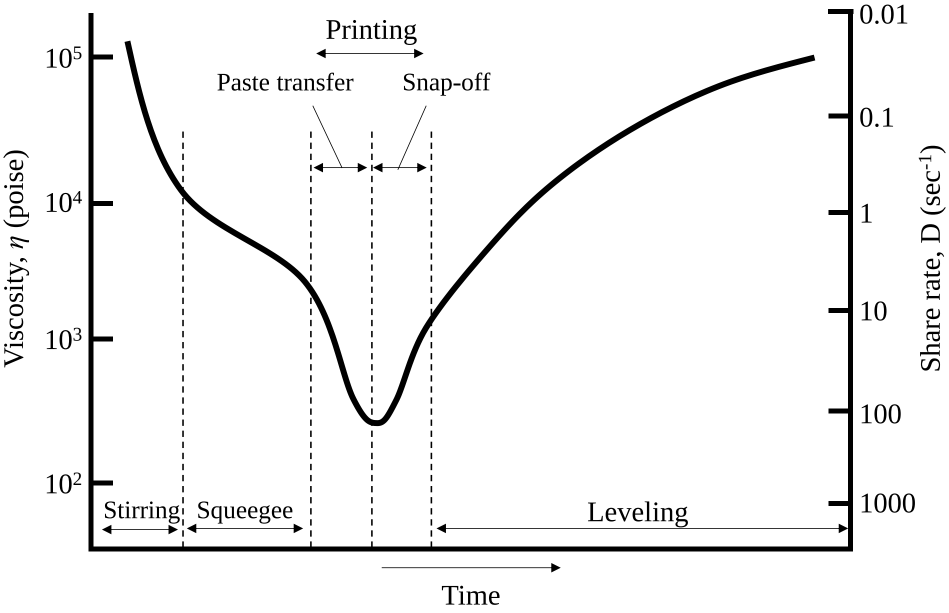

Figure 1-20. Changes of shear rate and viscosity during the screen-printing process [3].

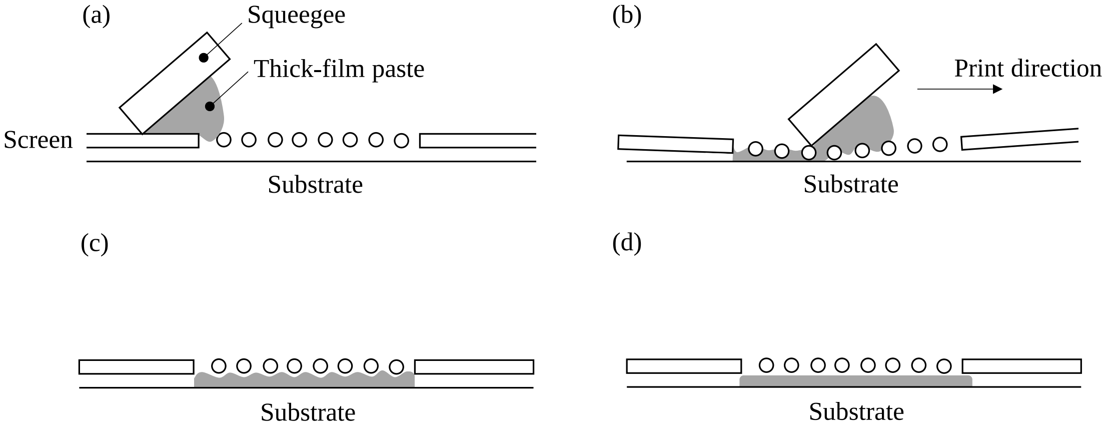

Figure 1-21. Schematic depiction of paste behavior during the screen-printing process: (a) started being pressured by the squeegee, (b) during the transfer by the squeegee, (c) shortly after being deposited on the substrate, and (d) after the leveling on the substrate [3,4,47].

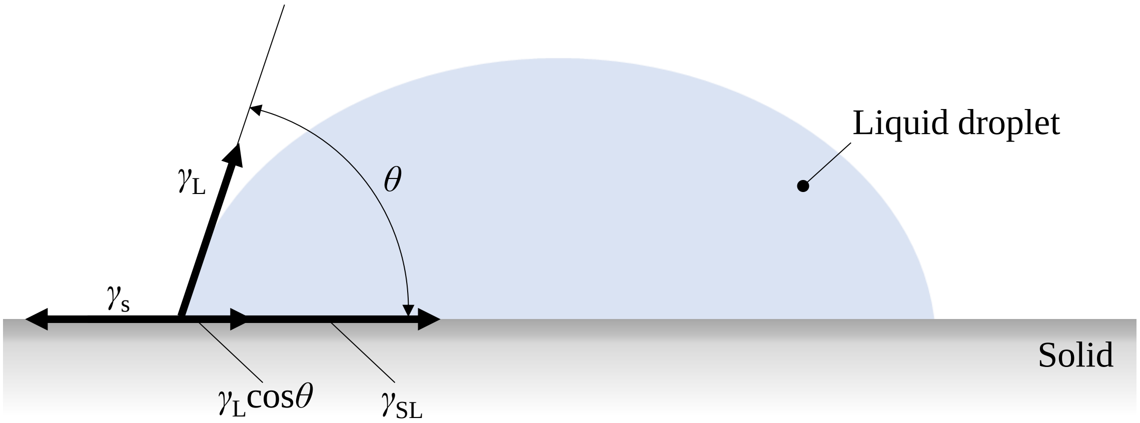

Figure 1-22. Contact angle of a hemispherical liquid droplet on a solid surface [51].

1.3.3. Annealing Process

After the screen-printing process, the formed thick film is annealed through two steps, drying and firing process. The purpose of the drying process is to remove the volatile organic solvents, and the typical drying temperature is between 70°C and 200°C. [1–3]. Infra-red or hot air heating is generally used for the drying process. Printed parts are often batch dried in box ovens in the small-scale production but the drying process typically carried out in moving belt driers in the mass production. The high temperature firing process is complex in comparison to the drying process, and it performs three main functions: 1) remove the remaining organic vehicle, 2) develop the electrical properties of the thick film, and 3) bind the thick film to the substrate [1,3,4]. To control the temperature, heating and cooling rate, and volume of airflow stably, multi-zone moving belt furnaces are extensively used [1,3,4]. The firing duration is in the order of 20–60 min, and the firing peak temperatures are between 600°C and 1000°C in many cases [1–4]. **Figure 1-23** shows a typical firing profile with a peak temperature of 850°C as an example. There are two shoulders in the elevated temperature process to remove the remaining organic vehicle before the glass frit melts. It is reported that the remaining carbon could cause pinholes or bubbling in the thick film during the firing process [3]. The firing temperature for the polymer thick film (PTF) is significantly low in comparison to that for the glass-bond thick film. For example, the PTF is annealed at approximate 200°C to develop electrical properties, and such process is referred to as cure rather than firing [1,8].

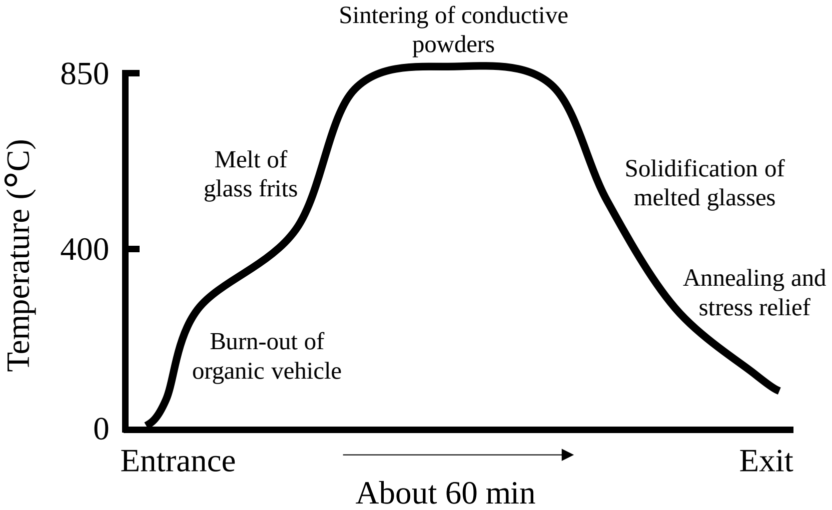

Figure 1-23. Typical firing profile with a peak of 850°C for the thick-film formation [3].

1.4. Substrates Used for Thick-Film Conductors

The common function of substrates in most applications is to provide mechanical support with high reliability, and the mass productivity and low cost are required. The main substrates used for glass-bond thick-film conductors are ceramics. For example, the alumina substrate with alumina content in the range of 94–97% extensively has been used for the hybrid integrated circuit since the early stage of thick-film history [1–4]. The 94–97% Al_2O_3 substrates can be synthesized at low temperature in comparison to the high purity alumina, and those are composed of crystals of alpha-alumina embedded in a glass crystalline matrix, usually composed of calcium and magnesium silicate which improve the densification and electrical properties [1,3,4]. It is reported that the composition of Al_2O_3 substrates was slightly different by manufacturers, as shown in **Table 1-5**. The applications of the thick film material have been diversified over the past 50 years, and a variety of substrates are used nowadays. **Table 1-6** shows substrate examples used for various applications of thick-film conductors. Ferroelectric $BaTiO_3$ is used for the multi-layered ceramic capacitor (MLCC) [29]. The MLCC is made of the multi layers of ceramics and inner electrodes (e.g., Ni) like sandwich, and the capacitance (C_t) is expressed by [28,29]

$$C_t = \varepsilon_0 \times \varepsilon_\mathrm{r} \times \left(\frac{S}{d}\right) \times N, \tag{1-14}$$

where ε_0 is a dielectric constant of free space, ε_r is a relative dielectric constant of the ceramic, S is overlap area of the internal electrodes, d is a thickness of the dielectric layer, and N is the number of the individual dielectric layers. The high dielectric constant of $BaTiO_3$ enables to improve C_t of the MLCC. AlN is used for heaters since the thermal conductivity is usually in the order of 138–200 W/mK, which is significantly high in comparison to other ceramics [30,52]. Crystalline silicon is used for most photovoltaic cells [21,37]. Soda lime glasses were used in the early stage of the plasma display panel (PDP) but those were changed to the glass with high strain point to avoid the thermal shrinkage during the PDP making process [31]. PD200, composed of SiO_2–Al_2O_3–R_2O–R'O (R_2O: alkali metal oxide, R'O: alkaline-earth metal oxide) developed by AGC, was famous for the PDP [32]. It is reported that the strain point of the soda lime glass was approximately 511°C but that of the PD200 was 570°C [31,32]. Green sheets composed of Al_2O_3 filler and CaO–Al_2O_3–SiO_2–B_2O_3 glass are used for the low temperature co-fired ceramics (LTCC) [33,34]. The LTCC is made of the multi layers of ceramics and inner electrodes (e.g., Ag, Cu, and Au), and it is a multi-layered circuit board [33,34]. In case of polymer thick films, polymer substrates (e.g., polyesters, polycarbonates, and polyimide plastics) are available since the cure temperature is low. For example, polyester is used for a biosensor which is an analytical instrument to detect a biochemical signal [53].

Table 1-5. Composition analysis of 96% Al_2O_3 substrates produced by some manufactures [4]

	American Lava Alsimag 614	Coors ADS 96	Kyoto A 476	Narumit AT 396	Stemag	English Glass UL 300
Al_2O_3	94.67	95.10	95.25	95.05	97.31	97.02
SiO_2	2.98	2.33	3.38	3.30	1.71	1.97
CaO	0.2	< 0.01	0.02	0.04	0.84	1.00
MgO	2.15	1.94	1.35	1.61	0.14	0.14

Table 1-6. Substrate examples used for various applications of thick-film conductors [1–4,15,21,29–34]

Application	Substrate
Hybrid integrated circuit	Al_2O_3
Multilayered ceramic capacitor	$BaTiO_3$
Heater	AlN
Photovoltaic cell	Si
Plasma display panel	Soda lime glass SiO_2–Al_2O_3–R_2O–R’O* glass
Low temperature co-fired ceramics	Green sheet composed of Al_2O_3 filler and CaO–Al_2O_3–SiO_2–B_2O_3 glass

*R_2O: alkali metal oxide, R’O: alkaline-earth metal oxide

1.5. Glass Frits Contained in Thick-Film Conductors

1.5.1. Function of Glass Frits in Thick-Film Conductors

Conductor pastes mainly consist of metal powders, small amount of glass frits, and/or metal oxides with an organic vehicle. The glass frit is made by milling the glass. The glass frit in the conductor paste promotes the sintering of metal powder during the firing process and binding of the metal film to the substrate [2–5,19]. **Figure 1-24** illustrates the cross-sectional schematic depiction of two types of thick-film conductors after the firing process. The glass frit softens gradually with increasing temperature and flows. Furthermore, the melted glass reacts with the substrate, and it forms the glass layer underneath the meal rich layer on the substrate after the firing process, as shown in **Fig. 1-24(a)**. The thick-film conductor adhering on the substrate by the mechanical interlocking using the glass layer is referred to as a glass-bond type [2,4]. Therefore, glass frit significantly affects the adhesion of the thick-film conductor on the substrate. The glass also affects the electrical and metallurgical properties of thick-film conductors but those are mostly dependent upon the nature of the metal [3]. On the other hand, properties of the thick-film conductor such as the solder leach resistance are affected by a combination of both factors, the metal and glass [3]. The metal oxide reacts with the substrate during the firing process and forms crystalline compounds in some cases, as shown in **Fig. 1-24(b)**. For example, CuO reacts with the alumina substrate and forms $CuAlO_2$ and $CuAl_2O_4$ [2,4,5]. The thick-film conductor adhering on the substrate by the formation of crystalline compound is referred to as a chemical-bond type. The chemical-bond type conductor is rare since it generally requires above 950°C, and such a high temperature firing limits the application [2]. On the other hand, the metal oxide is often used with the glass frit together in the thick-film conductor since the mixed glass and oxide system enables to improve the adhesion even below 900°C [2].

There is no room for doubt that the choice of glass frits is restricted by the firing condition (e.g., firing peak temperature and firing duration). In addition, it is restricted by the compatibility with other materials and the thermal expansion of the substrate. For example, if the thick-film conductor is overlapped with the thick-film resistor and/or insulator in the circuits, interdiffusion may occur between these thick films during the firing process. It is needed to avoid the change of each material property. The thermal expansion of the glass in the thick-film conductor should closely match that of the substrate in the firing temperature range. The thermal expansion mismatch would result in a highly stressed system giving weak adhesion and resistance to thermal shock [3].

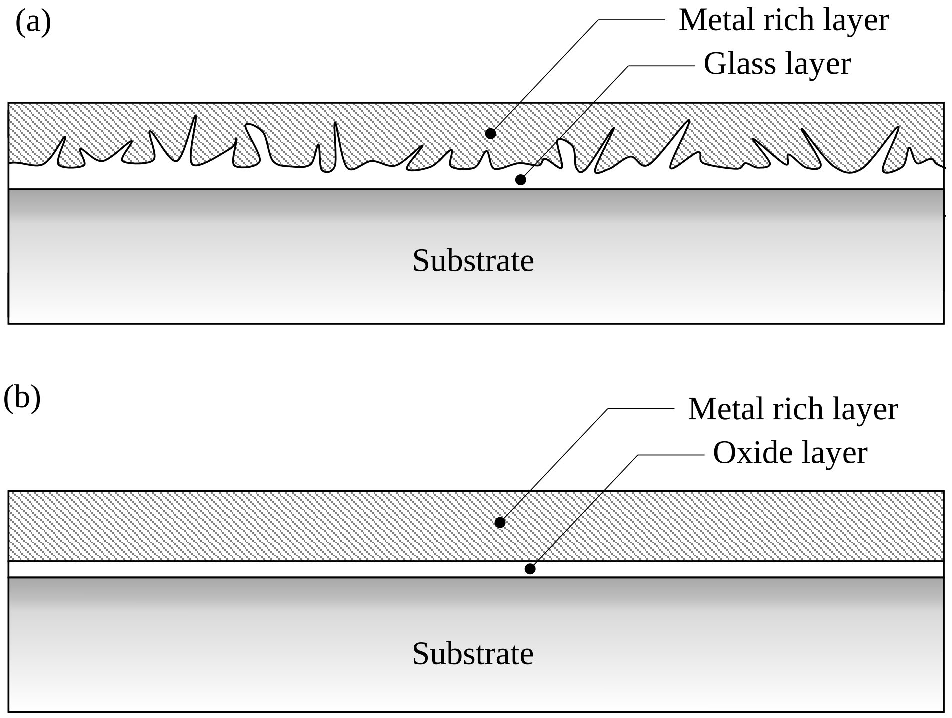

Figure 1-24. Cross-sectional schematic depiction of thick-film conductors after the firing process: (a) glass-bond type and (b) chemical-bond type [2–4].

1.5.2. Definition of Glass

ASTM (C162) states “a glass is an inorganic product of fusion that has cooled to a rigid condition without crystallizing” [54]. Dictionary of science and technical terms states “a glass is a hard, amorphous, inorganic, usually transparent, brittle substance made by fusing silicates, sometimes borates and phosphates, with certain basic oxide, and then rapidly cooling to prevent crystallization” [55]. However, there are organic and molecular glasses which are typically synthesized by condensation or polymerization, and those do not go through the general fusion and cooling process [56,57]. **Table 1-7** shows the comparison of glass synthesis methods. Solution based sol-gel and chemical vapor deposition (CVD) method do not go through the general fusion and cooling process, respectively [58,59]. There are glasses including crystals referred to as a glass ceramic or crystallized glass [60]. Tempered glasses, the outer surface of which is compressed and the interior of which retains tension by controlled thermal or chemical treatments, show three times or more strength in comparison to general glasses [61]. Due to the complexity of the structure of glass, all-encompassing definition for glass remains elusive.

It is thought that a current accepted simple definition of glass widely is “a glass is a non-crystalline solid, and a glass transition temperature (T_g) is observed in heating and cooling reversibly” [62,63]. **Figure 1-25** shows the schematic specific volume-temperature relationships for crystallization and glass formation. On cooling from an elevated temperature, the molar volume decreases gradually since the liquid state is usually less dense and larger volume than the solid state, either amorphous or crystal (A→B). If the liquid crystallizes, the molar volume significantly decreases at a melting temperature (T_m) due to solidification (B→E), and it decreases as decreasing the temperature again after the crystallization is completed (E→F). If the crystallization is avoided, the liquid changes to a supercooled state, and the rate of decrease in the molar volume does not change on passing through T_m (B→C or B→ C’). It is known that a rapid cooling avoids the crystallization since the molecules do not have time to form crystals and quickly form the supercooled liquid [58,64]. The viscosity of the glass continues to increase as decreasing the temperature, and the supercooled liquid freezes and meets the practical definition of solid referred to as glassy state at the viscosity of 10^{13} poise [57,62]. With a further decrease in temperature, the molar volume of the glass decreases but the degree of the change gets small since the thermal vibration amplitude gets small (C→D or C’→D’) [62]. The intersection temperature between the curve of the glassy state and that of the supercooled liquid is known as T_g. Since T_g location varies with the cooling rate, it is more accurate to call it a transformation range rather than fixed point. Below T_g

range, the glass structure does not relax, and the thermal expansion behavior is usually same as that of the crystalline solid. If a substance is a glass, the change of the molar volume should be observed at the T_g range during the heating and cooling reversibly.

Table 1-7. Comparison of glass synthesis methods [58]

Synthesis method	Standard quenching method	Rapid-quenching method	CVD method	Sol-gel method
Raw material	Mixture of powders	Mixture of powders	Metal compounds (powder)	Metal alkoxides (solution)
Initial process and the temperature	Fusion at 2200℃	Fusion at 2200℃	Oxidative decomposition of the spray liquid at 1400℃	Gelatinization at room temperature
Vitrification process and the temperature	Quenching of the liquid by room temperature	Rapid-quenching of the liquid by room temperature	Sintering of the fine powder aggregate at 1500–1600℃	Sintering of the gel at 800–1100℃
Rate of quench	1℃/sec	10^5–10^7℃/sec	-	-
Manufacturing facility	High temperature furnace and molding equipment	High temperature furnace and roller quencher	Sprayer, vapor phase reactor, or deposition apparatus	Flask, beaker, and low temperature furnace

The process temperature is an example of quartz glass.

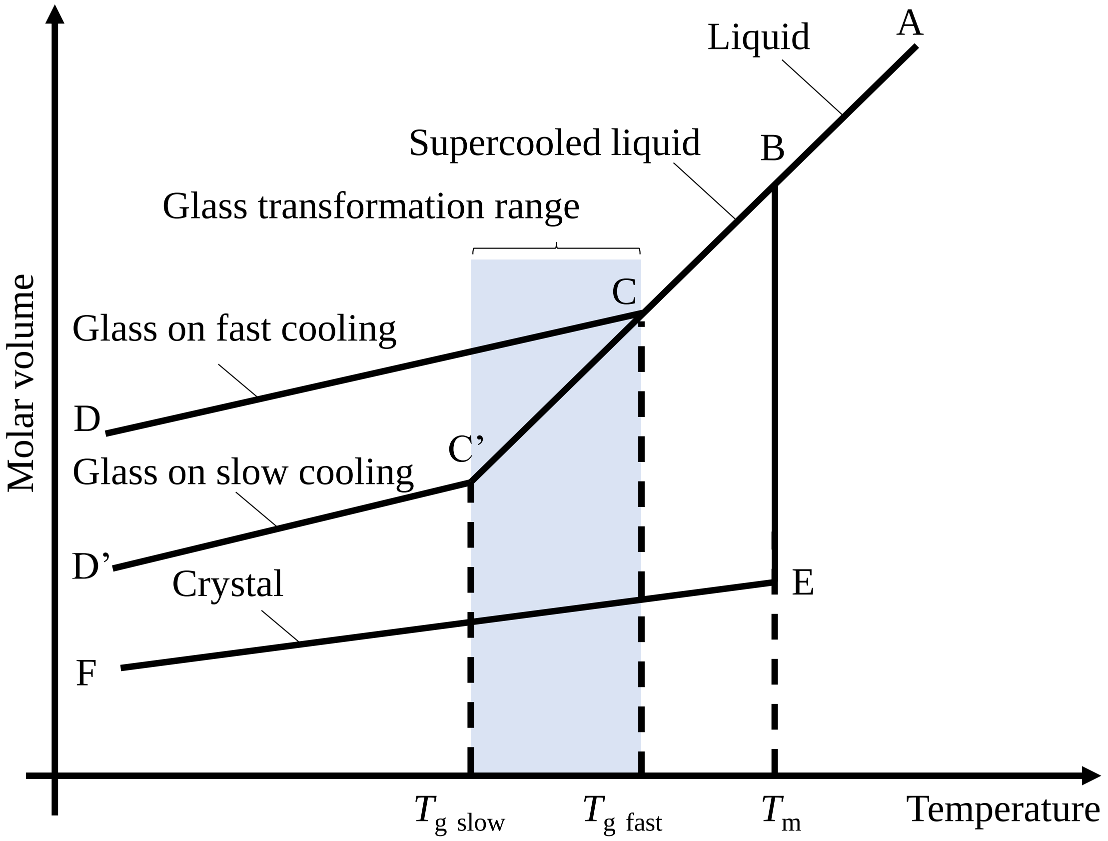

Figure 1-25. Schematic specific volume-temperature relationships for crystallization and glass formation [62–64].

1.5.3. Glass-Forming Oxides

There is not a single theory which is able to predict and specify which materials are able to form glasses. However, there are some theories and models which encompass most of the relevant aspects which are known to lead to glass formation in practice. According to Stanworth's rules, the elements, having the values of electronegativity on Pauling scale of 1.8–2.1 and the value of 1.5 Å (1 Å = 0.1 nm) or smaller atomic radius, are generally regarded as excellent glass formers [57,63,65]. For example, the electronegativity values of silicon, germanium, boron, and phosphorus are between 1.8 and 2.1, and the atomic radius of these elements are less than 1.3 Å [63]. These elements singly form silicate, germanate, borate, and phosphate glasses. W. H. Zachariasen postulates M–O bond between metal atom M and oxygen atom O forms three-dimensional continuous random network (3-D CRN) [57,62–64,66,67]. **Figure 1-26** shows the schematic two-dimensional (2-D) depiction of atomic arrangements in the 3-D CRN of oxide glass M_xO_y **(a)** and corresponding crystal **(b)**. Given that the interatomic forces and the nature of interatomic bonds are similar in the glass and corresponding crystal, four rules for the glass formation were led: 1) Each oxygen atom is bonded only to one or two glass-forming cations, 2) the oxygen coordination number around glass forming cation is small, generally three or four, 3) the oxygen polyhedra share corners, but those do not share edges or faces, and 4) the polyhedral structural units form a 3-D CRN in which at least three corners of each polyhedron should be shared [57,63,64,66]. Tricoordinate of M_2O_3 and tetracoordinate of MO_2 and M_2O_5 meet the rule 1–4) among M_2O, MO, M_2O_3, MO_2, M_2O_5, MO_3, M_2O_7, and MO_4 [63]. Those correspond to B_2O_3, SiO_2, GeO_2, P_2O_5, As_2O_3, As_2O_5, Sb_2O_3, and V_2O_5, and these metal oxides singly form glasses. However, this does not mean that metal oxides that fail to meet the abovementioned rules cannot form glasses. If the above criteria are met, the conditions for glass formation are favorable. Zachariasen's theory was led from the perspective of the crystal chemistry, whereas K. H. Sun made criteria on the basis of the idea that strong M–O bond is needed to form the 3-D CRN. Sun's criterion established a correlation between glass forming tendency and chemical bond strength in the glass. The single bond strength of M–O (ε) is expressed by [63]

$$\varepsilon = \frac{E_{\mathrm{D}}}{n}, \tag{1-15}$$

where E_{D} is dissociation energy of metal oxides into gaseous elements, and n is the oxygen coordination number. Sun noted that the metal oxides with ε of 80 kcal/mol or higher singly form the 3-D CRN so those are referred to as glass network former (NWF)

[62,63]. The NWF shows the high electronegativity and small ionic radius so the oxygen coordination number is small. Although the metal oxides with ε of 60 kcal/mol or less cannot singly form the 3-D CRN, those present as ions to alters the glass network, usually reducing glass network connectivity so those are referred to as glass network modifier (NWM) [62,63]. The NWM shows the low electronegativity and large ionic radius so the oxygen coordination number is high. The metal oxides, ε of which is between 60 kcal/mol and 80 kcal/mol, can play a role as the NWF and NWM, depending on glass composition so those are referred to as intermediate [62,63]. **Table 1-8** shows properties of metal oxides which form glasses. The Sun's model would suggest that stronger M–O bonds make it more difficult to rearrange the structure for crystallization in the quench process, as a result, the easier is glass formation.

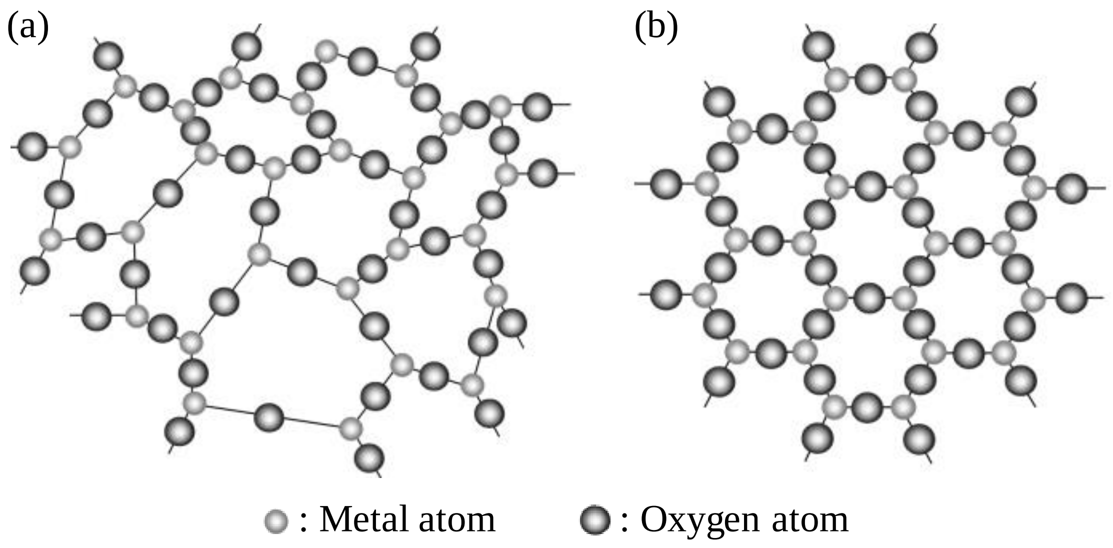

Figure 1-26. Schematic 2-D depiction of atomic arrangements: (a) 3-D CRN of oxide glass M_xO_y and (b) crystalline compound of the same substance [57,63,68,69].

Table 1-8. Properties of metal oxides which form glasses [62,63]

	M_xO_y	Valence	Electronegativity	Ionic radius (Å)	Oxygen coordination number	Single-bond strength (kcal/mol)
Network formers	B_2O_3	3+	2.0	0.15	3	119
	GeO_2	4+	1.8	0.53	4	108
	SiO_2	4+	1.8	0.40	4	106
	V_2O_5	5+	1.6	0.50	4	90–112
	P_2O_5	5+	2.1	0.31	4	88–111
	Al_2O_3	3+	1.5	0.53	4	79–101
	B_2O_3	3+	2.0	0.25	4	89
	As_2O_5	5+	2.0	0.48	4	70–87
	Sb_2O_5	5+	1.9	0.74	4	68–85
	ZrO_2	4+	1.4	0.86	6	81
Intermediates	TiO_2	4+	1.5	0.75	6	73
	PbO	2+	1.6	1.33	(2)	73
	ZnO	2+	1.6	0.74	(2)	72
	ThO_2	4+	1.3	1.08	8	64
	BeO	2+	1.5	0.41	4	63
	ZrO_2	4+	1.4	0.98	8	61
	Al_2O_3	3+	1.5	0.68	6	53–67
	CdO	2+	1.7	0.92	(2)	60
Network modifiers	Sc_2O_3	3+	1.3	0.88	6	60
	La_2O_3	3+	1.1	1.17	7	58
	Y_2O_3	3+	1.2	1.16	8	50
	SnO_2	4+	1.8	0.83	6	46
	Ga_2O_3	3+	1.8	0.76	6	45
	In_2O_3	3+	1.7	0.94	6	43
	ThO_2	4+	1.3	-	12	43
	PbO_2	4+	1.6	0.92	6	39
	MgO	2+	1.2	0.86	6	37
	ZnO	2+	1.6	0.74	4	36
	PbO	2+	1.6	1.33	4	36
	Li_2O	1+	1.0	0.90	4	36
	BaO	2+	0.9	1.49	8	33
	CaO	2+	1.0	1.26	8	32
	SrO	2+	1.0	1.40	8	32
	CdO	2+	1.7	0.92	4	30
	CdO	2+	1.7	1.09	6	20
	Na_2O	1+	0.9	1.16	6	20
	K_2O	1+	0.8	1.65	9	13
	Rb_2O	1+	0.8	1.75	10	12
	HgO	2+	1.9	1.16	6	11
	Cs_2O	1+	0.7	2.02	12	10

1.5.4. Simple Structural Theories of Glass Formation

The popular concept of the atomic structure of glass have traditionally been divided into crystallite model and continuous random network (CRN) model.

The crystallite model considers that glasses are formed of discrete regions of crystalline-like structure separated by regions of disorder, as shown in **Fig. 1-27** [57,62,66,67]. With this model, it was thought that the size distribution of the crystalline-like structure is complex, and it affects a melting temperature, consequently, glasses have a transformation range [57]. The crystallite model was first proposed by A. A. Lebedev (1921) and experimentally supported by J. T. Randall *et al.* (1930) [57,62,66,67]. The terms "tiny crystals" or "crystals" were originally used but the term "crystallite" was proposed by E.A. Pro-Koshits later to express the small size of regions with high atomic orderings in the random network [66,67].

The CRN model considers that oxide glasses are formed by an extended 3-D interconnected network that lacks symmetry and periodicity, as shown in **Fig. 1-26(a)** [57,63,68,69]. The structure consists of an interconnected network of metal atoms bonded to oxygen atoms in a tetrahedral configuration, and the individual tetrahedra link through sharing of the corner bridging oxygen atoms [66]. With this model, it was thought that the dissociation energy of each atom in the glass is slightly different, and the bonds between atoms are not broken simultaneously in the elevated temperature process, consequently, glasses have a transformation range [57]. The CRN model was proposed by W. H. Zachariasen (1932) and was experimentally supported by B. E. Warren (1934) [57,62–64,66,67]. The model contains no morphological and crystallite long-range order, and the network has a connectivity of 4, which is continuous and chemically ordered [66]. Furthermore, the structural parameters are statistically homogeneous (F. L. Galeener 1990) [66,70].

The CRN is modified by the addition of glass network modifier (NWM) or intermediate. With a quartz glass, the shared corner oxygen atoms are referred to as bridging oxygen (BO) atoms, and those are shared between two adjacent atoms of Si [57,63]. If Na_2O of NWM is added in SiO_2, Na^+ disrupts the connectivity of the network of SiO_2 tetrahedra, and it bonds to an oxygen atom of SiO_2 electrostatically [57,63]. Therefore, some oxygen atoms bond to both the glass network former (NWF) and NWM. Such oxygen atoms are referred to as non-bridging oxygen (NBO) atoms [57,63]. **Figure 1-28** shows SiO_2 glass network modified through the addition of Na_2O. The NBO atom increases as increasing the addition of Na_2O, and the structure of the glass opens more. Finally, excess addition of Na_2O prevents vitrification. The limit of the addition can be expressed using two equations [57,63]:

$$X + Y = Z, \tag{1-16}$$

$$X + \frac{1}{2}Y = R, \tag{1-17}$$

where X is the number of NBO atoms per one Si atom, Y is the number of BO atoms, Z is the coordination number of Si atom, and R is the ratio of O/Si. Since Z is four, the relationship between R, Z, and Y is expressed, as shown in **Table 1-9**. If Y is three or more, SiO_4 tetrahedra meet the Zhachariasen's rule, and stable glasses are formed. If Y is two, two corners of each polyhedron should be shared, consequently, the chained structure is formed, which suggests it is difficult to form glasses [57,63].

It is not concluded which model is closer to the structure of glass, the crystallite or CRN, but the CRN model is recently supported more than the crystallite model [62,66]. The comparison of glass structure and crystal structure should remain highly valuable for interpreting experimentally derived data on glass.

Table 1-9. Relationship between glass compositions and "R, X, Y" [57]

Glass composition	R	X	Y
SiO_2	2	0	4
$Na_2O \cdot 2SiO_2$	2.5	1	3
$Na_2O \cdot SiO_2$	3	2	2

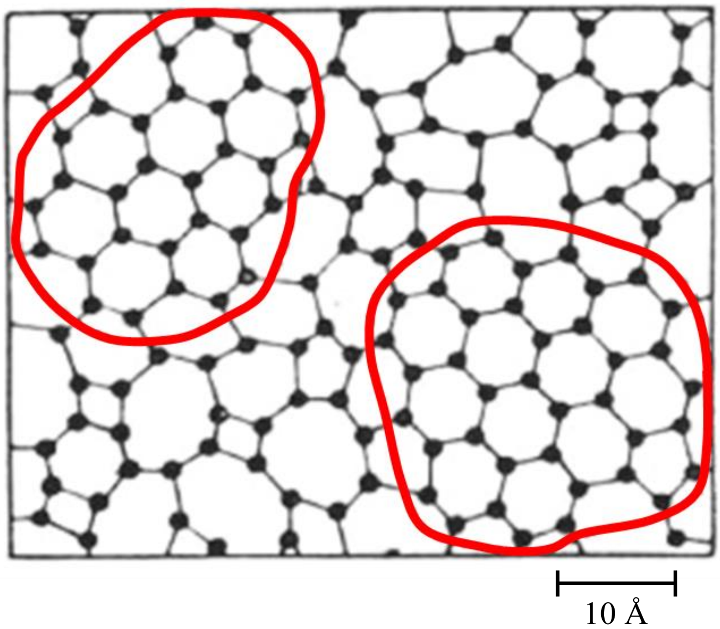

Figure 1-27. Glass structure of crystallite model [62]. The insides of the red circles are crystallite regions.

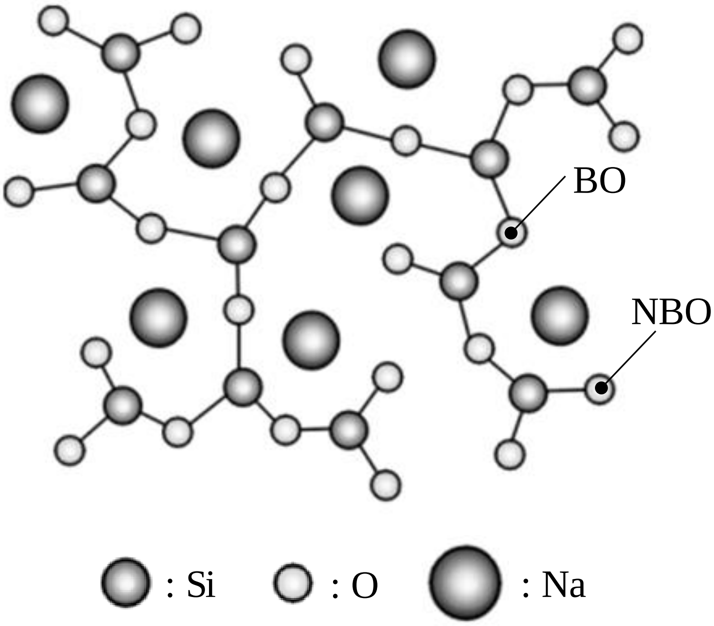

Figure 1-28. SiO_2 glass network modified through the addition of Na_2O [57,64,68,69].

1.5.5. Multi-Component Glasses

Multi-component glasses containing the glass network former (NWF), glass network modifier (NWM), and/or intermediate have been used in thick-film conductors for various applications. Since glass frits affect the function of thick-film conductors and the thick-film formation process, the formulation of glass frits is needed for each application. For oxide glasses, some trends for multi-component glass formation are known as follows: 1) in the binary system of NWFs, glasses are formed with any compositions unless the two-liquid immiscibility occurs above the liquidus curve, 2) it is hard to form glasses from NWMs and intermediates without NWFs, in addition, the glass forming ability generally decreases as decreasing the NWFs, and the glass formation range depends on which oxides are combined, 3) a high number of components is prone to form glasses without devitrification, and 4) the glass formation of multi-component glasses is related to the melting temperature and liquidus curve of crystals likely precipitated from the liquid, and the glass is prone to be formed around the eutectic point [63].

Various glass frits have been employed in conductor pastes but lead silicate and/or lead borosilicate glasses have been used extensively [2–4,15]. Pb is a unique element, and it cannot singly form a glass, but high amount of Pb can be accommodated in the glass [57,71–73]. Although the role of Pb in the structure is still debated, past studies suggest that Pb plays a dual structure role. Pb acts as a NWM such as alkali at low Pb content in silicate glass and borosilicate glass, whereas Pb acts as a NWF at high Pb content [73–76]. Furthermore, pyramidal PbO_4 and PbO_3 building units play a dominant role in reconstructing the network of borosilicate glasses by forming Pb–O–Si, Pb–O–Pb, and Pb–O–B bond, and the role of Pb changes to the NWF from the NWM with increasing Pb content [75]. High polarizability of Pb^{2+} enables to form the oxygen two coordination structure with asymmetric bonding, as shown in **Fig. 1-29** [71,72]. The bond of Pb–O in the glass network is directional, and it prevents SiO_2 from re-arrayal and crystallization [57]. Due to the abovementioned unique characteristics, Pb increases the glass forming range, and it facilitates melting of various metal oxides into glasses in a wider formulation range. It is also known that lead silicate and lead borosilicate glasses readily melt at low temperature [63,68,69,76]. **Table 1-10** shows the composition and properties of commercial glasses, and **Figure 1-30** shows the viscosity curves of the commercial glasses. The softening points of the lead-alkali silicate glasses are low in comparison to other glasses. It is also reported that the fraction of bridging oxygen (BO) and BO binding energy decreased with the increase in Pb content [73,77]. The glass transition temperature and viscosity decreased with the increase in PbO content [73]. These results mean that Pb can reduce the viscosity of glasses. Thick-film conductors containing low melting glasses can be fired in the wide firing temperature range. Therefore, lead silicate and/or lead borosilicate glasses have extensively been used for thick-film conductors.

Table 1-10. Composition and properties of commercial glasses in Fig. 1-30 (wt.%) [63,69]

Glass number in Fig. 1-30	Type	SiO_2	Na_2O	K_2O	CaO	MgO	PbO	B_2O_3	Al_2O_3	Annealing point (°C)	Softening point (°C)
1	Silicate glass	99.5+	-	-	-	-	-	-	-	1140	1667
2	96% silica glass	96.3	< 0.2	< 0.2	-	-	-	2.9	0.4	910	1500
3	Aluminosilicate glass	57	1.0	-	5.5	12	-	4	20.5	715	915
4	Soda-lime silicate glass (Sheet glass)	71–73	12–14	-	10–12	1–4	-	-	0.5–1.5	553	735
5	Borosilicate glass	80.5	3.8	0.4	-	-	-	12.9	2.2	565	820
6	Soda-lime silicate glass (Electric bulb)	73.6	16	0.6	5.2	3.6	-	-	1	510	696
7	Lead-alkali silicate glass	63	7.6	6.0	0.3	0.2	21	0.2	0.6	435	626
8	Lead-alkali silicate glass (High lead content)	35	-	7.2	-	-	58	-	-	430	580

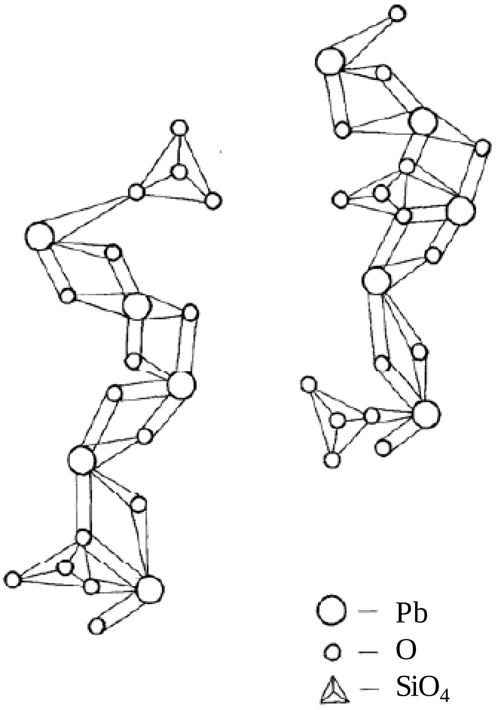

Figure 1-29. Model of lead silicate glass structure [72].

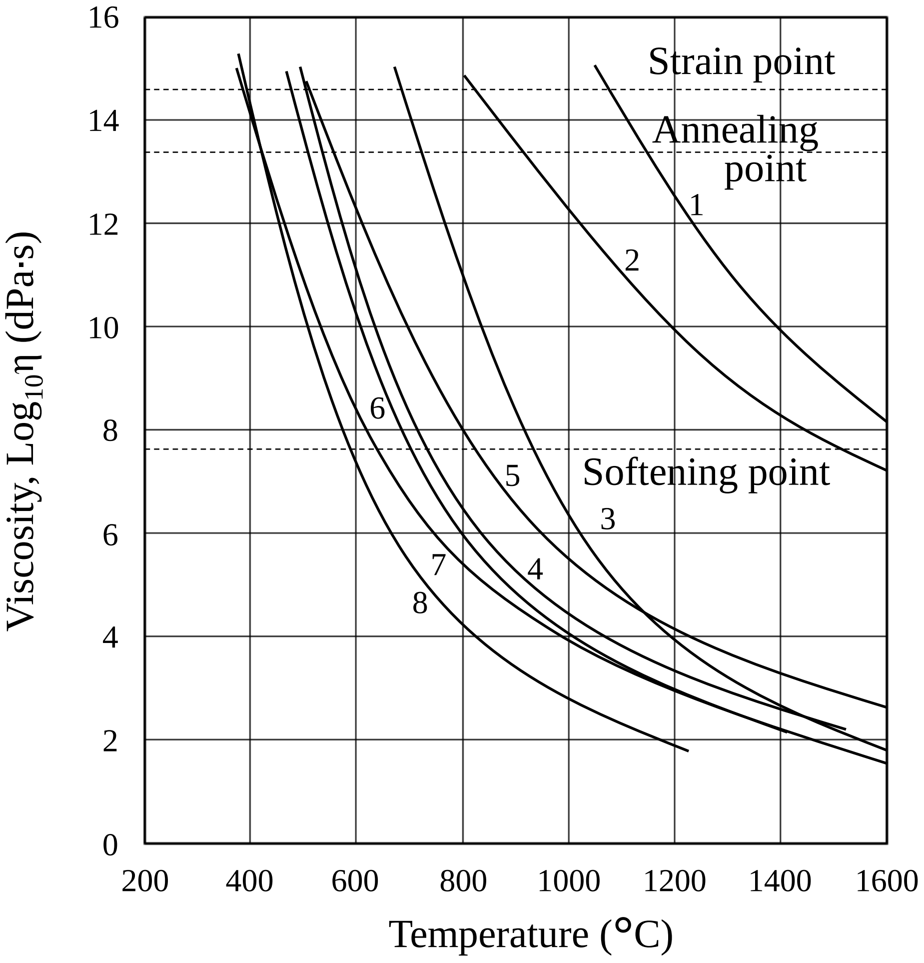

Figure 1-30. Viscosity curves of commercial glasses in Table 1-10 [63,68,69]: (1) silicate glass, (2) 96% silica glass, (3) aluminosilicate glass, (4), soda-lime silicate glass (sheet glass), (5) borosilicate glass, (6) soda-lime silicate glass (electric bulb), (7) lead-alkali silicate glass, and (8) lead-alkali silicate glass (high lead content).

1.5.6. Glass Ceramics

Crystallization of glass is not preferable for most applications (e.g., fiber, window, and display panel) because of the devitrification and the difficulty of control with the temperature and time. However, it is fact that glass ceramics have attracted a great deal of attention since Li_2O–Al_2O_3–SiO_2 glass ceramics were found by S. D. Stookey [57,60]. Glass ceramics are materials with an inorganic-inorganic microstructure which consists of one or more glassy and crystalline phases. The chemical composition and microstructure determine the properties of glass ceramics, and those enable to have unique properties such as almost zero thermal expansion, excellent mechanical, and/or chemical durability [57,60,78,79].

Crystallization of glass advances in three steps: 1) nucleation, 2) diffusion of atoms to the surface of nucleus in liquid, and 3) crystal growth [12,60,63]. The nucleation for glass ceramics is classified to homogeneous and heterogeneous nucleation, as shown in **Fig. 1-31** [12,60,63]. The nucleation process can be described in terms of a free energy change. The free energy of liquid is high in comparison to that of crystal, so the volume free energy decreases by the nucleation [12,60,63]. On the other hand, the generated nucleus forms a new interface in the liquid, which increases the surface free energy [12,60,63]. Therefore, the classical theory of the homogeneous nucleation gives the total free energy change (ΔG) per a spherical nucleus with a radius (r) as [12,60,63]

$$\Delta G = -\frac{4}{3}\pi r^3 \Delta G_x + 4\pi r^2 \sigma, \tag{1-18}$$

where ΔG_x is a free-energy change per unit volume associated with the transformation to the nucleus from the liquid, and σ is interfacial energy per unit area between the generated nucleus and liquid. ΔG is the largest at the radius of critical nucleus (r^*), and it reduces after exceeding r^*, as shown in **Fig. 1-32**. It means that the nuclei smaller than r^* are not stable, and those are generated and disappear repeatedly. However, the nuclei can stably grow after exceeding r^*. The thermodynamic barrier (ΔG^*) at r^* is defined as [12,60,63]

$$\Delta G^* = \frac{16\pi r^3}{3\Delta G_x^2}. \tag{1-19}$$

If heterogeneous interface exists, crystals grow at the interface which is referred to as heterogeneous nucleation. The thermodynamic barrier of the heterogeneous nucleation $(\Delta G^*_{\mathrm{hetero}})$ per a spherical-cap nucleus with a radius (r) on the interface is defined as [63]

$$\Delta G^*_{\mathrm{hetero}} = \frac{(2+\cos\theta)(1-\cos\theta)^2}{4}\frac{16\pi r^3}{3\Delta G_x^2}, \tag{1-20}$$

where θ is a contact angle of the spherical-cap nucleus on the interface. Since $(2 + \cos\theta)(1-\cos\theta)^2/4$ is between 0 and 1 in the range of $0 < \theta < \pi/2$, $\Delta G^*_{\mathrm{hetero}}$ is low in comparison to ΔG^*. Therefore, the nucleation is prone to advance in the heterogeneous nucleation easily in comparison to the homogeneous nucleation if the wettability of the nuclei to the liquid is good.

Figure 1-33 illustrates the schematic curves of nucleation rate (I) and crystal growth rate (U) as a function of temperature. With ΔG^*, I is defined as [12,60]

$$I = A\exp - \left[\frac{(\Delta G^* + \Delta E)}{kT}\right], \tag{1-21}$$

where A is a constant, ΔE is activation energy to diffuse atoms to the surface of nucleus in the liquid, k is a Boltzmann constant, and T is temperature. The number of nuclei is small at around the melting temperature (T_{m}), and it increases as the temperature closes to the glass transition temperature (T_{g}) [12,60]. On the other hand, the diffusion of atoms to the surface of nuclei increases as increasing the temperature. As a result, the peak of I appears between T_{g} and T_{m}. The crystal growth rate (U) is defined as [12,60]

$$U = \frac{D}{a}\left[1 - \exp\left(\frac{\Delta G_x}{kT}\right)\right], \tag{1-22}$$

where D is a diffusion coefficient, and a is a constant. The diffusion of atoms increases and ΔG_x decreases as increasing the temperature [12,60]. In addition, ΔG_x is equal to zero at T_{m} [12,60]. As a result, the peak of U appears between T_{g} and T_{m}, and it appears at higher temperature than that of I. Therefore, the annealing in the overlapping region of I and U in **Fig. 1-33** promotes the crystallization of glass. In other words, the crystallization of glass can be avoided by cooling the glass melt as rapidly as possible in the overlapping temperature range.

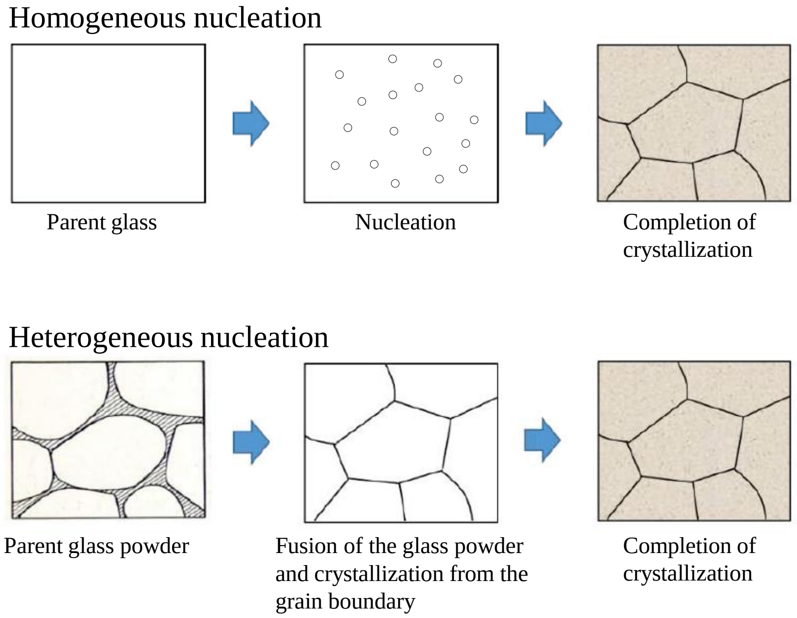

Figure 1-31. Nucleation process of glass ceramics [60,78].

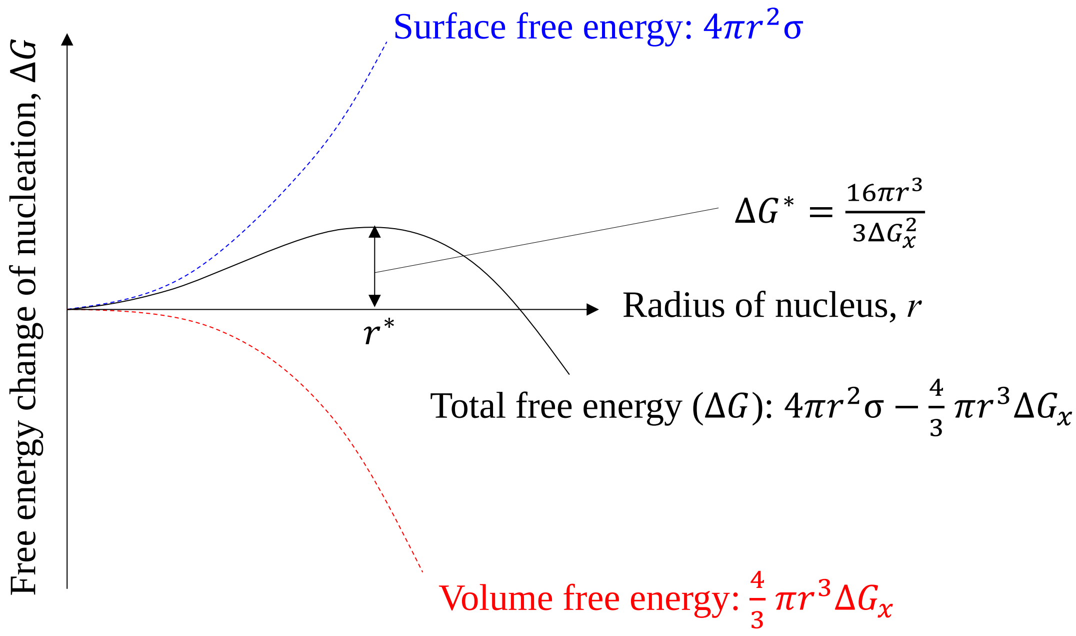

Figure 1-32. Free energy change of nucleation on the assumption that the nucleus is spherical [12,60,63].

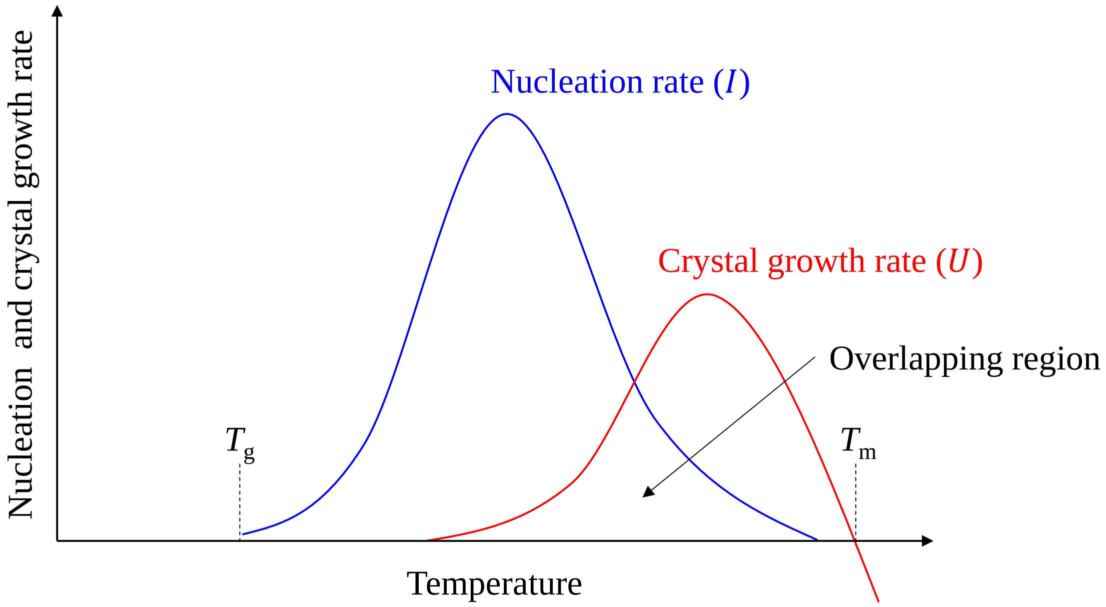

Figure 1-33. Schematic curves of nucleation and crystal growth rate as a function of temperature [12,60,63].

1.6. Global Market for Thick-Film Materials

1.6.1. Market Share of Thick-Film Materials

Thick-film materials have been used in electronics industry for over the past 50 years. It is clear that the thick-film materials have considerably contributed to the development of electronic devices in many segments: medical, telecommunications, automotive, aerospace, and consumer electronics [2]. On the other hand, thin-film technology also has contributed to the electronics industry. Although the definition of the thick film and thin film by the thickness is not clear, it is said that the thick film generally targets on the thickness between 5 μm and 25 μm, whereas the target thickness of thin film is approximately less than 5 μm [28,45]. **Figure 1-34** shows the global market share of thick films and thin films in electronic products. The others include nano films and ultrathin films of which thickness is thinner than 100 nm. The thick-film material is one of the oldest circuit materials, but it still accounts for a large share in the market. The excellent mass productivity, low cost, and high reliability of thick-film materials should retain considerable attention in electronics industry for a long period.

1.6.2. Global Market Trend of Thick-Film Materials by Application

The major applications of thick-film materials are photovoltaic devices, electronic components, circuit boards, low temperature co-fired ceramics, automotive parts, and sensors including chemical and physical sensors [45]. Photovoltaic devices are a top application, and electronic components and circuit boards come next, as shown in **Fig. 1-35**. The top three applications are explained in the below paragraphs.

Photovoltaic devices are renewable source of energy, and it is mega trend of technology to improve the environmental issue. Thick-film conductors are used as the front and back side electrode of crystalline silicon photovoltaic cells extensively. **Figure 1-36** illustrates the structure of a typical p-type crystalline silicon photovoltaic cell. The Ag thick-film conductor is used as the finger electrode contacting on the n^+ emitter of phosphorus doped Si where is generally referred to as the front side of the photovoltaic cell. On the other hand, the Al thick-film conductor is used as the back-side electrode contacting on the boron doped Si.

Electronic components are classified to active and passive component. The active components require an external energy source to operate, and the typical active components are transistors, diodes, and semiconductors [1,81]. On the other hand, the passive components do not require an external energy source to operate, and the typical passive components are resistors, capacitors, and inductors [1,81]. The thick-film materials are mainly used for passive components. For example, **Fig. 1-37** illustrates a passive surface-mount chip component, and it has a rectangular shape and electrode termination [1,38]. In case of the chip resistor, the thick-film conductor, resistor, and insulator are used as the electrode termination, resistor, and overcoat, respectively [1,38].

Circuit boards mechanically support and electrically connect electronic components. The thick-film conductor, resistor, and insulator are used as conductors and functional elements on the circuit board [1].

1.6.3. Market Assessment of Thick-Film Materials by Intellectual Property

Figure 1-38 shows the number of patent families about thick-film materials until 2017. Although the number was not high in 1960s, it significantly increased from 1980s, and about 150 or more patents have been applied every year since 1994. **Figure 1-39** shows patent families about thick-film materials by protection country in 2019. It suggests that many applications designed with thick-film materials are developed and/or produced in China, United State of America, Japan, and Taiwan.

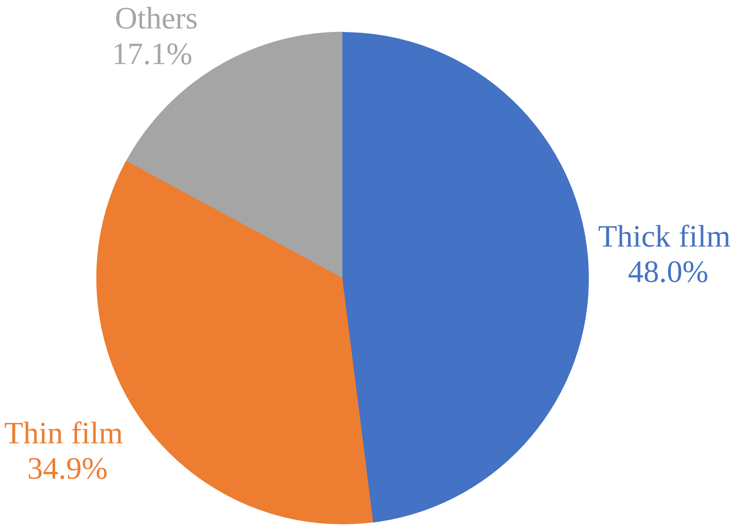

Figure 1-34. Global market share for thick films and thin films in electronic products in 2017 [45].

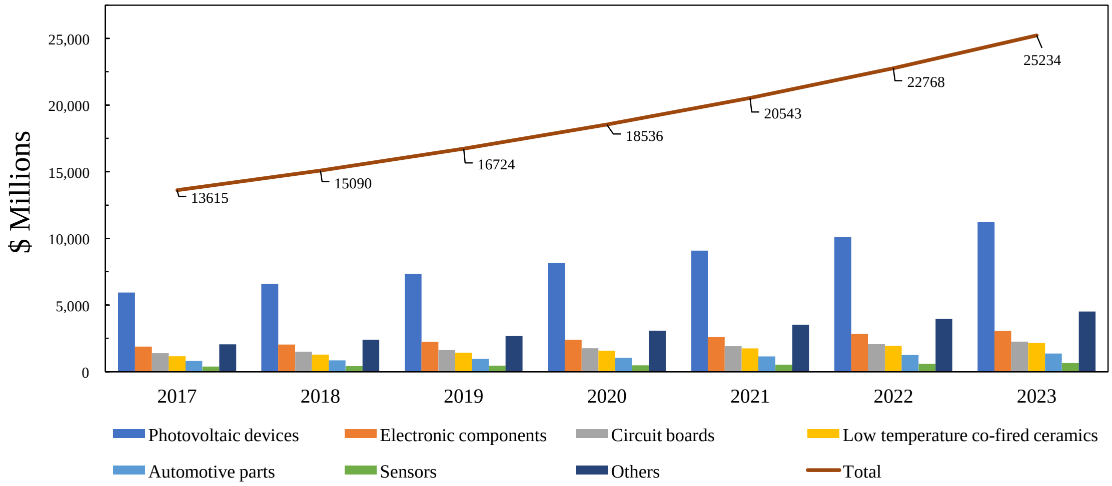

Figure 1-35. Global market for thick-film materials by application [45].

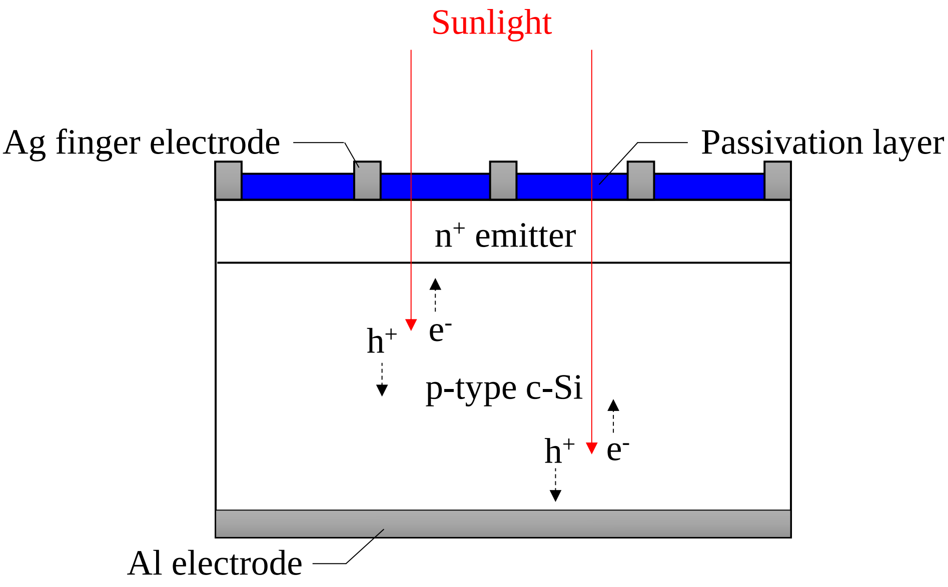

Figure 1-36. Structure of a typical p-type crystalline silicon photovoltaic cell [80].

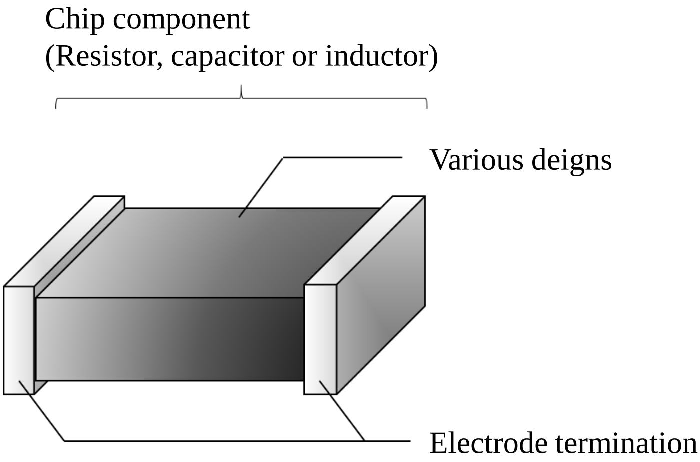

Figure 1-37. Schematic depiction of a typical surface-mount chip component [1,38].

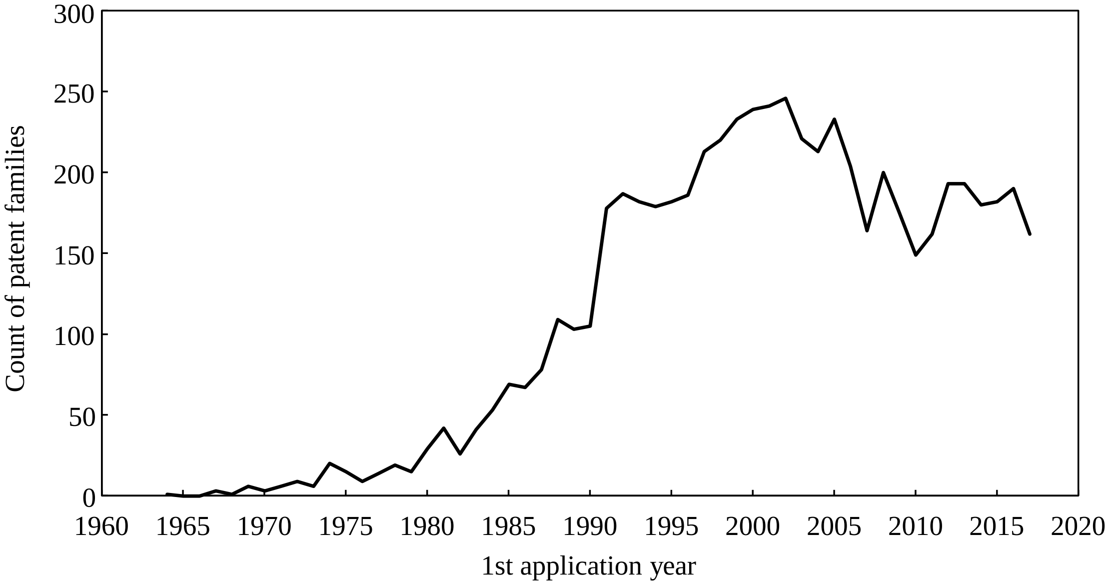

Figure 1-38. The number of patent families about thick-film materials until 2017.

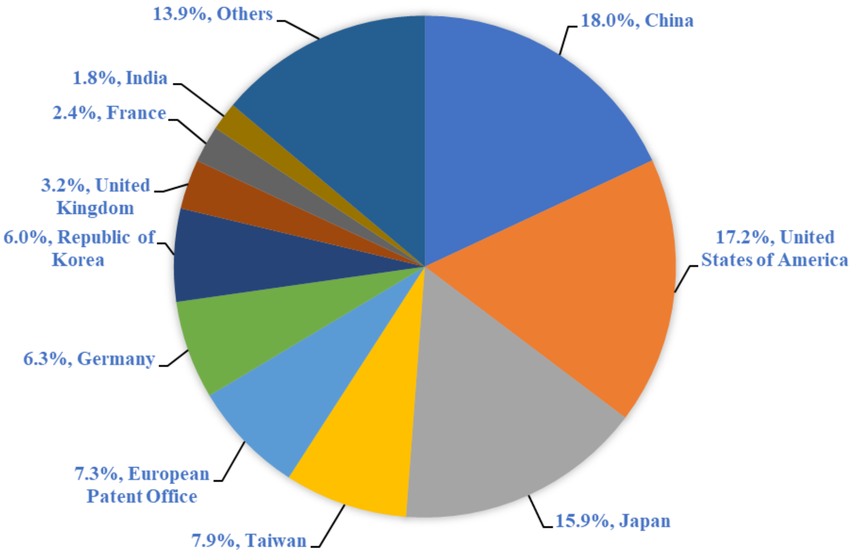

Figure 1-39. Patent families about thick-film materials by protection country in 2019.

1.7. Purpose of This Study

Glass frits in conductor pastes promote the sintering of metal powders during the firing process and binding of the metal film to the substrate. Therefore, low-melting glasses are suitable for thick-film conductors, and lead borosilicate glasses have been extensively used. Recently, material design with Sustainable Development Goals is becoming important, and further function control of thick-film conductors is required. This study takes the Pb-free request for environment and health and the request of photovoltaic cells as renewable source of energy.

The purpose of this study is to investigate the effect of glass frit composition on the chemical durability and electrical properties of Ag thick-film conductors, and build new underlying technology for Ag thick-film conductors by controlling the interfacial glass layer between the thick-film conductor and substrate. Since the performance requirement for thick-film conductors depends on the application, fabrication process of the electronic components and circuits, and those designs, it is needed to control the function for each of the requests. At first, glass frits are prepared, and the properties are characterized in Chapter 3. Next, those are examined in Ag thick-film conductors in Chapter 4 and 5.

Chapter 4 presents "Effect of Micro-Crystallization of Alkali and Alkaline-Earth Borosilicate (AEB) Glass on Acid Durability of Ag Thick-Film Conductor". Pb-free electronic materials are environmentally required but that makes a problem of acid durability of electroplated Ag thick-film conductors in acidic solutions since high acid durability is a challenging for most low-melting Pb-free glasses. In addition, there are few studies on the chemical durability of thick-film conductors under acidic conditions.

Chapter 5 presents "Reduction in Contact Resistivity of Ag Thick-Film Conductor on SiN_x-Coated Si Wafer Using Lead Tellurite (PT) Glass Frit" It is still difficult to remove Pb in Ag thick-film conductors for photovoltaic cells, while further lowering of the contact resistivity on SiN_x-coated Si wafers is required for Ag thick-film conductors to improve the photo-conversion efficiency and increase the renewable source of energy. There have been numerous reports on the contact formation mechanism and the microstructure analysis of Ag thick-film conductors containing lead borosilicate glass frits but it is difficult to improve the contact resistivity further. In addition, there are few studies on the correlation between the properties of glass frits and the contact resistivity of Ag thick-film conductors except lead borosilicate glass frits.

References

[1] N. White, *Springer Handbook of Electric and Photonic Materials*, Eds. by S. Kaap and P. Chapper, Springer International Publishing, Switzerland, pp.707–721 (2017).

[2] J. R. Larry, R. M. Rosenberg, and R. O. Uhler, *IEEE. T. Compon. Hybr.*, **3**(2), pp.211–225 (1980).

[3] R. G. Loasby, P. J. Holmes, J. Savage, W. A. Crossland, L. Hailes, P. F. T. Linford, J. B. McCloghrie, and H. D. Fisher, *Handbook of Thick Film Technology*, Eds. by P. J. Holmes and R. G. Loasby, Electrochemical Publications, Scotland, pp.1–79, pp.97–136, pp.153–154, pp.164–169, and pp.274–332 (1976).

[4] N. Sugimoto, *HIC Peisuto Zairyo to Insatsu-Shosei Gijutsu* (*HIC Paste Materials and Print-Firing Technology*), Japan Association for International Chemical Information, Japan, pp.27–80, pp.83–95, and pp.109–110 (1989) [in Japanese].

[5] B. E. Taylor, J. J. Felten, S. J. Horowitz, J. R. Larry, and R. M. Rosenberg, *Electrocomp. Sci. Tech.*, **9**, pp.67–85 (1981).

[6] M. L. Topfer and J. Piper, *J. Electrochem. Soc.*, **119**, p156C (1972).

[7] A. A. Milgram, *Metallurgical Transactions*, **1**. pp.695–700 (1970).

[8] S. Achmatowicz1 and E. Zwierkowska, *MATERIA"Y ELEKTRONICZNE*, **34**, pp.5–47 (2006).

[9] N. Uchitomi, *Handotai ga Ichiban Wakaru* (*Semiconductor*), Gijutsu-Hyohron, Japan, pp.14–15 and pp.22–23 (2014) [in Japanese].

[10] S. Park, C. Kim, W. Lee, S. Sung, and M. Yoon, *Mater. Sci. Eng. R*, **114**, pp.1–22 (2017).

[11] S. C. Mishra, *Global Journal of Engineering Science and Researches*, **1**(9), pp.32–44 (2014).

[12] A. Kamegawa, *Ceramic Material Science*, Muroran Institute of Technology, Japan, pp.59–62, pp.65–85, and pp.97–111 (2019).

[13] K. Tanaka, *Solid Chemistry*, Tokyo Kagaku Dojin, Japan, pp.218–239 and pp.240–252 (2019).

[14] C. Tapeinos, *Smart Nanoparticles for Biomedicine*, Ed. by G. Ciofani, Elsevier, Netherlands, pp.131–142 (2018).

[15] C. Jiro and S. Nagahara, *Hybrids*, **2**(3), pp.2–9 (1986).

[16] M. Munakata, *The Journal of The Institute of Electrical Engineers of Japan*, **75**(806), pp.1389–1394 (1955).

[17] M. Tatsumisago, *New Glass*, **23**(2), pp.46–53 (2008).

[18] K. Kanaizuka, M. Kurihara, H. Ueda, and T. Mori, *Handbook of Chemistry: Pure Chemistry 6th ed.*, Ed. by The Chemical Society of Japan, Maruzen Publishing, Japan, pp.110–119 and pp.1023–1025 (2021).

[19] M. V. Coleman and G. E. Gurnett, *Electrocomp. Sci. Tech.*, **5**, pp.55–59 (1978).

[20] H. Okamoto, *Phase Diagrams for Binary Alloys*, Eds. by M. A. Fleming and C. McNeill, ASM International, USA, p3 and p15 (2000).

[21] A. Uruena, J. Horzel, S. Singh, I. Kuzma-Filipek, E. Cornagliotti, J. John, R. Mertens, and J. Poortmans, *Energy Procedia*, **27**, pp.561–566 (2012).

[22] A. Tanaka, *Kinzokufun no Erabikata Tsukaikata* (*Handbook of Metal Powders*), Ed. by Y. Aoki, Technical Information Institute, Japan, pp.66–72 (2010) [in Japanese].

[23] S. Honma, *Purasuchikku Zairyo Taizen* (*Handbook of Plastic Materials*), Nikkan Kogyo Shimbun, Japan, pp.10–13 (2015) [in Japanese].

[24] K. Hida, *J. Surf. Finish. Soc. Jpn.*, **69**(2), pp.73–79 (2018).

[25] M. Ohwa, *Journal of Printing Science and Technology*, **40**(3), pp.168–175 (2003).

[26] H. Kimura, M. Date, and J. Yamamoto, *Journal of Network Polymer, Japan*, **28**(3), pp.101–108 (2007).

[27] S. Iyoshi, H. Miyake, K. Nakamatsu, and S. Matsui, *J. Photopolym. Sci. Technol.*, **21**(4), pp.573–581 (2008).

[28] N. Baba, *Shikizai*, **72**(1), pp.51–60 (1999).

[29] D. D. Liu and M. J. Sampson, presented at *CARTS International*, pp.59–71 (2012).

[30] G. Radosavljevic and W. Smetana, *Printed Films*, Eds. by M. Prudenziati and J. Hormadaly, Woodhead Publishing, UK, pp.429–468 (2012).

[31] K. Maeda and T. Manabe, *New Glass*, **12**(2), pp.27–32 (1996).

[32] T. Fujiwara, T. Haranoh, and H. Ishikawa, *J, Vac. Soc. Jpn.*, **41**(7), pp.608–612 (1998).

[33] J. Fukuta, S. Ooiwa, M. Fukaya, and H. Araki, *J. Ceram. Assoc. Japan*, **47**(7), pp.550–551 (2012).

[34] J. Fukuda, *J. Ceram. Assoc. Japan*, **42**(10), pp.795–797 (2007).

[35] T. Mutoh and T. Honda, *Hybrid IC Technology*, Ed. by Electronics Material, Kogyo Chosakai Publishing, Japan, pp.40–45 and pp.51–57 (1984).

[36] K. Hayashi, R. Yuasa, and K. Inami, *Quality Engineering*, **13**(3), pp.68–74 (2005).

[37] R. Hoenig, *Dr. Thesis*, Faculty of Engineering, Albert-Ludwigs-Universität Freiburg, Germany (2014).

[38] T. Ishida, Y. Tsujimoto, H. Ikebe, and T. Kuroda, *Surface Mount Technology*, Eds. by I. Masuyama and T. Honda, Kogyo Chosakai Publishing, Japan, pp.15–33 and pp.65–74 (1986).

[39] T. Uno and K. Tatsumi, *J. Japan Inst. Metals*, **63**(3), pp.406–415 (1999).

[40] T. Osawa, *J. Japan Inst. Electron. Packag.*, **5**(3), pp.304–309 (2002).

[41] K. Tashiro and M. Saito, *Mekki Taizen* (*Handbook of Plating*), Ed. by Kanto-gakuin University, Nikkan Kogyo Shimbun, Japan, pp.183–197 and pp.228–243 (2018) [in Japanese].

[42] T. Hashimoto, *J. Surf. Finish. Soc. Jpn.*, **61**(2), p198 (2010).

[43] M. Suzuki, *J. Vac. Soc. Jpn.*, **57**(8), pp.303–307 (2014).

[44] K. Shinoda and J. Akedo, *J. Surf. Finish. Soc. Jpn.*, **69**(11), pp.478–484 (2018).

[45] *Thick Film Materials: Global Markets to 2023*, BCC Research, USA, p21, p22, and p38 (2018).

[46] *Insatsu Erekutoronikusu Sentan Gijutsu no Kokunaigai Gijutsudoko no Purojekuto Chousa* (*Project Research of Domestic and International Technology Trend of Advanced Printed Electronics*), The Association for the Progress of New Chemistry, Japan, pp.3–13 (2010) [in Japanese].

[47] Y. Sano and S. Shimoyama, *Basic & Application of Advanced Screen Printing Techniques for Electronics*, Ed. by Y. Sano, CMC Publishing, Japan, pp.1–18 and pp.49–70 (2011).

[48] K. Koseki, Y. Sano, Y. Morotomi, D. Adachi, T. Kudo, N. Takada, Y. Sano, H. Yoshida, K. Koyama, and Y. Hino, *Journal of Printing Science and Technology*, **45**(5), pp.414–434 (2008).

[49] A. A. Tomchenko, *Thick-Film Semiconductor Chemical Sensors*, Eds. by C. A. Grimes, E. C. Dickey, and M. V. Pishko, American Scientific Publishers, USA, **10**, pp.279–290 (2006).

[50] D. He and N. N. Ekere, presented at *Proceeding from Electronics Components and Technology Conf.*, pp.142–146 (2000).

[51] T. Nakamichi, *Ganryo Bunsan* (*Pigment Dispersion*), Nikkan Kogyo Shimbun, Japan, pp.21–26 and pp.128–151 (2009) [in Japanese].

[52] S. N. Ivanov, P. A. Popov, G. V. Egorov, A. A. Sidorov, B. I. Kornev, L. M. Zhukova, and V. P. Ryabov, *Phys. Solid State*, **39**(1), pp.81–83 (1997).

[53] C. Bala, L. Rotariu, C. Ionescu, and P. Svasta, presented at *15th International Symposium for Design and Technology of Electronics Packages*, pp.325–330 (2009).

[54] *ASTM C162*, ASTM international, USA, p7 (2005).

[55] *McGraw-Hill Dictionary of Science and Technical Terms, Fourth Edition*, Eds. by S. P. Parker *et al.*, McGraw-Hill, USA, p810 (2000).

[56] K. Ohta, *Journal of the Illuminating Engineering Institute of Japan*, **24**(12), pp.50–57 (1940).

[57] S. Tsuchihashi, *Chemistry of Glass*, Kodansha, Japan, pp.9–16, pp.51–55, pp.71–106, and pp.157–168 (1988).

[58] S. Sakka, *New Glass*, (5), pp.27–39 (1987).

[59] K. Makita, *Resources Processing*, **37**(2), pp.93–100 (1990).

[60] T. Honma, *New Glass*, **26**(103), pp.33–37 (2011).

[61] T. Uwabe, *Tiri News*, Tokyo Metropolitan Technology Research Institute, Japan, pp.4–5 (2006).

[62] F. Yanagisawa, *Min. Geol.*, **40**(5), pp.353–362 (1990).

[63] M. Yamane, *Hajimete Garasu wo Tsukuruhito no Tameni* (*Handbook of Glasses*), Uchida Rokakuho Publishing, Japan, pp.1–24, pp.47–61, and pp.165–177 (2005) [in Japanese].

[64] M. Hasanuzzaman, A. Rafferty, M. Sajjia, and A. G. Olabi, *Ref. Modul. Mater. Sci. Mater. Eng.*, Elsevier, Netherlands, pp.1–12 (2016).

[65] J. E. Stanworth, *Nature*, **169**, pp.581–582 (1952).

[66] G. S. Henderson, *The Canadian Mineralogist*, **43**, pp.1921–1958 (2005).

[67] E. A. Porai-Koshits, *J. Non-Cryst. Solids*, **123**, pp.1–13 (1990).

[68] M. Yamane and Y. Asahara, *Glass for Photonics*, Cambridge University Press, UK, pp.1–8 (2000).

[69] E. B. Shand, *Glass Engineering Handbook 2nd ed*, McGrraw-Hill, USA, pp.3–22 (1958).

[70] F. L. Galeener, *J. Non-Cryst. Solids*, **123**, pp.182–196 (1990).

[71] R. Terai, *Mater. Integr.*, **17**(1), pp.51–55 (2004).

[72] N. J. Kreidl, *Glass: Science and Technology*, Eds. by D. R. Uhlmann and N. J. Kreidl, Academic Press, USA, pp.155–158 (1983).

[73] I. B. Kacem, L. Gautron, D. Coillot, and D. R. Neuville, *Chemical Geology*, **461**, pp.104–114 (2017).

[74] F. Fayon, C. Bessada, D. Massiot, I. Farnan, and J. P. Coutures, *J. Non-Cryst. Solids*, **232–234**, pp.403–408 (1998).

[75] G. El-Damrawi and E. Mansour, *Physica B*, **364**, pp.190–198 (2005).

[76] T. S. Petrovskaya, *Glass and Ceramics*, **54**, pp.347–350 (1997).

[77] B. M. J. Smets and T. P. A. Lommen, *J. Non-Cryst. Solids*, **48**, pp.423–430 (1982).

[78] *Science of Glass*, Ed. by New Glass forum, Nikkan Kogyo Shimbun, Japan, pp.88–91 (2013).

[79] M. Tashiro, S. Sakka, and T. Yamamoto, *J. Ceram. Assoc. Jpn.*, **71**(7), pp.152–157 (1963).

[80] J. F. Gray, *Handbook of Photovoltaic Science and Engineering*, Eds. by A. Luque and S. Hegedus, John Wiley & Sons, UK, p83 (2011).

[81] H. Akiyama, *Hybrids*, **4**(1), pp.19–20 (1988).

Chapter 2

Analytical Instruments and Methods

2.1. Evaluation Process of Ag Thick-Film Conductors

Figure 2-1 shows the basic evaluation process of Ag thick-film conductors. At first, thermal behavior and physical properties of glass frits were characterized in Chapter 3. Next, glass pastes or Ag conductor pastes were prepared by mixing and dispersing the glass frits, Ag powders, and/or metal oxides with an organic vehicle using a roll-milling machine, and then thick films were formed by screen-printing the pastes onto substrates. After the annealing process, the microstructure, chemical durability, and electric properties of the thick films were characterized in Chapter 4 and 5.

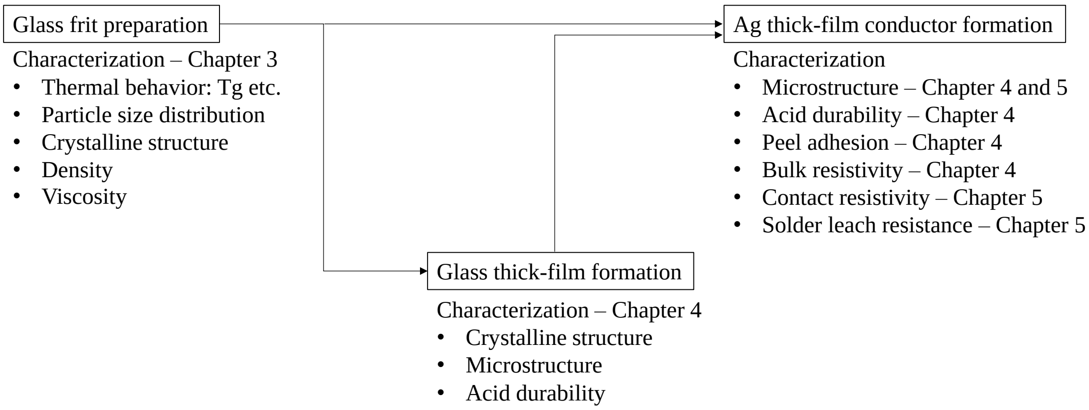

Figure 2-1. Basic flow chart of Ag thick-film conductor evaluation process.

2.2. Analytical Instruments for Characterization of Glass Frits

2.2.1. Thermogravimeter-Differential Thermal Analyzer

Thermogravimeter-differential thermal analyzer (TG/DTA) characterizes multiple thermal properties of a sample. The TG component measures weight changes associated with chemical changes (e.g., dehydration, decomposition, oxidization, and reduction) and physical changes (e.g., evaporation, sublimation, adsorption, and desorption) [1]. The DTA component measures the difference in temperature between the sample and reference [1]. The endothermic or exothermic peak of DTA is corresponding to the phase, chemical, and physical change. **Figure 2-2** illustrates the measurement principle of the TG/DTA. The TG and DTA are generally measured simultaneously. The thermal behavior of the glass frits was examined by a TG/DTA (TG/DTA6300, SII Nano Technology) in air in this thesis. The glass transition temperature (T_g) was obtained from the 1st exothermic peak of DTA, as shown in **Fig. 2-3**. Furthermore, the crystallization peak (T_c) and melting temperature (T_m) were obtained from the exothermic peak of DTA and the endotherm peak after T_c, respectively.

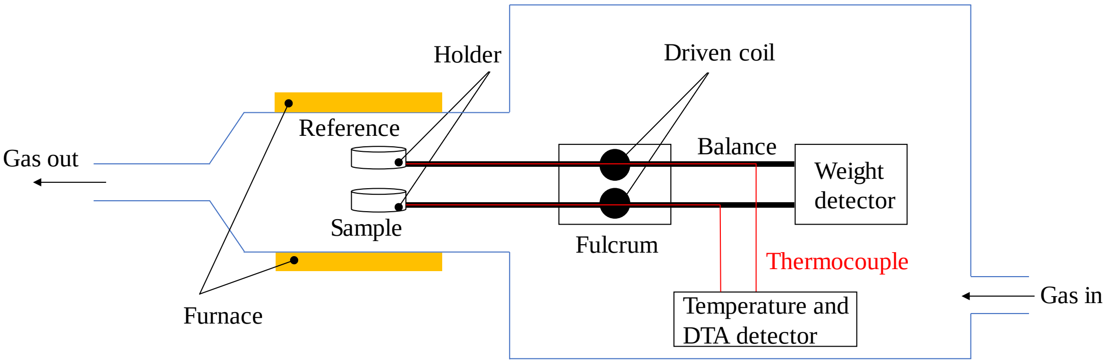

Figure 2-2. Measurement principle diagram of the horizontal TG/DTA [1,2].

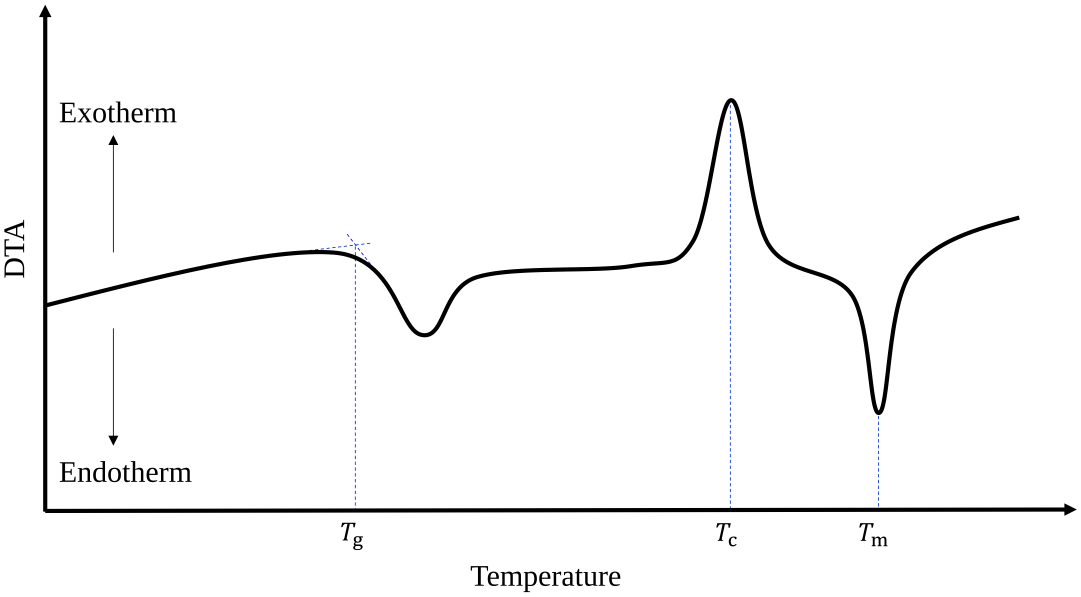

Figure 2-3. T_g, T_c, and T_m obtained from DTA curve [3].

2.2.2. Laser Scattering Particle Distribution Analyzer

The average particle size of the glass frits was examined by a laser scattering particle distribution analyzer (LA920, Horiba). This method measures the particle size distribution by measuring the angular variation in intensity of light scattered as a laser beam passes through a sample, as shown in **Fig. 2-4**. The spatial intensity distribution pattern depends on the particle size, as shown in **Fig. 2-5**. When the laser irradiates the particle, if the particle size exceeds the wavelength of the laser, most of the particles will scatter the light in the same direction as the laser light (forward scattering) [5]. On the other hand, when the particle size is almost the same or smaller than the wavelength of the light, the scattered light increases in the perpendicular direction (lateral) and in the direction towards the light source (backward) [5]. The ring detector is for detecting the forward scattered light, and the side and back detectors are for detecting the backward and other scattered lights. The scattering intensity (I_θ) can be calculated from the scattering pattern using Mie scattering theory defined as [6]

$$I_\theta = \frac{I_0 \lambda^2}{8\pi^2 R^2}\{i_1(\theta, m, \alpha) + i_2(\theta, m, \alpha)\}, \tag{2-1}$$

where I_0 is the light intensity before the interaction with particles, λ is a wavelength of the light, R is a distance between the particles, θ is a scattering angle, m is a relative refractive index, α is a particle size parameter, i_1 means the function of the perpendicular component to the scattering plane, i_2 means the function of the horizontal component to the scattering plane.

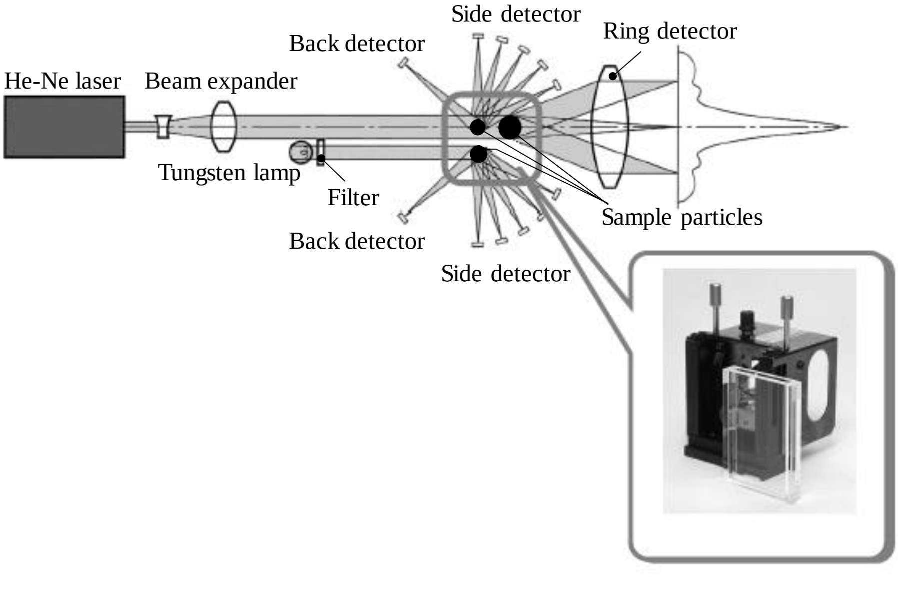

Figure 2-4. Measurement principle diagram of the laser scattering particle distribution analyzer [4].

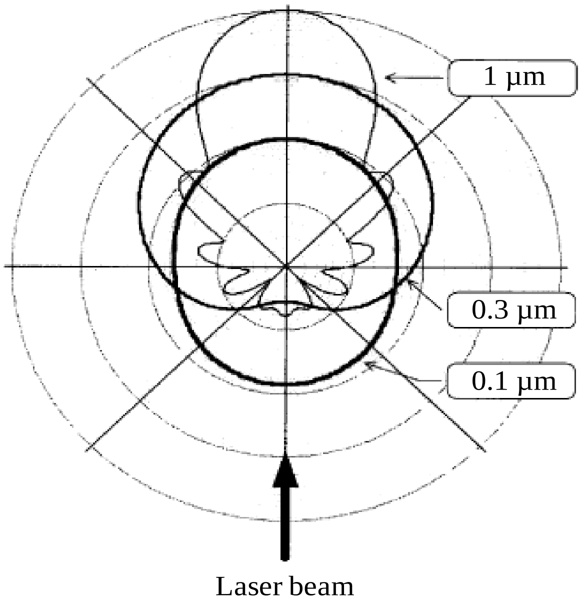

Figure 2-5. Relationship between particle size and scattered light intensity distribution [5].

2.2.3. X-Ray Diffraction Instrument

X-ray diffraction (XRD) is non-destructive technique primarily used for phase identification of a crystalline material, and it can provide information on unit cell dimensions. For example, quartz, cristobalite, and silica glass are all different phases of SiO_2, and these materials show the different X-ray diffraction patterns, as shown in **Fig. 2-6**. Amorphous materials like glass do not show sharp diffraction peaks, and the diffraction pattern of a mixture is a simple sum of the diffraction patterns of each individual phase [7,8]. The generated X-rays are generally filtered to produce monochromatic radiation, collimated to concentrate, and directed toward a sample [9]. After the incident X-rays are irradiated to the sample, the X-ray diffraction happens when the condition satisfies Bragg's law defined as [9]

$$n\lambda = 2d\sin\theta, \qquad (2\text{-}2)$$

where n is an integer, λ is a characteristic wavelength of the X-rays impinging on the crystallize sample, d is interplanar spacing between rows of atoms, and θ is an angle of the X-ray beam with respect to these planes. **Figure 2-7** illustrates Bragg's low. These diffracted X-rays are then detected and counted to identify the phase of the sample. In this thesis, a XRD instrument (D8, Bruker) with a monochromator employing Cu-Kα$_1$ radiation (λ = 1.5406 Å) was used for the characterization of the glass frits and thick films.

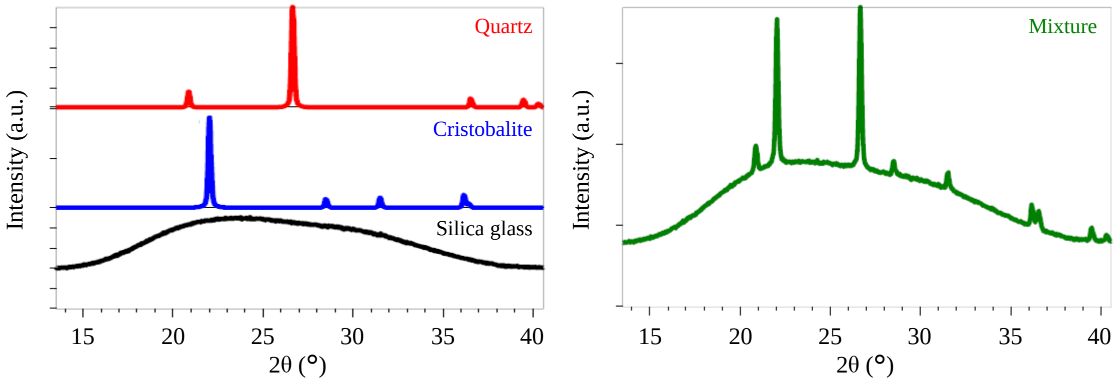

Figure 2-6. XRD patterns of quartz, cristobalite, silica glass, and the mixture [7].

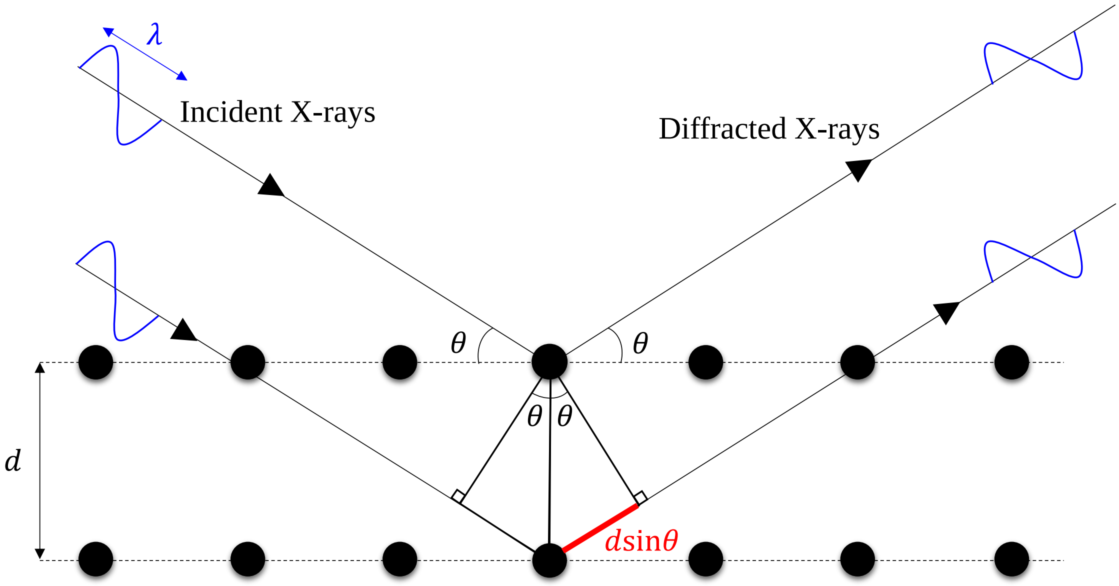

Figure 2-7. Bragg's law [9].

2.2.4. Dry-Process Pycnometer

The density of the glass frits was examined by a dry-process pycnometer (AccuPyc 1330TC, Shimadzu). This technique is non-destructive because of the gas displacement method. Helium gas was used in this thesis. **Figure 2-8** illustrates the measurement principle of the pycnometer. There are two chambers, and pressure is applied upon filling a sample chamber with the gas at first, as shown in **Fig. 2-8(a)**. Next, the gas is discharged into an empty expansion chamber by opening a valve, and the pressure changes in both chambers, as shown in **Fig. 2-8(b)**. With the change of the pressure, the apparent volume of a sample (V_{samp}) is expressed by [10]

$$V_{\mathrm{samp}} = V_{\mathrm{cell}} - \frac{V_{\mathrm{exp}}}{\frac{P_1 - P_{\mathrm{a}}}{P_2 - P_{\mathrm{a}}} - 1}, \tag{2-3}$$

where V_{cell} is the calibrated volume of the sample chamber, V_{exp} is the calibrated volume of the expansion chamber, P_1 is the pressure of the sample chamber after filling it with the gas, P_{a} is the pressure of the expansion chamber before opening the valve, and P_2 is the pressure of the sample and expansion chamber after opening the valve. Finally, the density of the sample is calculated from V_{samp} and weight of the sample.

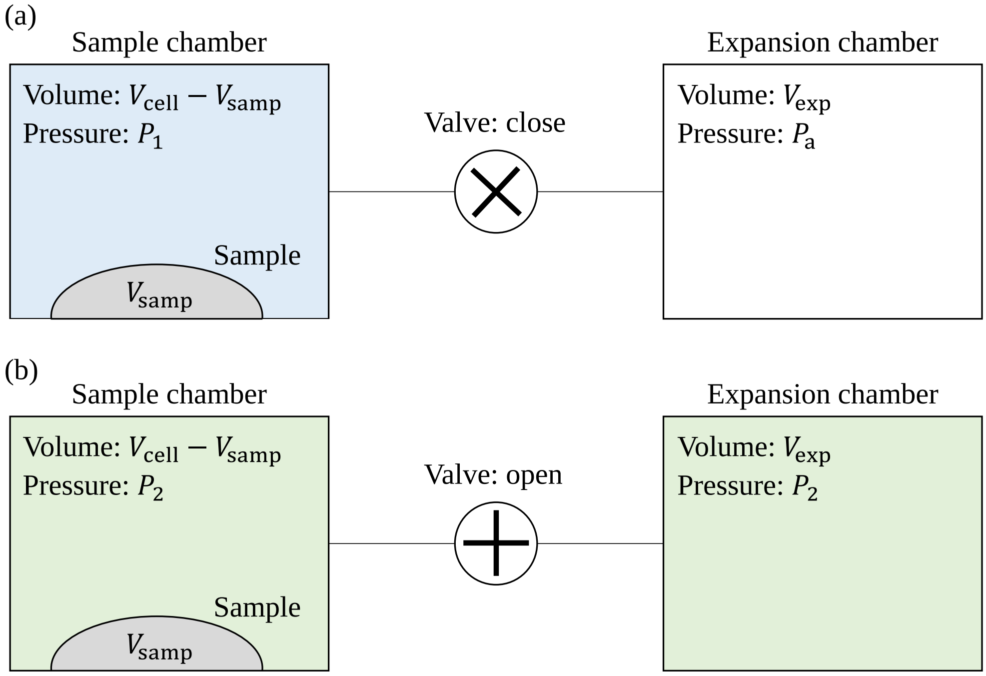

Figure 2-8. Measurement principle diagram of the pycnometer: (a) after filling the sample chamber with the gas and (b) after opening the valve [10].

2.2.5. Ball-up Viscometer

Viscosity of glasses varies over 15 digits so there are various viscosity measurement methods. **Figure 2-9** shows the typical viscosity measurement range of each method. In this thesis, the viscosity of the glass melts was measured using a ball pulling-up viscometer (BVM-11T, OPT), and the guaranteed viscosity measurement range of the viscometer is 2.5–10^4 poise (1 poise = 0.1 Pa·s). It is known that the ball pulling-up measurement applies Stokes' law. When considering of the uniform motion of a ball in liquid with infinite spread, Stokes' law defines viscosity (η) as [11]

$$\eta = \frac{2}{9} g a^2 \frac{(D_{\mathrm{L}} - D_{\mathrm{k}})}{v}, \tag{2-4}$$

where g is a gravitational acceleration, a is a radius of the ball, v is a pulling-up rate of the ball, D_{L} is a density of the melt, and D_{k} is a density of the ball. On the other hand, the viscosity is actually measured in a container, and it is more accurate to add the parameter of the container. For example, the Ladenburg's equation includes the correction of the container, and η is defined as [11,15]

$$\eta = \frac{2}{9} g a^2 \frac{(D_{\mathrm{L}} - D_{\mathrm{k}})}{v} \frac{1}{\left(1 + 2.4\frac{a}{R}\right)\left(1 + 3.3\frac{a}{h}\right)}, \tag{2-5}$$

where R is a radius of the cylindrical container, and h is a depth of the melt in the container. Given that the parameters regarding the container and ball are constant, Eq. 2-5 also can be expressed as [11]

$$\eta = KWT, \tag{2-6}$$

where K is an instrumental constant, W is a pulling-up load, and T is pulling-up time.

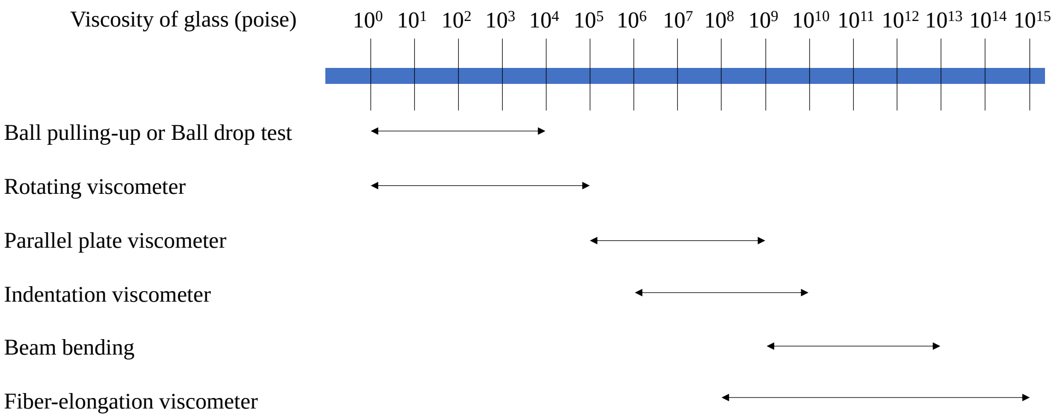

Figure 2-9. Viscosity measurement methods of glasses and the measurement range [11–14].

2.3. Analytical Instruments and Methods for Characterization of Thick Films

2.3.1. Scanning Electron Microscope and Scanning Transmission Electron Microscope

The surface morphology and cross section of the thick films were observed using a scanning electron microscope (SEM) and a scanning transmission electron microscope (STEM). **Figure 2-10** illustrates the optical arrangements of conventional SEM **(a)** and STEM **(b)**. SEM produces images of a sample by scanning the surface with a focused beam of electrons [16]. The position of the beam is combined with the intensity of the detected signals (e.g., reflection electron, secondary electron, characteristic X-ray, and fluorescence), which enables to make an image that contains information about the surface topography and composition of the sample [16]. In this thesis, carbon was sputtered on the samples to prevent the charge-up prior to the SEM observation. STEM produces images of a sample by scanning over a thin sample with a highly focused electron probe, and the transmitted electrons or the diffracted electrons detected with an annular detector form high-resolution images [17]. The STEM generally has two observation modes: 1) bright-field using the intensity of the transmitted wave and 2) dark-field mode using the intensity of the diffraction wave [17]. In the dark field mode, the method using the integral intensity obtained on the annular detector for the transmitted wave is referred to as an annular dark-field (ADF), and the method using the high angle diffracted electrons is referred to as a high-angle annular dark-field (HAADF) [17]. The HADDF provides atomic resolution images of crystalline samples with excellent elemental contrast which is referred to as a Z-contract [17,18]. The Z-contrast is proportionate to approximately atomic number squared [17,18]. In this thesis, a SEM (FlexSEM 1000, Hitachi High-Technologies), another SEM (Merlin, Carl ZEISS Microscopy) equipped with an energy-dispersive X-ray spectroscopy (EDS; X Flash 6130, Bruker), and a STEM (JEM-F200, JEOL) were used in Chapter 4. A SEM (ULTRA55, Carl ZEISS Microscopy) equipped with an EDS (Quantax 400, Bruker) was used in Chapter 5.

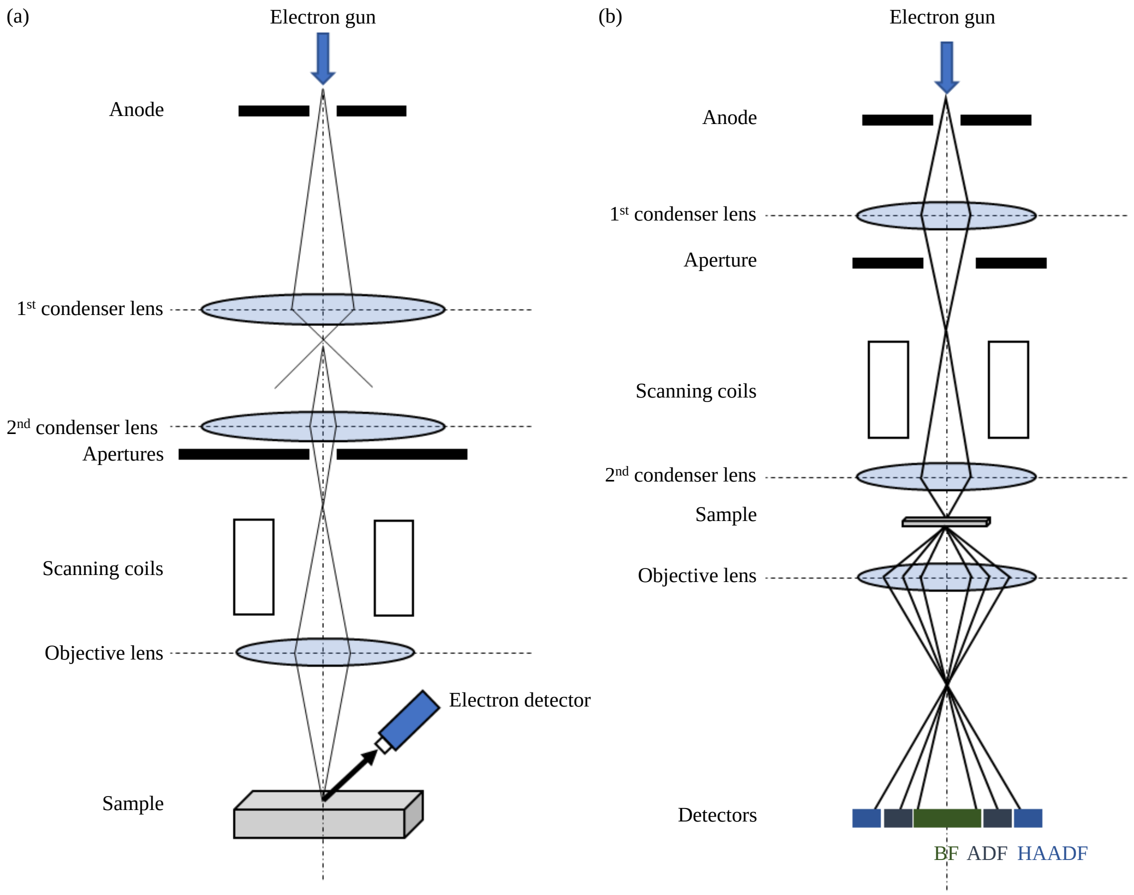

Figure 2-10. Optical arrangements of typical electron microscopes: (a) SEM and (b) STEM [16–20].

2.3.2. Acid Durability Test

In Chapter 4, the acid durability of the glass thick films and Ag thick-film conductors on the Al_2O_3 substrates was examined. The thickness and the calculated average roughness of these samples were measured using a surface texture measuring instrument (Surfcom480A, Tokyo Seimitsu). The samples were immersed in a 1 M H_2SO_4 aq. at 25°C, 60°C, or 80°C for 15 min, 30 min, 45 min, and 60 min at each temperature, and those were repeatedly washed with distilled water and then dried at room temperature overnight. Regarding the glass thick films, the weight and the weight loss of the corroded thick films in acidic solutions were examined using an electric analytical balance (AT200, Mettler-Toledo International). In addition, the surface of the glass thick films was observed using the SEM. With regard to the Ag thick-film conductors, in addition to the cross-sectional SEM observation, the peel adhesion on the Al_2O_3 substrates after immersion in a 1 M H_2SO_4 aq. was characterized. After polishing the surface of the Ag thick-film conductors, Sn-covered coppers wire were attached to 2 mm × 2mm pads by dipping for 10 s in a solder (Sn 96.5 wt.%, Ag 3.0 wt.%, and Cu 0.5 wt.%) at 260°C using a flux (Alpha 611, Alpha Assembly Solutions). The wires were pulled using a pull tester (1605NHTP, Aiko Engineering) with a 90° peel configuration, as illustrated in **Fig. 2-11**. The remaining Ag thick-film conductors on the Al_2O_3 substrates after the peel adhesion test were photographically observed with a microscope (BX51, Olympus).

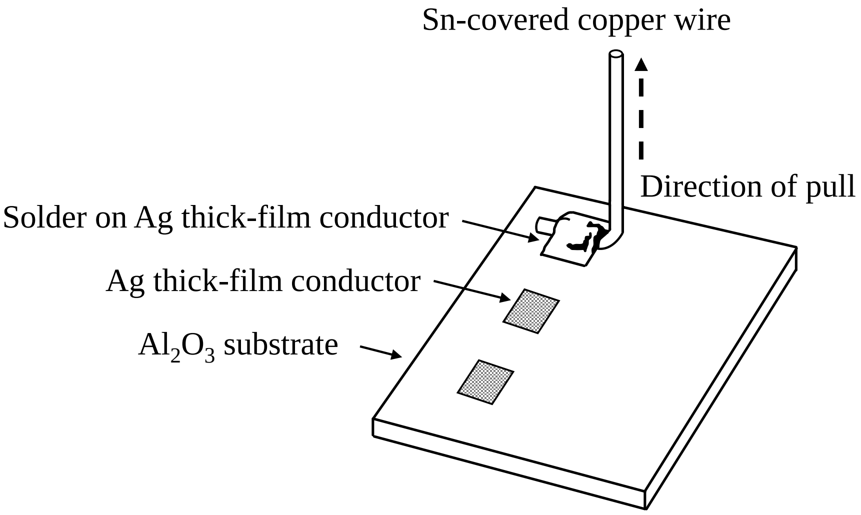

Figure 2-11. Schematic depiction of the Ag thick-film conductor on the Al_2O_3 substrate used for the peel adhesion test.

2.3.3. Contact Resistivity Measurement

In Chapter 5, the thickness and the calculated average roughness of the Ag thick-film conductors on the Si wafers were measured using a surface texture measuring instrument (Surfcom480A, Tokyo Seimitsu). Next, the conventional transfer length method (TLM) was applied to determine the contact resistivity of the Ag thick-film conductors on the Si wafers [21–25]. As illustrated in **Fig. 2-12,** the Ag thick-film conductors were printed with 1 mm length (d) and 10 mm width (W) separated by a distance (L) 1 mm, 2 mm, 3 mm, 4 mm, and 5 mm, respectively. The total resistance between the two Ag thick-film conductors was measured using a SourceMeter (Keithley 2400, Keithley Instruments). The results on total resistance versus Ag thick-film conductor distance measured by TLM are often used to estimate the contact resistivity as contact performance of Ag thick-film conductors on Si wafers [21–23].

The total resistance (R_T) is the sum of (i) the sheet resistance (R_{SH}) of the emitter between the two Ag thick-film conductors with a distance (L) and width (W), and (ii) the contact resistance of the two Ag thick-film conductors on the Si wafer $(2R_c)$, as expressed by [23,24]

$$R_T = \frac{R_{SH}}{W} L + 2R_C. \tag{2-7}$$

As shown in **Fig. 2-13**, the contact resistance (R_c) is one half of the y-intercept according to Eq. 2-7. **Figure 2-14** shows the schematic circuit diagram of the cross-section of two Ag thick-film conductors connected by the probes on the Si wafer during the total resistance measurement by TLM. It is noted that TLM assumes that each contact area is at a constant potential, and current flows uniformly between one contact area and the next [22]. Electrical current from the Ag thick-film conductor to the Si wafer is thought to flow near the edge of the contact area more than in the middle of the contact area due to the current crowding effect, as shown in **Fig. 2-14** [22,26]. The length over which current is thought to flow is referred to as a transfer length (L_T), and that is expressed by [23,24]

$$L_T = \frac{R_C W}{R_{SH}}. \tag{2-8}$$

L_T is one half of the x-intercept in **Fig. 2-13**. The contact resistivity (ρ_c) with a unit of $\Omega\cdot\mathrm{cm}^2$ is expressed by [21,23]

$$\rho_c = R_c L_T W. \tag{2-9}$$

In this thesis, the slope of TLM calculated R_T plotted as a function of L in **Fig. 2-13** is drawn from a calculation using the least-squares method [27]. The least squares method is a statistical procedure to find the best fit for a set of data points by minimizing the sum of the residuals of points [27]. Given data $\{(x_1, y_1), \ldots, (x_N, y_N)\}$, the error associated to $y = ax + b$ is defined as

$$E(a, b) = \sum_{n=1}^{N} \left(y_n - (ax_n + b)\right)^2, \tag{2-10}$$

$$\frac{\partial E}{\partial a} = \sum_{n=1}^{N} 2\left(y_n - (ax_n + b)\right) \cdot (-x_n), \tag{2-11}$$

$$\frac{\partial E}{\partial b} = \sum_{n=1}^{N} 2\left(y_n - (ax_n + b)\right) \cdot 1. \tag{2-12}$$

The values of a and b that minimize the error are $\frac{\partial E}{\partial a} = 0$ and $\frac{\partial E}{\partial b} = 0$, and those are obtained by solving the binary linear equation:

$$\begin{pmatrix} a \\ b \end{pmatrix} = \begin{pmatrix} \sum_{n=1}^{N} x_n^2 & \sum_{n=1}^{N} x_n \\ \sum_{n=1}^{N} x_n & \sum_{n=1}^{N} 1 \end{pmatrix}^{-1} \begin{pmatrix} \sum_{n=1}^{N} x_n y_n \\ \sum_{n=1}^{N} y_n \end{pmatrix} \tag{2-13}$$

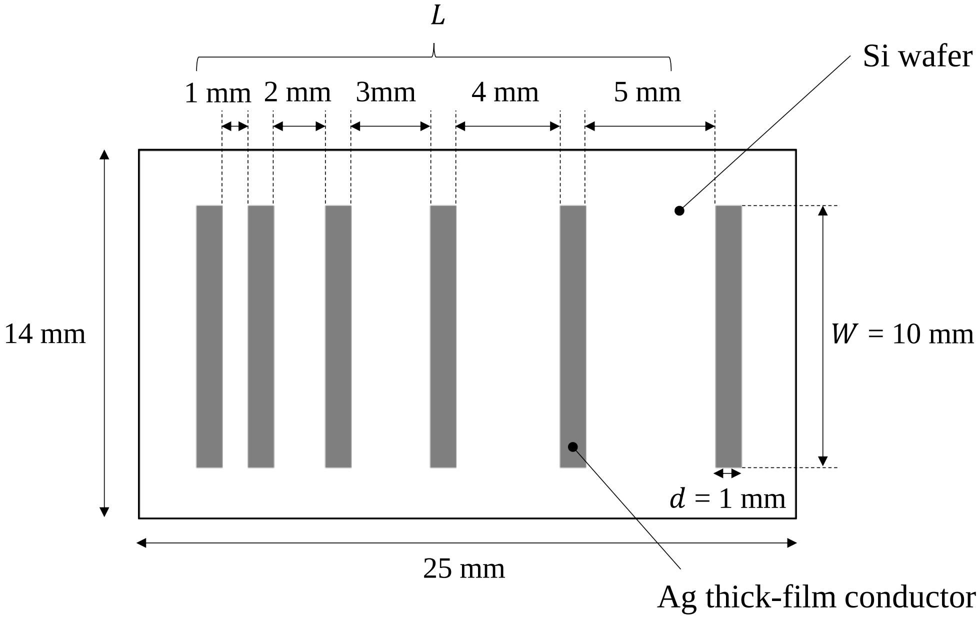

Figure 2-12. Schematic plan-view depiction of the Ag thick-film conductor pattern used for measurement of contact resistivity by TLM.

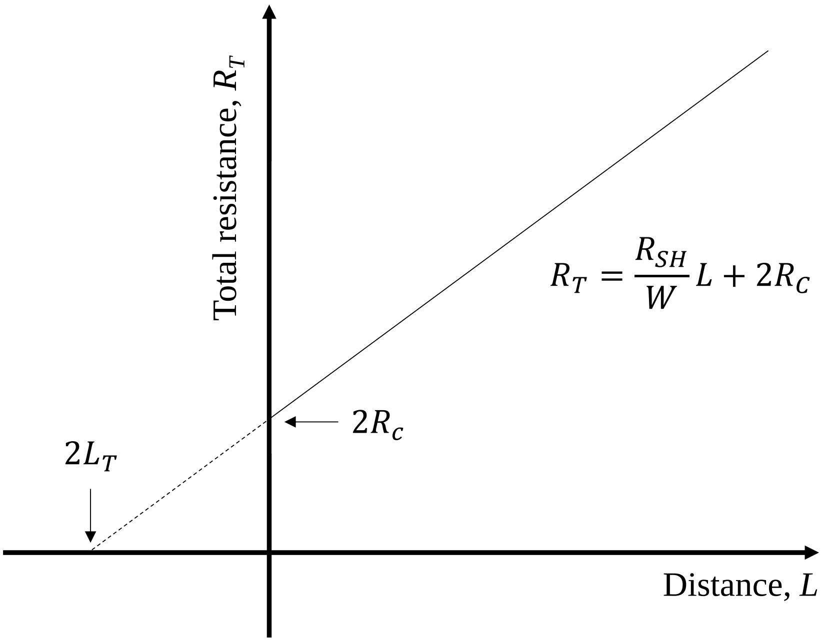

Figure 2-13. Relationship of the Ag thick-film conductor distance and total resistance [21].

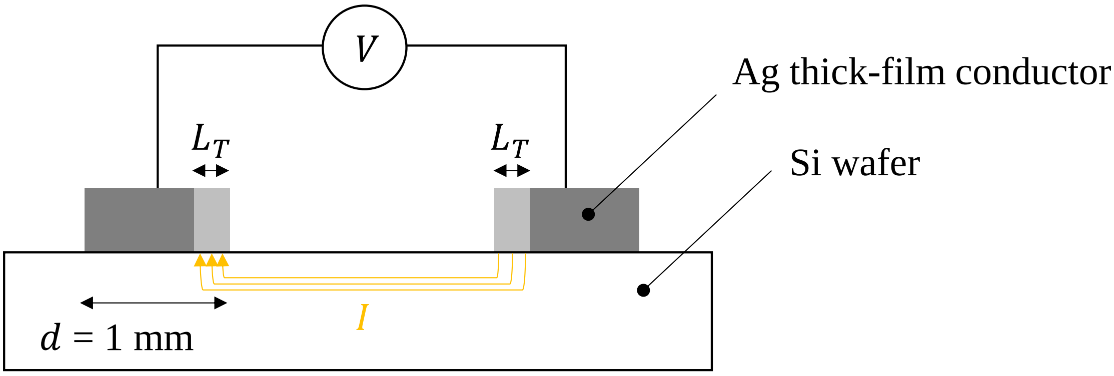

Figure 2-14. Schematic circuit diagram of the cross-section of two Ag thick-film conductors connected by the probes on the Si wafer during the total resistance measurement by TLM [26].

2.3.4. Solder Leach Resistance Test

In Chapter 5, the solder leach resistance of the Ag thick-film conductors was examined. The interdiffusion of Ag and solder and the formation of intermetallics can occur during the soldering process, as discussed in Subsection 1.2.4. Due to this, the solder leach increases the resistance of Ag thick-film conductors during the soldering process, and that finally leads to the disconnection. [28,29]. The Ag thick-film conductors on the Si wafers were dipped in a solder (Sn 62.0 wt.%, Pb 36.0 wt.%, and Ag 2.0 wt.%) at 200°C, 220°C, and 240°C using a flux (Alpha 611, Alpha Assembly Solutions), and the resistance-change was examined up to 60 s using a SourceMeter (Keithley 2400, Keithley Instruments). The resistance change ratio (ΔR) is expressed by

$$\Delta R = \frac{R_t}{R_i}, \tag{2-14}$$

where R_i is the initial resistance, and R_t is the resistance at the dipping time (t).

References

[1] T. Tsugoshi, *Analysis*, **12**, pp.568–574 (2017).

[2] N. Murasawa, H. Koseki, Y. Iwata, and Y. Shibata, *Journal of Food Research*, **1**(1), pp.320–329 (2012).

[3] M. Yamane, *Hajimete Garasu wo Tsukuruhito no Tameni* (*Handbook of Glasses*), Uchida Rokakuho Publishing, Japan, pp.147–151 (2005) [in Japanese].

[4] Y. Ogura, *Horiba Readout*, (20), pp.39–43 (2000).

[5] Y. Togawa and T. Kurozumi, *Horiba Readout*, (19), pp.1–5 (1999).

[6] T. Iwai, Y. Aizu, and T. Asakura, *Laser Study*, **27**(9), pp.642–651 (1999).

[7] S. A. Speakman, *Introduction to X-Ray Powder Diffraction Data Analysis*, Massachusetts Institute of Technology, USA (2013).

[8] K. Ohara, *New Glass*, **31**(118), pp.24–26 (2016).

[9] M. Kato, *X-Ray Diffraction Analysis*, Uchida Rokakuho Publishing, Japan, pp.17–22 (1990).

[10] *AccuPyc 1330TC manual*, Shimadzu, Appendix A pp.1–3.

[11] I. Sawai, M. Kunugi, and T. Yamate, *J. Soc. Mater. Sci., Jpn.*, **8**(70), pp.615–618 (1959).

[12] M. Kunugi, R. Ota, and T. Yamate, *J. Soc. Mater. Sci., Jpn.*, **15**(155), pp.567–571 (1966).

[13] Y. Shiraishi, *Bulletin of the Research Institute of Mineral Dressing and Metallurgy, Tohoku University*, **38**(1), pp.1–10 (1982).

[14] R. Ota, F. Tsuchiya, K. Kawamura, S. Nakanishi, and J. Fukunaga, *J. Ceram. Assoc. Japan*, **99**(2), pp.168–172 (1991).

[15] F. Imoto and K. Hirao, *J. Ceram. Assoc. Japan*, **67**(11), pp.381–385 (1959).

[16] T. Umemura *et al.*, *Instrumental Analysis*, Ed. by H. Ohtani, Kodansha, Japan, pp.136–148 (2015).

[17] K. Saitoh, *Journal of the Crystallographic Society of Japan*, **47**(1), pp.9–14 (2005).

[18] A. Ponce, S. Mejia-Rosales, and M. Jose-Yacaman, *Nanoparticles in Biology and Medicine: Methods and Protocols, Methods in Molecular Biology*, Ed. by M. Soloviev, Springer Science+Business Media, Germany, pp.453–471 (2012).

[19] J. C. Meyer, *Graphene*, Eds. by V. Skakalova and A. B. Kaier, Woodhead Publishing, UK, pp.101–123 (2014).

[20] B. J. Inkson, *Materials Characterization Using Nondestructive Evaluation (NDE) Methods*, Eds. by G. Hubschen *et al.*, Woodhead Publishing, UK, pp.17–43 (2016).

[21] Y. Shih, Y. Lin, J. You, and F. G. Shi, *J. Electron. Mater.*, **42**(3), pp.410–416 (2013).

[22] A. M. Gabor, G. Gregory, A. M. Payne, R. Janoch, A. Anselmo, V. Yelundur, and K. O. Davis, presented at *the 43rd IEEE Photovoltaic Specialists Conf.*, pp.1–4 (2016).

[23] R. Janoch, A. M. Gabor, A. Anselmo, and C. E. Dube, presented at *the 42nd IEEE Photovoltaic Specialists Conf.*, pp.1–6 (2015).

[24] G. K. Reeves and H. B. Harrison, *IEEE Electron Device Lett.*, **3**(5), pp.111–113 (1982).

[25] H. H. Berger, *J. Electrochem. Soc.*, **119**(4), pp.507–514 (1972).

[26] R. Hoenig, *Dr. Thesis*, Faculty of Engineering, Albert-Ludwigs-Universität Freiburg, Germany (2014).

[27] S. J. Miller, *The Method of Least Squares*, Brown University, USA, pp.1–7 (2006).

[28] N. Sugimoto, *HIC Peisuto Zairyo to Insatsu-Shosei Gijutsu* (*HIC Paste Materials and Print-Firing Technology*), Japan Association for International Chemical Information, Japan, pp.27–55 (1989) [in Japanese].

[29] S. Achmatowicz1 and E. Zwierkowska, *MATERIA"Y ELEKTRONICZNE*, **34**, pp.5–47 (2006).

Chapter 3

Glass Frit Preparation for Ag Thick-Film Conductors and Characterization

3.1. Preparation of Glass Frits for Ag Thick-Film Conductors

3.1.1. Preparation of Alkali and Alkaline-Earth Borosilicate (AEB) Glass Frit for Chapter 4

Table 3-1 shows the composition (wt.%) of the AEB glass frit. SiO_2, H_3BO_3, Na_2CO_3, $Al(OH)_3$, $BaCO_3$, $SrCO_3$, ZnO, TiO_2, $Mg(OH)_2$, and SnO_2 were used as starting materials of the AEB glass, and all of the materials have a purity of 95% or more. Here a small amount of MgO in the glass is expected to improve water resistance and mechanical properties of the obtained AEB glass frit; the role of this addition differs from that of the addition of the MgO powder to the AEB glass paste, which will be described in Chapter 4 [1–3]. A batch was weighed, mixed, and melted in a platinum crucible in an electrical furnace at 1300°C for approximately 1.5 h to produce clear and homogeneous liquid. After the melted glass was evenly distributed, that was immediately poured onto the roller quencher and then ball-milled in isopropanol to produce the AEB glass frit. The particle size, density, thermal behavior, and crystal structure were examined for the AEB glass frit.

Table 3-1. Composition of the AEB glass frit (wt.%)

Glass frit name	SiO_2	B_2O_3	Na_2O	Al_2O_3	BaO	SrO	ZnO	TiO_2	MgO	SnO_2
AEB	20.5	20.0	3.0	3.0	19.0	12.5	10.5	6.5	3.0	2.0

3.1.2. Preparation of Lead Borosilicate (PS) and Lead Tellurite (PT) Glass Frit for Chapter 5

Table 3-2 shows the composition (wt.%) of the PS and PT glass frit. Pb_3O_4, SiO_2, B_2O_3, Li_2CO_3, Na_2CO_3, Al_2O_3, ZrO_2, and TeO_2 were used as starting materials of these glass frits, and all of them have a purity of 98% or more. Each batch was weighed, mixed, and melted in a platinum crucible in an electrical furnace to produce clear and homogeneous liquid. The PS glass was melted at 1200°C for approximately 1 h, whereas the PT glass was melted at 1000°C for approximately 1 h. After the melted glass was evenly distributed, that was immediately poured onto the roller quencher and then ball-milled in isopropanol to produce the glass frit. The particle size, density, thermal behavior, crystal structure, and melt viscosity were examined for the PS and PT glass frit.

Table 3-2. Composition of the PS and PT glass frit (wt.%)

Glass frit name	PbO	SiO_2	B_2O_3	Li_2O	Na_2O	Al_2O_3	ZrO_2	TeO_2
PS	79.5	17.8	1.9	0.1	0.1	0.2	0.4	-
PT	48.0	-	-	0.5	-	-	-	51.5

3.2. Characterization of the Prepared Glass Frits

3.2.1. Characterization of the AEB Glass Frit

The white AEB glass frit was obtained, and the average particle size was approximately 2.5 μm, as show in **Fig. 3-1**. The density of the AEB glass frit was 3.4 g/cm^3. The glass transition temperature (T_g) of the AEB glass frit was approximately 570°C, and the clear crystal peak (T_c) was not observed by 850°C at a heating rate of 40°C/min, as shown in **Fig. 3-2**. The AEB glass frit did not exhibit a crystalline diffraction peak in the XRD pattern, and a halo peak was observed, as shown in **Fig. 3-3**. Since the atomic arrangement of glass is not regular, the halo peak is the distinct peak of glass.

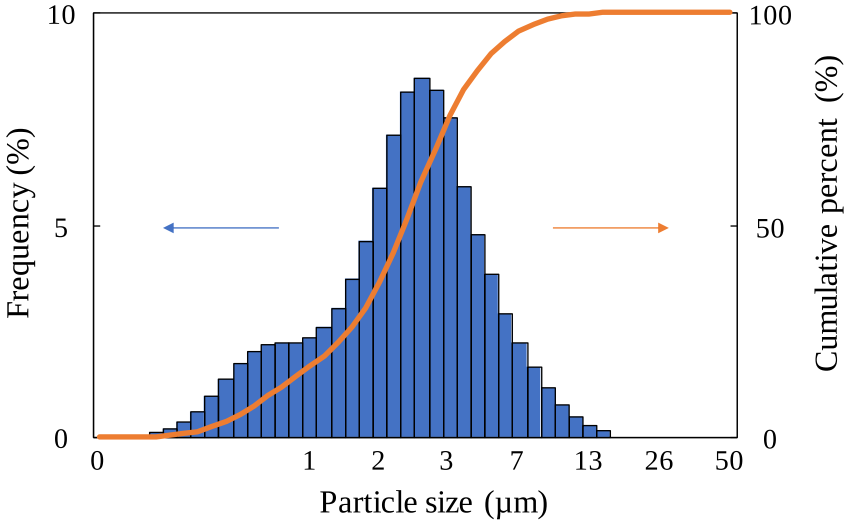

Figure 3-1. Particle size distribution of the AEB glass frit.

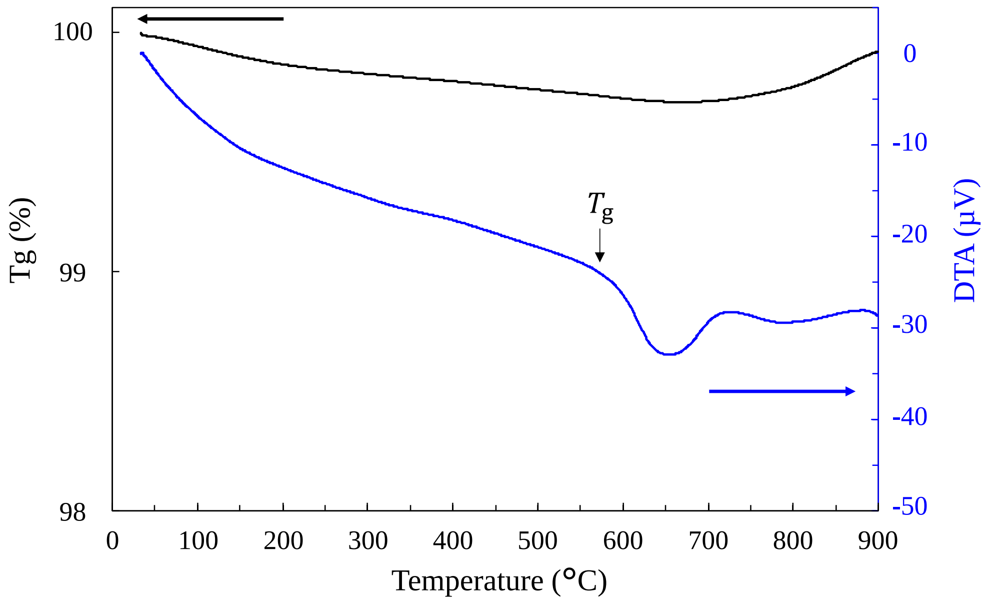

Figure 3-2. TG/DTA pattern of the AEB glass frit heated in air.

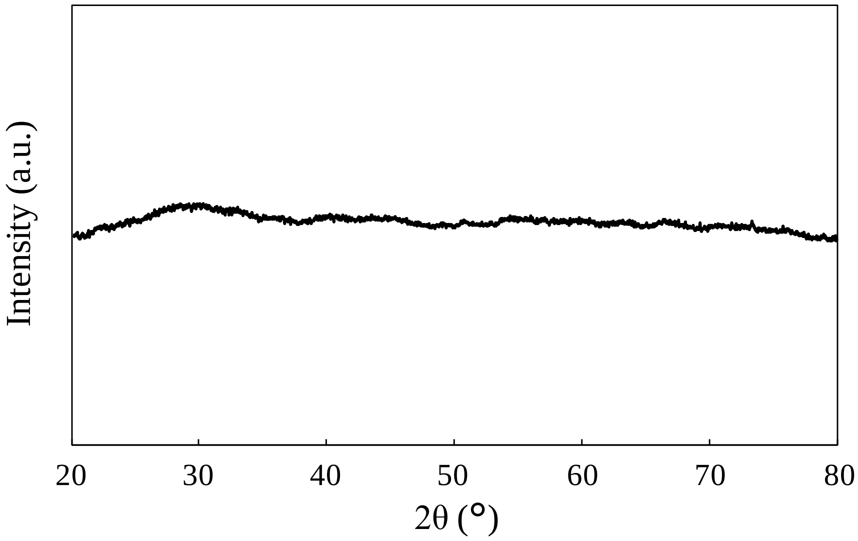

Figure 3-3. XRD pattern of the AEB glass frit.

3.2.2. Characterization of the PS and PT Glass Frit

The PS and PT glass frit were white, and the average particle size was approximately 0.8 μm, as shown in **Figs. 3-4(a)** and **3-4(b)**. The density of the PS glass frit was 6.2 g/cm^3, whereas that of the PT glass frit was 6.8 g/cm^3. **Figure 3-5** shows thermal behavior of the PS and PT glass frit at a heating rate of 20°C/min in air. The glass transition temperature (T_g) of the PS glass frit was approximately 390°C, and the peaks for crystallization (T_c) and re-melting (T_m) were not observed up to 800°C, as shown in **Fig. 3-5(a)**. T_g of the PT glass frit was approximately 230°C, and T_c and T_m were approximately 370°C and 570°C, respectively, as shown in **Fig. 3-5(b)**. Both glass frits did not exhibit a crystalline diffraction peak in the XRD patterns, and a halo peak was observed, as shown in **Figs. 3-6(a)** and **3-6(b)**. Since the atomic arrangement of glass is not regular, the halo peak is the distinct peak of glass. Therefore, the PT glass frit was the crystallized glass.

The most popular viscosity model of glass is Vogel-Fulcher-Tammann (VFT) equation. It is known that the equation fits to the experiment data in a wide viscosity range from T_g to liquidus temperature in most glass compositions, and viscosity (η) is defined as [4,5]

$$\eta = A\exp\{B/(T - T_0)\}, \tag{3-1}$$

$$\log\eta = A + \{B/(T - T_0)\}, \tag{3-2}$$

where A, B, and T_0 are constants, and T is temperature. T_0 is generally lower than T_g, and the viscosity is infinite at the temperature. Given that the viscosity of the PS and PT glass follows Eq. 3-2, the viscosity curve is fitted, as shown in **Fig. 3-7**. The substantial fill marks are the measurement values. The solid lines are the fitted curves in the measurement range, and the dashed lines with no-fill markers are the fitted curves extended to T_g from the measurement range. **Table 3-3** shows the obtained constants by the fitting. The viscosity of the PS glass melt was approximately 53 Pa·s at 650°C and 5 Pa·s at 750°C, whereas that of the PT glass melt was less than 1 Pa·s at 650°C or higher.

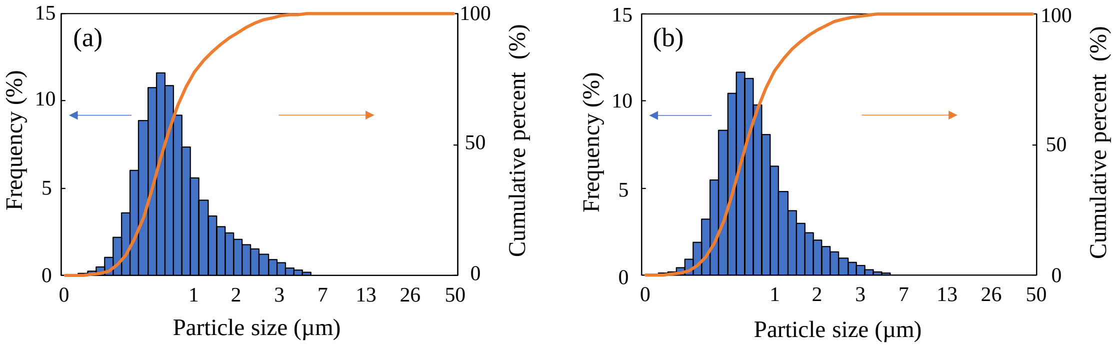

Figure 3-4. Particle size distributions of the glass frits: (a) PS and (b) PT.

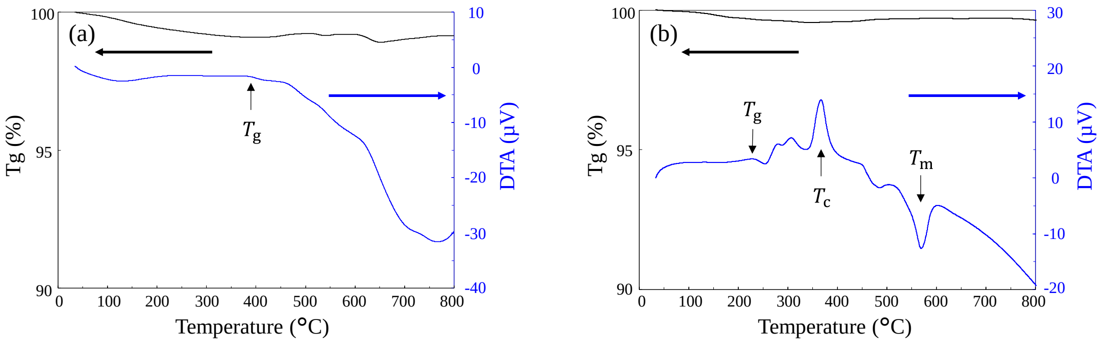

Figure 3-5. TG/DTA patterns of the glass frits heated in air: (a) PS and (b) PT.

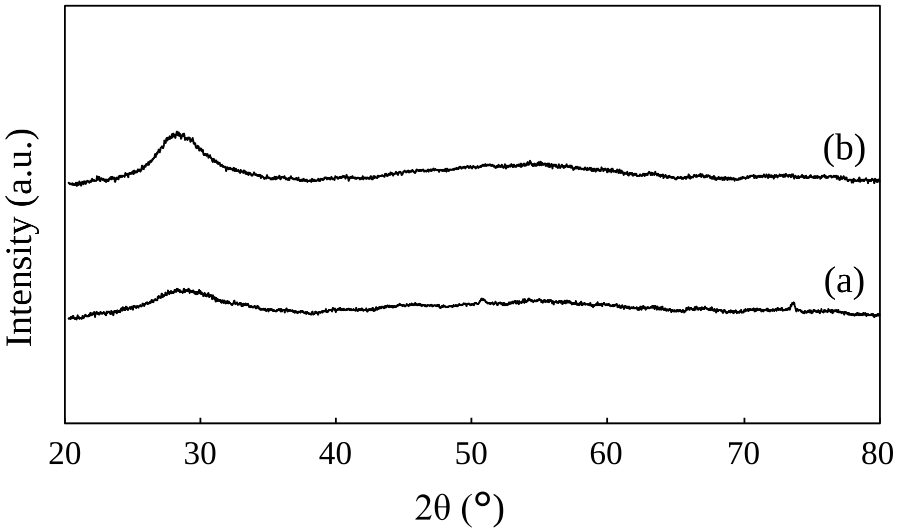

Figure 3-6. XRD patterns of the glass frits: (a) PS and (b) PT.

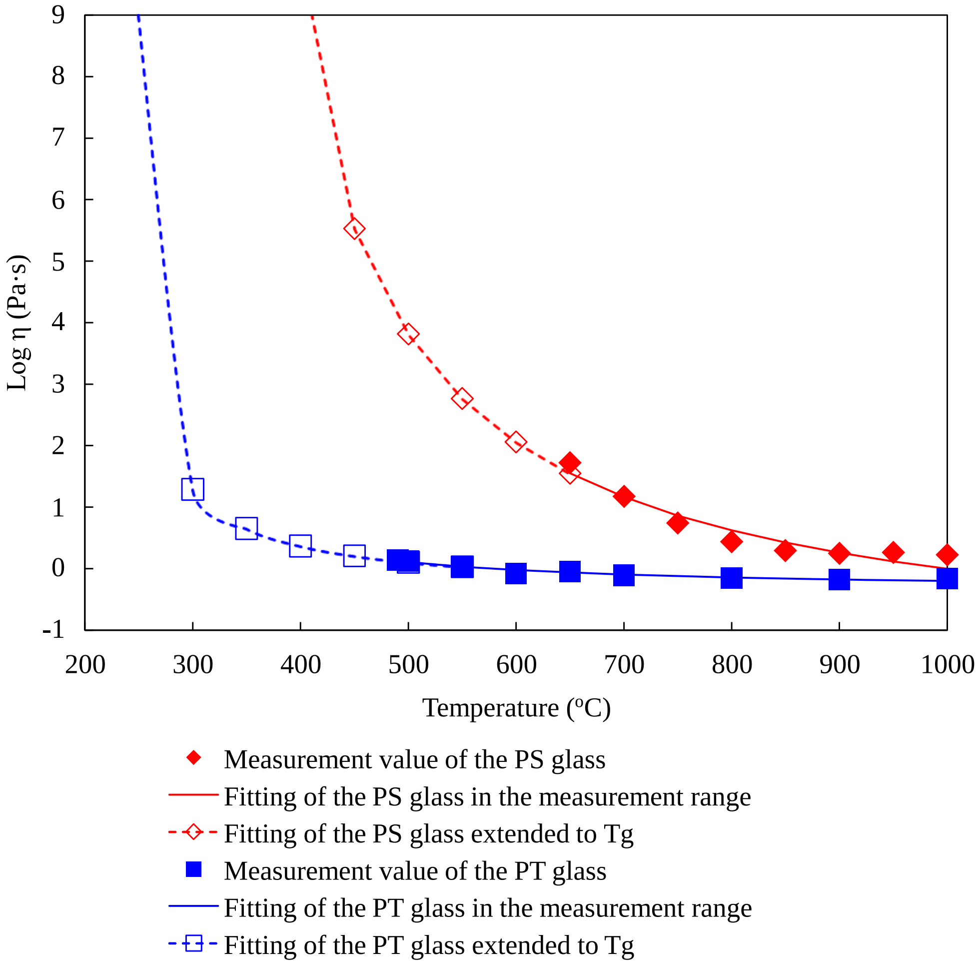

Figure 3-7. Viscosity curves of the PS and PT glass as a function of temperature.

Table 3-3. Constants calculated from the VTF fitting

Glass name	*A*	*B*	T_0 (°C)
PS	-0.59	1123	292
PT	0.63	134	220

References

[1] R. Terai, *Mater. Integr.*, **17**(2), pp.55–61 (2004).

[2] M. Tanaka, T. Uwabe, Y. Ito, D. Kojima, and J. Ono, *Bulletin of TIRI*, (1), pp.50–53 (2006).

[3] G. H. Koenderink, R. H. Brzesowsky, and A. R. Balkenende, *J. Non-Cryst. Solids*, **262**, pp.80–98 (2000).

[4] H. Tokunaga, S. Haruki, S. Sukenaga, N. Saito, and K. Nakashima, *J. Jpn. Inst. Met.*, **74**(5), pp.331–336 (2010).

[5] J. C. Mauro, Y. Yue, A. J. Ellison, P. K. Gupta, and D. C. Allan, *PNAS*, **106**(47), pp.19780–19784 (2009).

Chapter 4

Effect of Micro-Crystallization of Alkali and Alkaline-Earth Borosilicate (AEB) Glass on Acid Durability of Ag Thick-Film Conductor

4.1. Introduction

Glass frits in conductor pastes promote the sintering of metal powders during the firing process and binding of the metal film to the substrate [1–3]. Therefore, low-melting glasses are suitable for thick-film conductors, and lead borosilicate glasses have been extensively used [1,4,5]. Lead lowers the melting temperature of glasses and facilitates melting of various metal oxides into glasses in a wide glass formation range [6]. Consequently, lead borosilicate glasses are useful for designing thick-film conductors with low resistivity and strong adhesion on ceramic substrates with high reliability. However, environmental regulations, such as the Waste Electrical and Electronic Equipment Directive and Restriction of Hazardous Substances Directive from 2003, banned the use of lead for many applications, the scope of which is continuously expanding.

It is known that Bi_2O_3-based glasses, phosphate glasses, and borosilicate glasses containing B_2O_3 and/or alkali a lot are available as Pb-free low-melting glasses [7–9]. In addition, ZnO, SnO, and/or fluorides decrease the melting temperature of glasses [7]. Despite these advances, high chemical durability is a challenging for most low-melting Pb-free glasses. There are many studies on corrosion mechanisms of borosilicate glasses. Leaching occurs due to the replacement of network-modifying constituent ions (e.g., alkali) with H^+ (H_3O^+) from the solution, and solutions containing these protonated species enhance such reaction [10–12]. Glass network dissolution occurs due to the nucleophilic attack of OH^- on the silicate network under alkali conditions [10–12]. On the other hand, the excellent chemical durability of crystallized glasses has received considerable attention. For examples, it is reported that the acid durability of crystallized Li_2O–SiO_2 glasses ($Li_2O{\cdot}3SiO_2$, $Li_2O{\cdot}2SiO_2$, $Li_2O{\cdot}1.5SiO_2$) by the addition of Pt was much high compared with that of the glasses without the addition of Pt [13]. There are many reports of promoters for crystallized glasses, and the effect changes by the base glass composition. P_2O_5 promotes the crystallization of high lithia and low alumina silicate glasses, whereas it does not work for low lithia and high alumina silicate glasses since P_2O_5 bonds to Al_2O_3, and it is incorporated into the tetrahedral silicate network [14]. In case of the latter glass composition, TiO_2 and/or ZrO_2 are effective for the crystallization [14]. The effect of Na_2O on the crystallization is low in comparison to Li_2O, so MgO, TiO_2, and/or ZrO_2 are effective to promote the crystallization for alkali silicate glasses including Na_2O [14]. The acid durability of crystallized glasses is generally affected by the acid durability of precipitated crystals, glass matrix around the precipitated crystals, structure (e.g., presence or absence of micro cracks), and surface morphology [13,14].

Although the microstructure analysis of thick-film conductors glass-bonded onto Al_2O_3 substrates and the effect of the firing conditions and Al_2O_3 substrate characteristics (e.g., composition and surface texture) on adhesion behavior have been investigated, there are few studies on the chemical durability of thick-film conductors under acidic conditions [1–4,15,16]. Better understanding of the acid corrosion behavior of glass in thick films would facilitate the designing of thick-film conductors with enhanced properties. For example, in most industrial processes, Ni and Sn are typically electroplated on thick-film conductors used as the electrode termination of surface-mount chip components, and the thick-film conductors are soaked in acidic solutions during the electroplating process in many cases [17–20]. In such process, acid durability is essential for thick-film conductors.

The purpose of Chapter 4 is to investigate the effect of micro-crystallization of the alkali and alkaline-earth borosilicate (AEB) glass on the acid durability of Ag thick-film conductors. At first, the micro-crystallization of the AEB glass and the acid durability are examined by the addition of MgO powder to the glass thick films on Al_2O_3 substrates at 850°C. Next, the micro-crystallization of the glass and the acid durability are studied in the Ag thick-film conductors. According to the abovementioned results, the correlation between the micro-crystallization of the glass and the acid durability of the Ag thick-film conductors is evaluated. Furthermore, the bulk resistivity for the Ag thick-film conductors is examined.

4.2. Experimental Procedures

As shown in **Table 4-1**, three types of glass pastes and two types of Ag conductor pastes were prepared by mixing different ratios of the AEB glass frit, MgO powder (average particle size of 2 μm), and Ag powder (average particle size of 2 μm) with an organic vehicle using a roll-milling machine. The amount of MgO powder in the GTF-1.5 glass paste was one half of the GTF-2 glass paste. The ratio of the MgO powder to AEB glass frit in the GTF-2 glass paste was the same as that in the ATF-2 Ag conductor paste. Generally, thick-film conductors contain metal powders 40–80 wt.% and glass frits 3–14 wt.% [21]. Since glass frits are insulation binder, adhesion of thick-film conductors on substrates decreases at low glass frit content, while bulk resistivity increases at high glass frit content. The amount of Ag powder and glass frit is decided by considering these properties. The organic vehicle was composed of ethyl cellulose, terpineol, and diethylene glycol dibutyl ether. The thick films were prepared by screen printing the pastes onto the dense sintered Al_2O_3 substrates (A476T, Kyocera). After the screen-printing process, the samples were dried at 150°C for 10 min to remove the volatile organic solvent. Next, the samples were heated to 850°C at the average rate of 75°C/min in air and fired at the temperature for 10 min.

The crystal structure, acid durability, and microstructure of the glass thick films were examined. Next, the microstructure, acid durability, and bulk resistivity of the Ag thick-film conductors were evaluated.

Table 4-1. Composition of the glass and Ag conductor pastes (wt.%)

Category	Sample name	AEB glass frit	MgO powder	Ag powder	Organic vehicle
Glass pastes	GTF-1	70.0	-	-	30.0
	GTF-1.5	67.5	2.5	-	30.0
	GTF-2	65.0	5.0	-	30.0
Ag conductor pastes	ATF-1	7.0	-	60.0	33.0
	ATF-2	6.5	0.5	60.0	33.0

4.3. Results and Discussion

4.3.1. Effect of the MgO Powder Addition to the Glass Pastes on the Structure of Glass During the Annealing Process

Figure 4-1 shows the XRD patterns of the GTF-1 **(a)**, GTF-1.5 **(b)**, and GTF-2 glass thick film **(c)** on the Al_2O_3 substrates after annealing at 150°C and 850°C. As shown in **Fig. 4-1(a)**, the XRD patterns of the GTF-1 glass thick film did not exhibit a crystalline diffraction peak except for the peaks attributed to the Al_2O_3 substrate corresponding to α-Al_2O_3 (PDF card No. 71-1123). This indicates the amorphous state of the AEB glass annealed at the temperature as high as 850°C. On the other hand, the peak assigned to MgO (200) plane at about 43° (PDF card No. 4-0829) was observed in the XRD patterns of the GTF-1.5 and GTF-2 glass thick film dried at 150°C, as shown in the bottom patterns in **Figs. 4-1(b)** and **4-1(c)**. This observation indicates the absence of reaction between the added MgO powder and AEB glass frit at 150°C. After firing at 850°C, the peak attributed to the MgO disappeared, and the peaks attributed to $(Ba,Sr)Al_2Si_2O_8$ (BSAS) were observed, as shown in the upper patterns in **Figs. 4-1(b)** and **4-1(c)**. Although the diffraction peaks of the GTF-1.5 and GTF-2 glass thick film were close to those of $Ba_{0.75}Sr_{0.25}Al_2Si_2O_8$ (PDF card No. 38-1451), additional experiments are needed to determine the accurate ratio of Ba to Sr in the obtained BSAS. It is known that $BaAl_2Si_2O_8$ (BAS) and $SrAl_2Si_2O_8$ (SAS) form solid solutions in the entire composition range, and the polymorphism exists [22]. The crystallinity of the GTF-1.5 was 53%, whereas that of the GTF-2 was 63%. These results suggest that the micro-crystallization of the AEB glass was promoted by the reaction of the added MgO powder with the AEB glass frit. MgO is not crystal core and it is thought that MgO increases non-bridging oxygen atoms in the AEB glass and makes it easier to re-arrange the structure for crystallization.

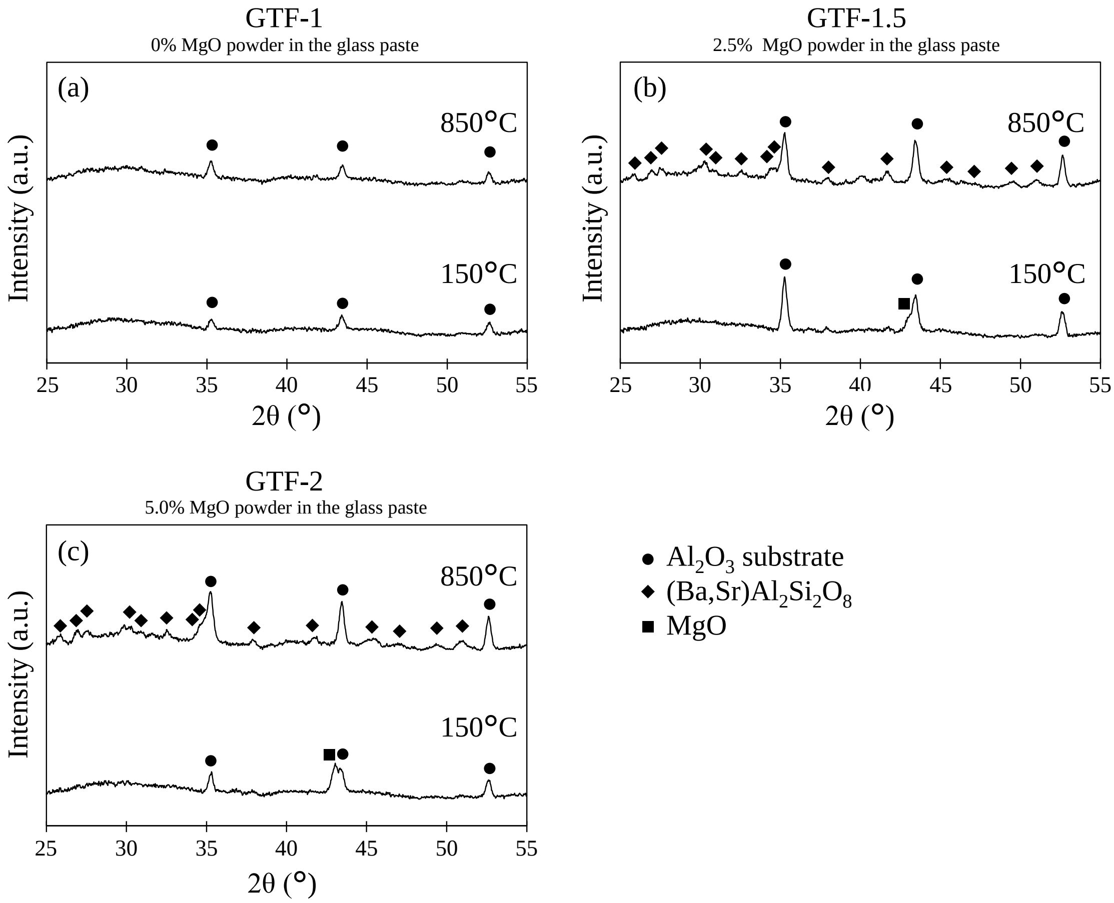

Figure 4-1. XRD patterns of the glass thick films on the Al_2O_3 substrates annealed at 150°C and 850°C: (a) GTF-1, (b) GTF-1.5, and (c) GTF-2.

4.3.2. Acid Durability of the Glass Thick Films

Figure 4-2 shows the corrosion weight loss of the GTF-1 **(a)**, GTF-1.5 **(b)**, and GTF-2 glass thick film **(c)** as a function of immersion time in a H_2SO_4 aq. The weight of the glass thick film was approximately 26 mg before the corrosion test, and the area was approximately 4.84 cm^2. The average thickness was approximately 16 μm, and the calculated average roughness was approximately 0.8 μm before the corrosion test. The weight loss of the GTF-1 glass thick film without the addition of MgO powder increased monotonously with increasing immersion time up to 60 min at all temperatures. The weight loss of the GTF-2 glass thick film with the added MgO powder increased by approximate 15 min of immersion at all temperatures, and then the weight loss remained approximately constant after 45 min of immersion at 25°C and after 30 min of immersion at 60°C and 80°C, respectively. The weight loss of the GTF-1.5 glass thick film was less than that of the GTF-1 glass thick film and higher than that of the GTF-2 glass thick film. The weight loss rate of the GTF-1, GTF-1.5, and GTF-2 glass thick film was accelerated at high temperature. It is known that elution of alkali and B_2O_3 in glass is accelerated at high temperature [23]. It is noted that the weight losses of the GTF-1.5 and GTF-2 glass thick film were approximately 46% and 56% lower in comparison to that of the GTF-1 glass thick film for the 60-min immersion at 25°C, respectively. This observation indicates an improvement in the acid durability of the glass thick film owing to the addition of the MgO powder to the glass paste.

Figure 4-3 presents the SEM images of the GTF-1 **[(a)–(c)]**, GTF-1.5 **[(d)–(f)]**, and GTF-2 glass thick film **[(g)–(i)]** before and after the corrosion test at 25°C. The GTF-1, GTF-1.5, and GTF-2 glass thick film had smooth surface before the corrosion test as shown in **Figs. 4-3(a), 4-3(d),** and **4-3(g)**. However, the cracks were observed after the GTF-1 glass thick film was immersed in a H_2SO_4 aq. for 15 min, as seen in **Fig. 4-3(b)**. The cracks became bigger, and their number increased during the immersion, as shown in **Fig. 4-3(c)**. On the basis of previous studies [10,12], it is possible that three reactions occur mainly on the glassy surface under acidic solutions: 1) ion-exchange reactions in which modifier cations are replaced by H^+ (H_3O^+), 2) hydration in which water enters the glass, and 3) hydrolysis in which water reacts with the metal-oxygen bond in the glass. These reactions occur quickly, and then fast shrinkage may happen in the GTF-1 glass thick film. The magnified SEM image of the GTF-1 glass thick film after immersed in a H_2SO_4 aq. for 15 min is shown in the inset of **Fig. 4-3(b)**. In the SEM image, the deformation was clearly observed on the surface. On the other hand, the cracks were not observed on the surface of the GTF-1.5 and GTF-2 glass thick film after immersed in a

H_2SO_4 aq., as seen in **Figs. [4-3(e)–(f)** and **4-3(h)–(i)]**. The precipitation of BSAS crystals occurred in the GTF-1.5 and GTF-2 glass thick film fired at 850°C, as shown in **Figs. 4-1(b)** and **4-1(c)**. Furthermore, the crystallinity of the AEB glass increased and the weight loss decreased as increasing the MgO powder in the glass thick films, as shown in **Fig. 4-4**. It is thought that the micro-crystals mainly improved the acid durability. On the other hand, it is reported that MgO in glasses improves water resistance so the increase of MgO in the glass can support the improvement of acid durability [7,9,24].

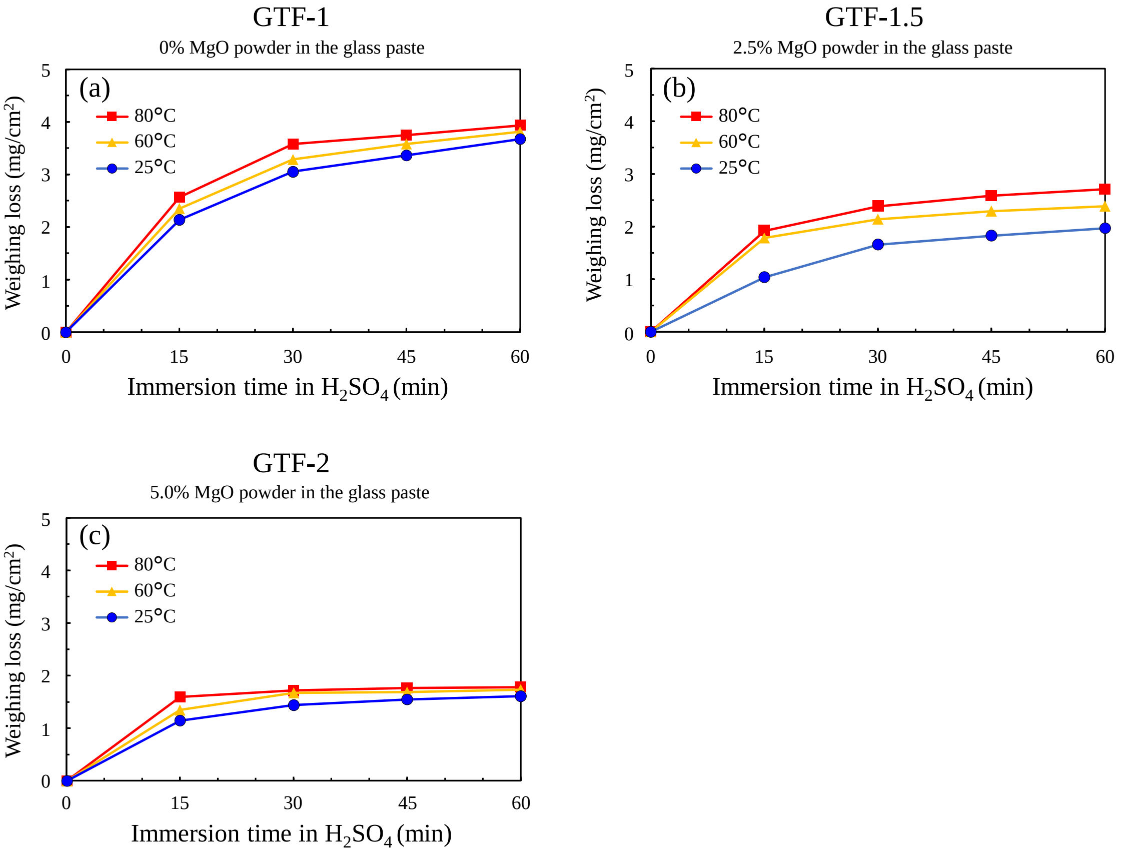

Figure 4-2. Weight loss of the glass thick films on the Al_2O_3 substrates corroded in a 1 M H_2SO_4 solution at 25°C, 60°C, and 80°C: (a) GTF-1, (b) GTF-1.5, and (c) GTF-2.

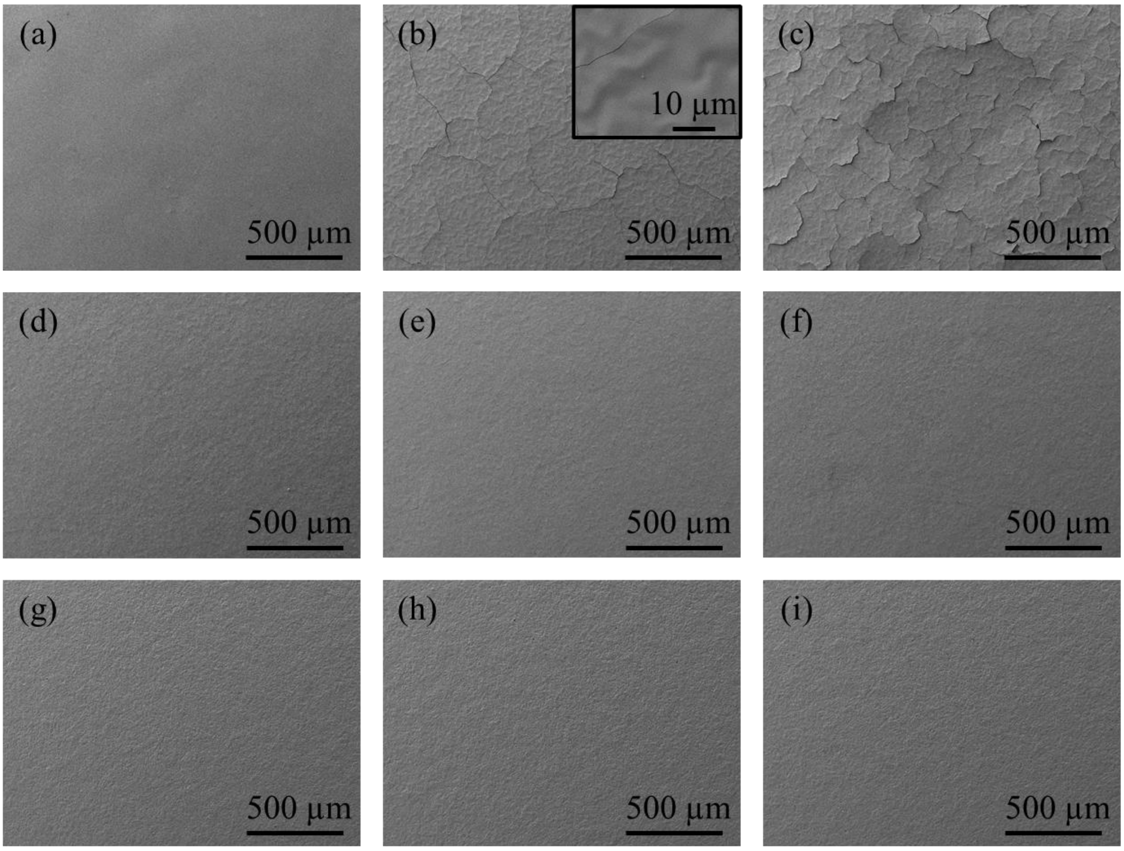

Figure 4-3. SEM images of the surface of the glass thick films immersed for different periods of time in a 1 M H_2SO_4 solution at 25°C: (a) GTF-1 for 0 min, (b) GTF-1 for 15 min, (c) GTF-1 for 60 min, (d) GTF-1.5 for 0 min, (e) GTF-1.5 for 15 min, (f) GTF-1.5 for 60 min, (g) GTF-2 for 0 min, (h) GTF-2 for 15 min, and (i) GTF-2 for 60 min.

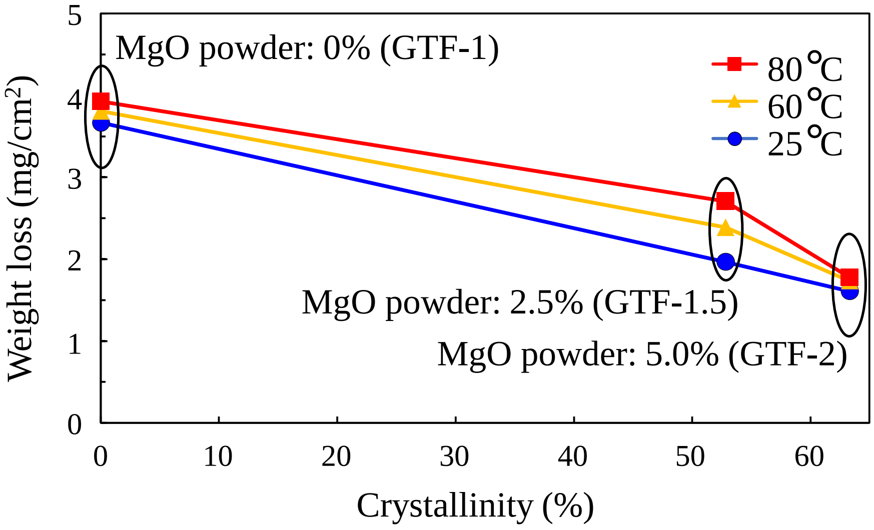

Figure 4-4. Weight loss of the glass thick films on the Al_2O_3 substrates in a 1M H_2SO_4 solution as a function of crystallinity.

4.3.3. Effect of the MgO Powder Addition to the Ag Conductor Pastes on the Structure of Glass During the Annealing Process

Figure 4-5 presents the cross-sectional SEM images of the ATF-1 **(a)** and ATF-2 Ag conductor **(b)** fired at 850°C, and the cross-sectional STEM images of the ATF-2 Ag conductor with the MgO powder addition **[(c)–(d)]**. The different contrast areas were clearly observed in the glass layer of the ATF-2 Ag conductor, whereas those were not observed in the ATF-1 Ag conductor, as shown in **Figs. 4-5(b)** and **4-5(a)**. Furthermore, as seen in the glassy region image **Fig. 4-5(d)** of the red dotted area of **Fig. 4-5(c)**, rectangular micro-crystalline particles were observed at the different contrast areas of the ATF-2 Ag conductor. It is suggested that the micro-crystallization, promoted by the addition of MgO powder to the glass pastes, happens in the ATF-2 Ag conductor, and Ag powder does not affect the micro-crystallization. These results demonstrate that the small amount of MgO powder-added to the Ag conductor paste promoted the micro-crystallization of the AEB glass. On the other hand, a further study is needed to reveal that the micro-crystals in the ATF-2 Ag conductor are the same as those in the GTF-2 glass thick film.

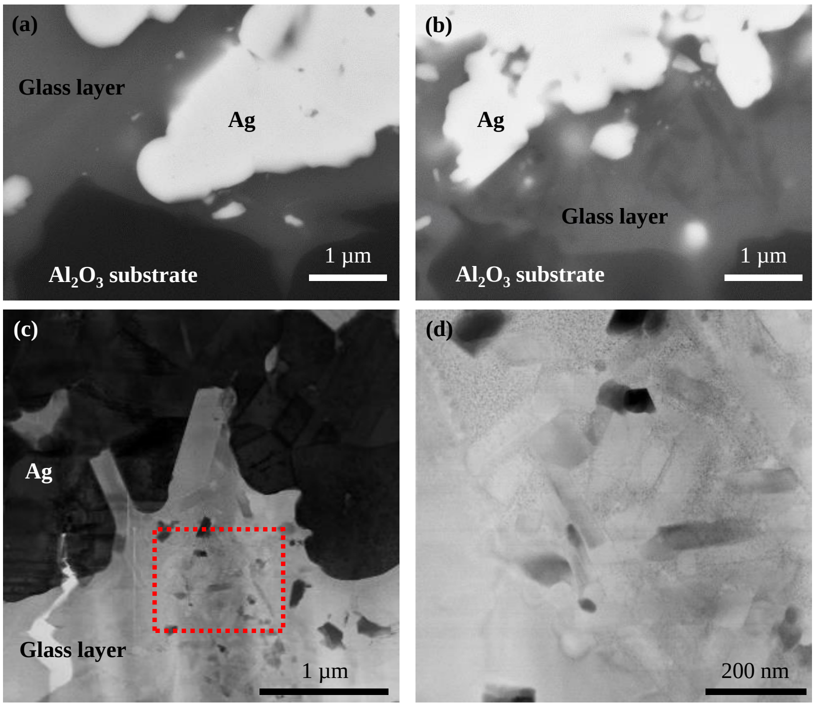

Figure 4-5. Cross-sectional SEM and STEM images of the ATF-1 and ATF-2 Ag conductor fired at 850°C: (a) SEM image of ATF-1, (b) SEM image of ATF-2, (c) BF-STEM image of ATF-2, and (d) BF-STEM image of the red dotted region in (c).

4.3.4. Acid Durability of the Ag Thick-Film Conductors

The average thickness of the Ag thick-film conductors was approximately 10 µm, and the calculated average roughness was approximately 0.7 µm. Since it was difficult to measure the weight loss of the ATF-1 and ATF-2 Ag conductor as a function of immersion time in a H_2SO_4 sq. accurately, SEM analysis was performed to observe the corrosion behavior of the Ag thick-film conductors. **Figure 4-6** presents the cross-sectional SEM images of the ATF-1 and ATF-2 Ag conductor before and after immersion in a H_2SO_4 aq. for approximate 60 min. As shown in **Figs. 4-6(a)** and **4-6(c)**, a glass layer was observed between the Ag-rich layer and Al_2O_3 substrates before the corrosion test, and glass fingers extended to the Ag-rich layer throughout the structure. This observation means that the glass-based bonding is formed in the ATF-1 and ATF-2 Ag conductor. It is known that a glass-bonded thick-film conductor typically forms a metal-rich upper layer and a glass-rich lower layer [1]. As shown in **Figs. 4-6(b)** and **4-6(d)**, after immersion in a H_2SO_4 aq., voids with low contrast appeared in the glass layer, and large voids were observed in the ATF-1 Ag conductor in comparison to the ATF-2 Ag conductor. This observation indicates that the ATF-1 Ag conductor without the added MgO powder exhibited a more corroded glass layer in comparison to the ATF-2 Ag conductor with the MgO powder addition. The H_2SO_4 aq. appears to penetrate to the Ag thick-film conductors and preferentially erode the glass layer.

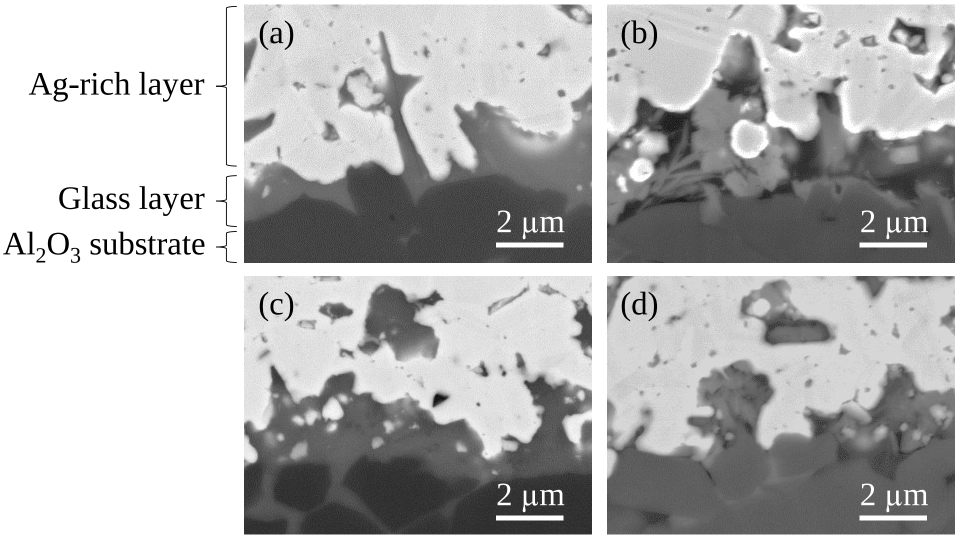

Figure 4-6. Cross-sectional SEM images of the Ag thick-film conductors immersed for different periods of time in a 1 M H_2SO_4 solution at 25°C: (a) ATF-1 for 0 min, (b) ATF-1 for 60 min, (c) ATF-2 for 0 min, and (d) ATF-2 for 60 min.

4.3.5. Peel Adhesion Characteristics of the Ag Thick-Film Conductors in an Acidic Solution

Figure 4-7 shows the peel adhesion of the Ag thick-film conductors on the Al_2O_3 substrates after immersion in a H_2SO_4 aq. for different periods of time. It is clear that the peel adhesion of the ATF-1 Ag conductor continued to decline with increasing immersion time, and it decreased to less than 1 N after 60-min immersion. However, the degree of the adhesion deterioration of the ATF-2 Ag conductor with the added MgO powder was small in comparison to the ATF-1 Ag conductor. Because the obtained adhesion greatly depends on the weakest point in the soldered Ag thick-film conductor, the breaking location needs to be taken into account when elucidating the peel adhesion behavior.

Figure 4-8 shows the photographs of the remaining Ag thick-film conductors on the Al_2O_3 substrates after the peel adhesion test. The failure mode of the ATF-1 and ATF-2 Ag conductor was not an interface failure between the Ag thick-film conductor and Al_2O_3 substrate but a cohesive failure (i.e., failure in the bulk of the adhesive layer) before immersion in a H_2SO_4 aq., as shown in **Figs. 4-8(a)** and **4-8(d)**. However, the area of the remaining Ag thick-film conductors on the Al_2O_3 substrates after acid immersion was found to be reduced with increasing immersion time, as seen in **Figs. [4-8(b)–(c)** and **4-8(e)–(f)]**. This observation indicates that the failure mode changed to delamination between the Ag thick film and Al_2O_3 substrate. The observed change in abovementioned failure mode after acid immersion was faster in the ATF-1 Ag conductor compared with the ATF-2 Ag conductor. These results suggest that the peel adhesion characteristics of the Ag thick-film conductors correspond to the acidic corrosion behavior of the glass layers in the Ag thick-film conductors.

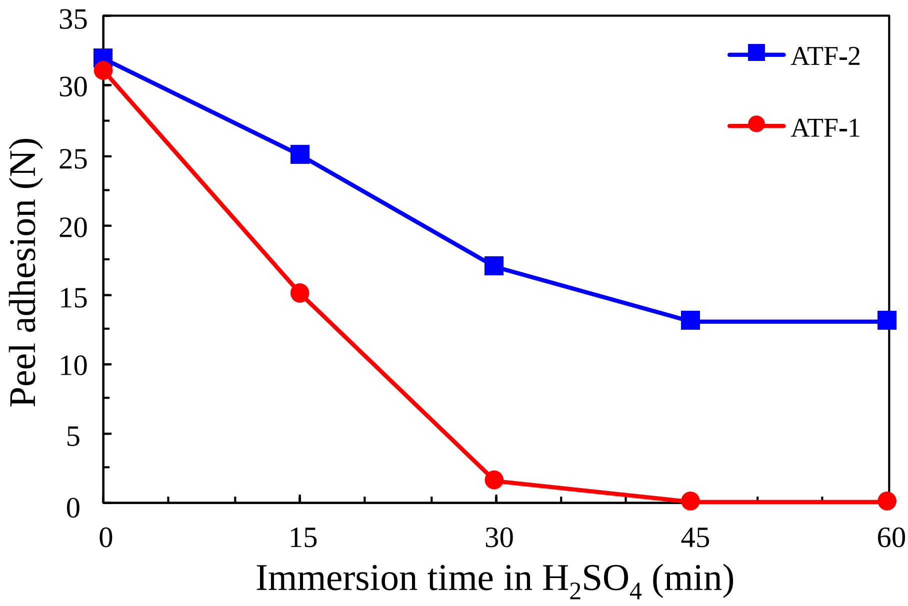

Figure 4-7. Peel adhesion of the Ag thick-film conductors on the Al_2O_3 substrates after immersion in a 1 M H_2SO_4 solution for different periods of time at 25°C.

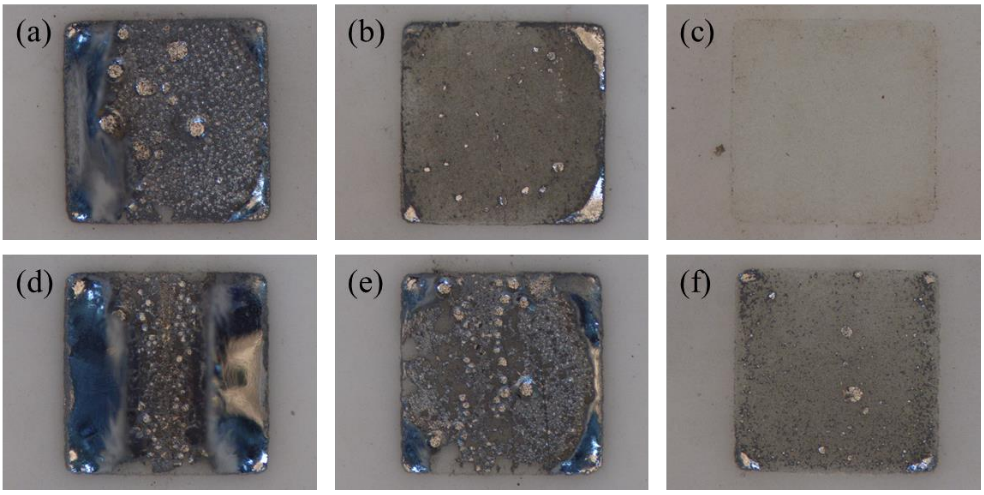

Figure 4-8. Photographs of the peel adhesion-tested Ag thick-film conductors after immersed for different periods of time in a 1 M H_2SO_4 solution at 25°C: (a) ATF-1 for 0 min, (b) ATF-1 for 15 min, (c) ATF-1 for 60 min, (d) ATF-2 for 0 min, (e) ATF-2 for 15 min, and (f) ATF-2 for 60 min.

4.3.6. Bulk Resistivity of the Ag Thick-Film Conductors

The bulk resistivity (ρ) of the ATF-1 and ATF-2 Ag conductor was estimated using Eq. 1-6 and the resistance measured using a SourceMeter (Keithley 2400, Keithley Instruments). ρ of the ATF-2 Ag conductor was 3.94 μΩ·cm, whereas that of the ATF-1 Ag conductor was 3.75 μΩ·cm. It is noted that ρ of the ATF-2 Ag conductor was approximately 5% higher than that of the ATF-1 Ag conductor. It is thought that the addition of MgO powder caused the compositional change on the Ag grain boundaries and increased the bulk resistivity slightly.

4.4. Conclusions

The MgO powder promoted the micro-crystallization of the alkali and alkaline-earth borosilicate glass on the Al_2O_3 substrates during the firing process at 850°C at the ratio of the glass frit to MgO powder = 13:1–27:1 in weight, and the precipitation of $(Ba,Sr)Al_2Si_2O_8$ crystals occurred in the glass thick films. Improved acid durability was observed for the micro-crystalized glass thick films on the basis of the weight loss characterization and SEM images after immersion in a 1 M H_2SO_4 aq. The STEM images showed the micro-crystals in the glass layer of the Ag thick-film conductor with the addition of MgO powder. This observation suggests that the micro-crystallization, promoted by the addition of MgO powder to the glass pastes, occurred in the Ag thick-film conductor. On the other hand, a further study is needed to reveal that the precipitated micro-crystals in the Ag thick-film conductor are the same as those in the glass thick films. The Ag thick-film conductor with the addition of MgO powder exhibited small corrosion behavior of the glass layer (on the basis of the SEM images), small deterioration of peel adhesion in the acidic solutions, and slow change of the failure mode in comparison to the Ag thick-film conductor without the addition of MgO powder. These results suggest that the improved acid durability of the Ag thick-film conductor is correlated with the micro-crystallization of the alkali and alkaline-earth borosilicate glass induced by the addition of MgO powder to the thick-film pastes during the firing process at 850°C. On the other hand, the addition of MgO powder to the Ag thick-film conductor slightly increased the bulk resistivity.

References

[1] J. R. Larry, R. M. Rosenberg, and R. O. Uhler, *IEEE. T. Compon. Hybr.*, **3**(2), pp.211–225 (1980).

[2] M. V. Coleman and G. E. Gurnett, *Electrocomp. Sci. Tech.*, **5**, pp.55–59 (1978).

[3] B. E. Taylor, J. J. Felten, S. J. Horowitz, J. R. Larry, and R. M. Rosenberg, *Electrocomp. Sci. Tech.*, **9**, pp.67–85 (1981).

[4] J. Savage, *Handbook of Thick Film Technology*, Eds. by P. J. Holmes and R. G. Loasby, Electrochemical Publications, Scotland, pp.97–113 (1976).

[5] C. Jiro and S. Nagahara, *Hybrids*, **2**(3), pp.2–9 (1986).

[6] R. Terai, *Mater. Integr.*, **17**(1), pp.51–55 (2004).

[7] R. Terai, *Mater. Integr.*, **17**(2), pp.55–61 (2004).

[8] Y. Kasai, *New Glass*, **21**(1), pp.36–41 (2006).

[9] M. Tanaka, T. Uwabe, Y. Ito, D. Kojima, and J. Ono, *Bulletin of TIRI*, (1), pp.50–53 (2006).

[10] B. C. Bunker, *J. Non-Cryst. Solids*, **179**, pp.300–308 (1994).

[11] F. Yanagisawa, *Min. Geol.*, **40**(5), pp.353–362 (1990).

[12] H. A. Elbatal, M. A. Azooz, E. A. Saad, F. M. EzzELDin, and M. S. Amin, *Silicon*, **10**, pp.1139–1149 (2018).

[13] M. Tashiro, S. Sakka, and T. Yamamoto, *J. Ceram. Assoc. Jpn.*, **71**(7), pp.152–157 (1963).

[14] M. Tashiro, *J. Crystallogr. Soc. Jpn.*, **8**, pp.147–156 (1966).

[15] P. F. Becher and W. L. Newell, *J. Mater. Sci.*, **12**, pp.90–96 (1977).

[16] P. F. Becher and J. S. Murday, *J. Mater. Sci.*, **12**, pp.1088–1094 (1977).

[17] T. Nakada, Y. Kaneda, K. Fukui, N. Watanabe, A. Hashimoto, and I. Koiwa, *J. Jpn. Inst. Electron. Packag.*, **16**(1), pp.66–69 (2013).

[18] K. Oyamada and K. Akiyama, *J. Surf. Finish. Soc. Jpn.*, **58**(11), pp.637–640 (2007).

[19] K. Tashiro and M. Saito, *Mekki Taizen (Handbook of Plating)*, Ed. by Kanto-gakuin University, Nikkan Kogyo Shimbun, Japan, pp.183–197 and pp.228–243 (2018) [in Japanese].

[20] T. Ishida, Y. Tsujimoto, H. Ikebe, and T. Kuroda, *Surface Mount Technology*, Eds. by I. Masuyama and T. Honda, Kogyo Chosakai Publishing, Japan, pp.15–33 and pp.65–74 (1986).

[21] Y. Tachibana, *CHIP RESISTOR*, US20180061536A1 (2018).

[22] N. P. Bansal, *J. Mater. Sci.*, **33**, pp.4711–4715 (1998).

[23] N. Takusagawa and H. Kawamura, *Inorg. Mater.*, **4**, pp.287–294 (1997).

[24] G. H. Koenderink, R. H. Brzesowsky, and A. R. Balkenende, *J. Non-Cryst. Solids*, **262**, pp.80–98 (2000).

Chapter 5

Reduction in Contact Resistivity of Ag Thick-Film Conductor on SiN_x-Coated Si Wafer Using Lead Tellurite (PT) Glass Frit

5.1. Introduction

Crystalline Si photovoltaic cells have accounted for the majority of market share of photovoltaic, and Ag-based metallization contact to Si wafers through screen printing has been used as the predominant technique due to excellent mass productivity [1–10]. In the metallization process, Ag electrodes on the Si wafer are formed by screen-printing Ag conductor pastes composed of glass frits, Ag powders, and organic vehicle onto the Si wafer and then firing them in a range of 700°C to the temperature below the silver-silicon eutectic temperature of 835°C [9–13]. Low-melting lead borosilicate glasses have been commonly used as the functional glass frits of the Ag thick-film conductors [4,8–11,14].

In the Ag conductor pastes, the lead-containing oxide glass frits are reported to etch the anti-reflective and passivation layer (about 75 nm thickness) of silicon nitride (SiN_x) coated on an emitter of the Si wafer for photovoltaic cells during the firing process, and also the melted glass frits are known to promote sintering of Ag powders [1,4,6–11,14]. After the firing process, the melted and reacted glasses form the thin glass layer between the Ag thick-film conductor and Si wafer, enabling the mechanically stable and electrically conductive contacts to develop [4,6,7,9,10,14]. Further lowering of the contact resistivity of the screen-printed Ag thick-film conductor on the SiN_x-coated Si wafer is of importance for the high photo-conversion efficiency of the photovoltaic cells. The photo-conversion efficiency of screen-printed cells is typically 1.5–2.0% lower than that of cells with photolithographically patterned metal contact, and the model calculation shows higher contact resistivity of the screen-printed cells accounts for about 10% in the loss of the efficiency [14].

Compared to lead borosilicate glasses, tellurite glasses generally possess lower melting, higher density, higher thermal expansion coefficient, as well as extreme optical properties of high refractive index, higher infrared transmittance, and higher dielectric constant [15–23]. It is also known that tellurium oxide is an atypical glass former, and the supercool process is needed to form the tellurite glass by itself [22,23]. On the other hand, the addition of a glass network modifier (NWM; e.g., Li_2O, Na_2O, K_2O, MgO, ZnO, PbO, or BaO) helps to form the tellurite glass using the conventional melt-quenching method [15,16,20–23]. In addition to these physical properties, there are many reports on the structure. **Figure 5-1** shows the typical three structures of tellurite glass. The basic structural unit in the pure tellurite glass is considered to be TeO_4 trigonal bipyramid (tbp), as shown in **Fig. 5-1(a)** [21,23,24]. In tbps, the tellurium atom is surrounded by four oxygen atoms, and all of them are bridging, while one of the sites is occupied by a lone pair of electrons. The addition of NWM stretches one of the axial bonds in TeO_4 and deforms the network structure into lower symmetry TeO_{3+1}, as shown in **Fig. 5-1(b)**. Further addition of NWM increases the non-bridging oxygen, and the network structure is deformed into TeO_3 trigonal pyramid (tp), as shown in **Fig. 5-1(c)** [21,23,24]. The structural unit of tp has three oxygen atoms connected to the tellurium atom, of which only two are bridging. Therefore, the fraction of tbps in the structure generally decreases with increasing the NWM [24].

To date, there have been numerous reports on the contact formation mechanism and the microstructure analysis of Ag thick-film conductors containing lead borosilicate glass frits as well as the viscosity of lead borosilicate glasses, the wettability on the Si wafer, and the etching behavior of SiN_x layer [4,9–11,25,26]. In contrast, few studies on the high-temperature thermal behavior of Ag thick-film conductors containing lead tellurite glass frits [12]. The purpose of Chapter 5 is to investigate the wettability, reactivity, microstructure, and electrical contact of the lead borosilicate (PS) and lead tellurite (PT) glass frit in an application for metallization contact of Ag thick-film conductors onto SiN_x-coated Si wafers for photovoltaic cells at 750°C. In addition, the correlation between the abovementioned properties and the properties of the glass frits in Chapter 3 is discussed. Furthermore, the solder leach resistance for the Ag thick-film conductors is investigated since Ag thick-film conductors on Si wafers are directly soldered in many cases [27].

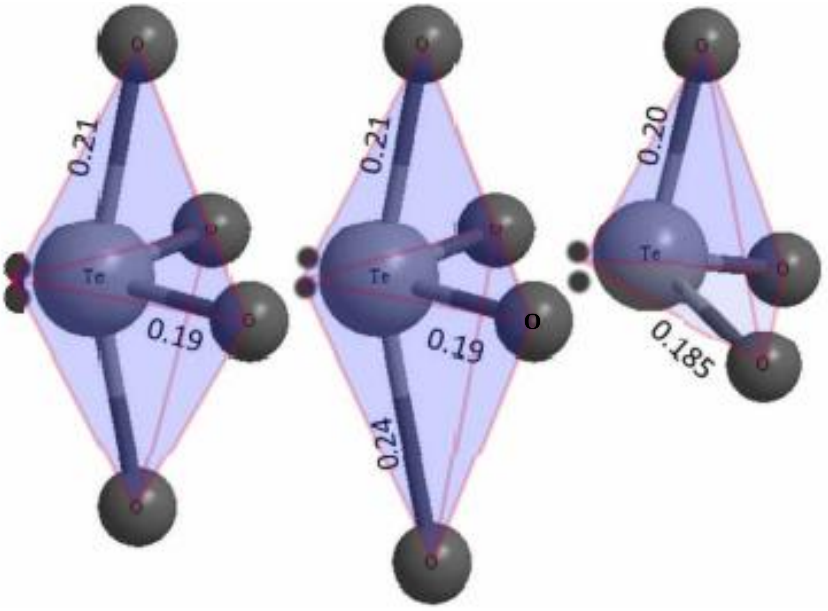

(a) TeO_4 (tbp)　(b) TeO_{3+1} (distorted tbp)　(c) TeO_3 (tp)

Figure 5-1. Ball and stick representation of the structural units present in tellurite glass: (a) trigonal bipyramidal TeO_4, (b) distorted trigonal bipyramidal TeO_{3+1}, and (c) trigonal pyramidal TeO_3. Dots represent nonbonding electrons [21].

5.2. Experimental Procedures

As shown in **Table 5-1**, two types of Ag conductor pastes were prepared by mixing the glass frit and Ag powder (average particle size of 2 μm) with an organic vehicle using a roll-milling machine. It is noted that the ATF-S Ag conductor paste contains the PS glass frit, whereas the ATF-T Ag conductor paste contains the PT glass frit. The ratio of the glass frit, Ag powder, and organic vehicle was 4.5:40:55.5 (vol.%). Generally, thick-film conductors contain metal powders 40–80 wt.% and glass frits 3–14 wt.% [28]. Since glass frits are insulation binder, adhesion of thick-film conductors on substrates decreases at low glass frit content, while bulk resistivity increases at high glass frit content. Glass frits are also needed to etch the silicon nitride on Si wafers in this study. The amount of Ag powder and glass frit is decided by considering these properties. When converted into wt.%, the ATF-S Ag conductor paste contained Ag powder 82.5 wt.% and PS glass frit 6.0 wt.%, whereas the ATF-T Ag conductor paste contained Ag powder 82.0 wt.% and PT glass frit 6.5 wt.%. The organic vehicle was composed of ethyl cellulose, terpineol, and diethylene glycol dibutyl ether. The Ag conductor pastes were screen-printed onto 25 mm × 14 mm, 190-μm-thick Si wafers with an 80-nm-thick SiN_x layer above to realize Ag metallization, as illustrated in **Fig. 2-12**. The sheet resistance of the Si wafers was examined by a contact type resistance measurement instrument (RT-3000/RG-100, Napson), and that was approximately 65 Ω/sq. The samples were dried at 150°C for 10 min to remove the volatile organic solvent and then fired at 750°C in air.

The wettability of the glass frits on the Si wafers, reactivity of these glass frits with the silicon nitride, microstructure and contact resistivity of the Ag thick-film conductors on the Si wafers were evaluated. Furthermore, the solder leach resistance was examined for these Ag thick-film conductors.

Table 5-1. Composition of the Ag conductor pastes (vol.%)

Sample name	PS glass frit	PT glass frit	Ag powder	Organic vehicle
ATF-S	4.5	-	40.0	55.5
ATF-T	-	4.5	40.0	55.5

5.3. Results and Discussion

5.3.1. Wettability of the Glass Frits on the Si Wafers

Glass pellets (φ7 mm × 1 mm) were prepared by pressing the glass frits to investigate the wetting behavior of glass melts on the Si wafers. These pellets were heated to 750°C on the Si wafers and cooled down to room temperature, and then the contact angle was measured using a contact angle meter (OCA 15EC, DataPhysics Instruments). The contact angle of the glass melts on the Si wafers in wetting measurement was approximately 14° for the PS glass, and approximately 1° for the PT glass, as shown in **Figs. 5-2(a)** and **5-2(b)**. These results suggest that the wettability of the PT glass on the Si wafer at 750°C was superior to that of the PS glass.

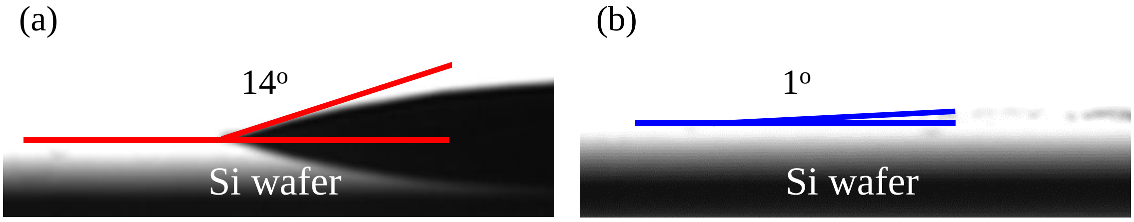

Figure 5-2. Contact angles of glass pellets on the Si wafers at 750°C: (a) PS and (b) PT.

5.3.2. Reactivity of the Glass Frits with the Silicon Nitride

To investigate the reactivity of the glass frit in the Ag conductor paste with the SiN_x layer on the Si wafer, the mixtures of Si_3N_4 powder (average particle size of 0.5 μm) and glass frit, the ratio of which was 10:1 (vol.%), were annealed at 150°C, 550°C, 600°C, 650°C, 700°C, and 750°C in air for 10 min each and then analyzed by the XRD instrument.

The XRD patterns of the Si_3N_4 powder without the glass frit were not changed before and after the annealing at 750°C, as shown in **Fig. 5-3**. This indicates that the Si_3N_4 powder is stable as high as 750°C. **Figures 5-4** shows the XRD patterns of the mixtures of Si_3N_4 powder and PS **(a)** or PT glass frit **(b)** after annealing at temperatures from 150°C up to 750°C. The crystalline diffraction peak at about 22.9° in **Figs. 5-4(a)** and **5-4(b)** is corresponding to the α-Si_3N_4 (110) plane (PDF card No. 73-1210). As shown in **Fig. 5-4(a)**, the XRD peak intensity corresponding to Si_3N_4 was almost unchanged up to 750°C, and there were observed no clear diffraction peaks except Si_3N_4 peaks by 750°C. On the other hand, the Si_3N_4 peak intensity decreased with increasing temperatures for the annealed mixtures of Si_3N_4 powder and PT glass frit, as shown in **Fig. 5-4(b)**, and interestingly above 600°C, the peak attributed to the α-cristobalite SiO_2 (101) plane (PDF card No. 39-1425) appeared at about 21.9°, and the SiO_2 peak intensity increased with increase in the annealing temperature. These changes in the XRD pattern imply the occurrence of any reaction during annealing of the mixtures of Si_3N_4 powder and PT glass frit at high temperature. The precise reaction mechanism of lead-containing oxide glass frit and SiN_x layer on the Si wafer remains in doubt, but many arguments suggest that SiN_x is oxidized by PbO in the glass by [4,26]

$$2\mathrm{PbO} + \mathrm{SiN_x} \rightarrow 2\mathrm{Pb} + \mathrm{SiO_2} + \frac{x}{2}\mathrm{N_2}. \qquad (5\text{-}1)$$

Given Eq. 5-1, SiO_2 crystal precipitation in the annealed mixtures of Si_3N_4 powder and PT glass frit, as shown in **Fig. 5-4(b)** suggests that the reaction of the Si_3N_4 powder with the PT glass frit started at approximately 600°C, and the reaction was advanced with increase in the annealing temperature. Regarding the mixture of Si_3N_4 powder and PS glass frit, in contrast, the inclusion of SiO_2 component as glass network in the glass frit is thought to suppress somewhat Eq. 5-1 producing SiO_2 as compared to the PT glass frit, and even the SiO_2 component formed in Eq. 5-1 should be incorporated into the PS glass [4,9]. These results show that the reactivity of the Si_3N_4 powder with the PT glass frit relating to Eq. 5-1 is higher than that with the PS glass frit although the Pb content in the PT glass frit is low in comparison to that in the PS glass frit.

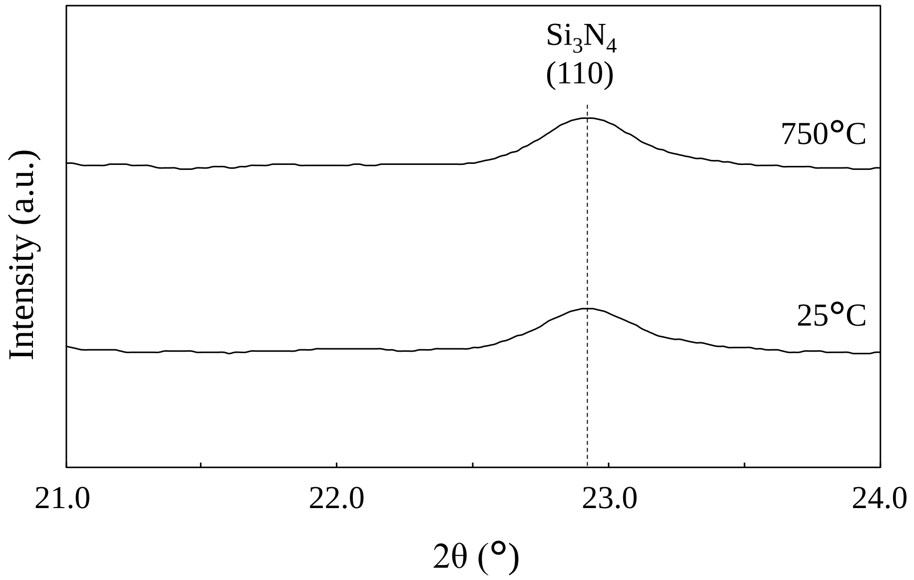

Figure 5-3. XRD patterns of the Si_3N_4 powder before and after annealing at 750°C.

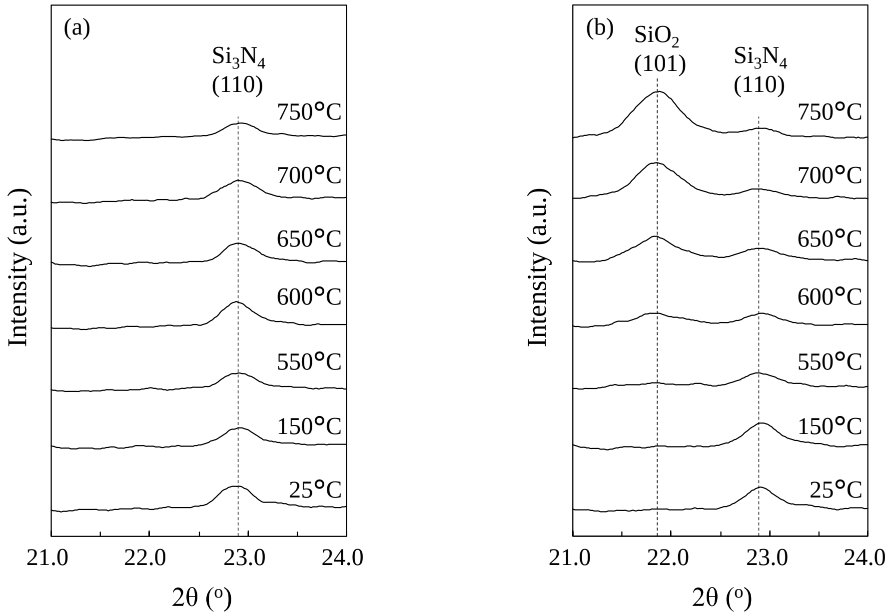

Figure 5-4. XRD patterns of the mixtures of Si_3N_4 powder and glass frits after annealing at temperatures from 150°C up to 750°C: (a) PS and (b) PT.

5.3.3. Microstructure Analysis of the Ag Thick-Film Conductors on the Si Wafers

Figure 5-5 presents the cross-sectional SEM image of the Si wafer before printing the Ag conductor paste, and the SiN_x layer with an approximate thickness of 80 nm was observed. **Figure 5-6** presents the cross-sectional SEM images of the ATF-S **(a)** and ATF-T Ag conductor **(b)** on the Si wafers. The glass layer with an approximate thickness of 0.3–0.8 μm was observed between the Ag rich layer and Si wafer for the ATF-S Ag conductor, as shown in **Fig. 5-6(a)**. The thickness of the glass layer was not uniform, but it is known that the interfacial glass layer in the thick-film conductor is generally not uniform since it is formed during the firing process through melting glass and sintering metal power [6,10,12,14,29] On the other hand, the thin glass layer with approximately 80–150 nm thickness was observed for the ATF-T Ag conductor in a wide observation range, as shown in **Fig. 5-6(b)**. The glass transition temperature of the PT glass frit was approximately 230°C, and the viscosity of the PT glass melt was less than 1 Pa·s at 650°C or higher, as discussed in **Figs. 3-5(b),** and **3-7**. In addition, the wettability of the PT glass on the Si wafer at 750°C was superior to that of the PS glass, as discussed in Subsection 5.3.1. The results suggest that these properties enabled to form such thin glass layer in the ATF-T Ag conductor. **Figure 5-7** has a magnification 10 times greater than **Fig. 5-6**. In the ATF-S and ATF-T Ag conductor, the SiN_x layer was not observed underneath the glass layer, as shown in **Figs. 5-7(a)** and **5-7(b)**. It suggests that the SiN_x layers on the Si wafers were etched away by the glass frits in both Ag thick-film conductors. Although the reactivity of the PS glass frit with the Si_3N_4 powder was low as discussed in **Fig. 5-4(a)**, it is thought that the SiN_x layer was etched away since the Ag powder in the ATF-S Ag conductor assisted the etching as previously reported that Ag dissolves into the glass during the firing of Ag thick-film conductor, and then Ag ions are reduced to Ag due to a redox reaction with the SiN_x layer [4,27]. Ag crystal particles with a size of about 50 nm were observed in the glass layers of the ATF-S and ATF-T Ag conductor, and those were close to the Si wafers, as shown in **Figs. 5-7(a)** and **5-7(b)**. It is reported that Ag dissolves in the glass during the firing process, and the solubility of Ag in the melted glass decreases as it cools down from the firing peak temperature, and Ag nanocrystals precipitate within the glass layer [4,14]. Ag dissolved in the melted glass oxidizes Si to SiO_2 and then the Ag crystals precipitate and grow on the emitter surface of the Si wafer [4,9,10,14]. The number of Ag crystal particles in the glass layer of the ATF-T Ag conductor was less than that of the ATF-S Ag conductor.

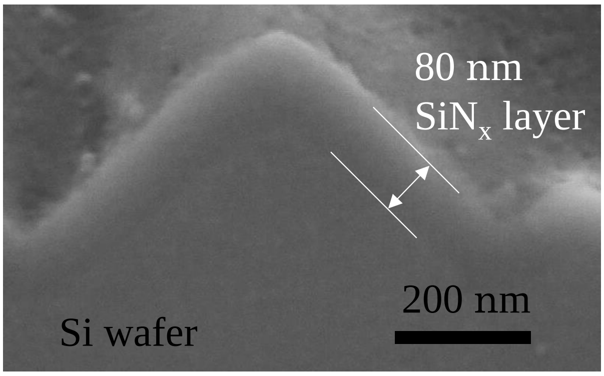

Figure 5-5. Cross-sectional SEM image of the Si wafer before printing the Ag conductor paste.

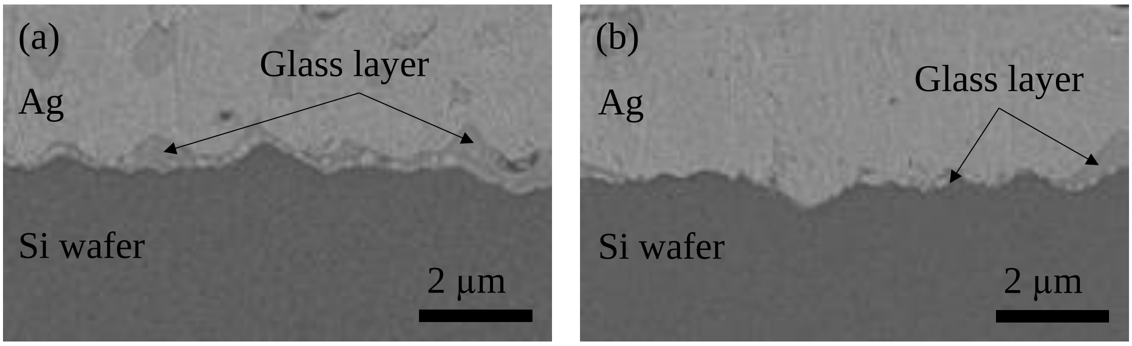

Figure 5-6. Cross-sectional SEM images of the Ag thick-film conductors on the Si wafers fired at 750°C: (a) ATF-S and (b) ATF-T.

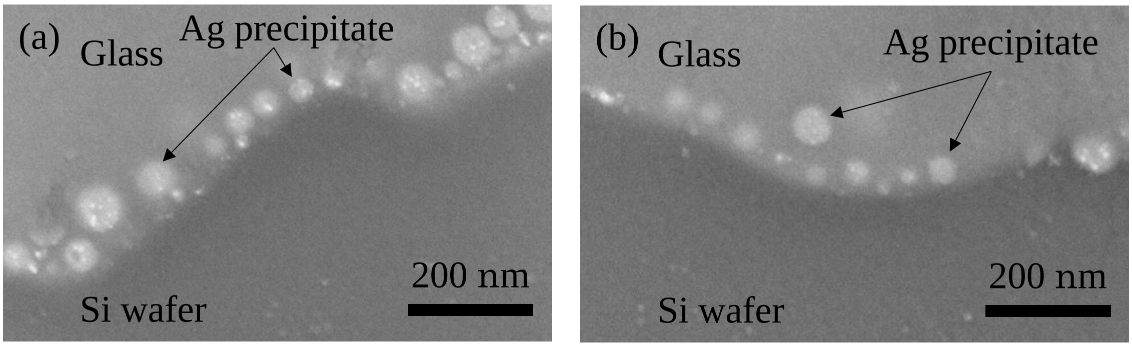

Figure 5-7. Cross-sectional high magnification SEM images of the Ag thick-film conductors on the Si wafers fired at 750°C: (a) ATF-S and (b) ATF-T.

5.3.4. Contact Resistivity of the Ag Thick-Film Conductors on the Si Wafers

The average thickness of the Ag thick-film conductors was approximately 15 μm, and the calculated average roughness was approximately 0.6 μm. **Figure 5-8** shows the TLM calculated total resistance (R_T) plotted as a function of the distance (L) between two Ag thick-film conductors for the ATF-S and ATF-T Ag conductor fired at 750°C. The substantial fill marks are the measured values, and the dashed lines are drawn from a calculation using the least-squares method [30]. The statistical determination coefficients (R^2) for the dashed lines were approximately 1.00, as shown in **Table 5-2**, meaning that the lines fitted well to the measurement values. The contact resistance (R_c) of the ATF-S Ag conductor was estimated at 1.56 Ω, whereas that of the ATF-T Ag conductor was 0.25 Ω. The sheet resistances of the Si wafers estimated using Eq. 2-7 from the slop of the dashed lines in **Fig. 5-8** were both approximately 50 Ω/sq., which was lower than the measured value of 65 Ω/sq. Since it is possible that some of the current find a path of low resistance through the structure along the edge of the sample, it is thought that the effect of the edge shunt increases as increasing the distance between Ag thick-film conductors, as a result, the slope becomes low in the TLM [31]. The contact resistivity (ρ_c) was estimated using Eq. 2-9 from the x-intercept and y-intercept of the dashed line in **Fig. 5-8**. ρ_c of the ATF-S Ag conductor was estimated at 52.0 mΩ·cm^2, whereas that of the ATF-T Ag conductor was 1.32 mΩ·cm^2. Thus, the contact resistivity of the Ag thick-film conductor containing the PT glass frit was found to be less than one-tenth of that containing the PS glass frit. Generally, the electrical current between the Ag thick-film conductor and emitter of Si wafer is supposed to be transmitted through three possible channels: 1) direct interconnection between the Ag and emitter, 2) tunneling through the ultra-thin glass layer between the Ag and emitter, and 3) conduction through the glass layer via multi-step tunneling from Ag to Ag particle within the glass layer [4–6,9,10,14]. In the ATF-T Ag conductor containing the PT glass frit, the direct interconnection between the Ag and emitter was not observed in a wide observation range, and the number of Ag crystal particles in the glass layer of the ATF-T Ag conductor was less than that of the ATF-S Ag conductor, as shown in **Figs. 5-7(b)** and **5-7(a)**. On the other hand, the formation of the thinner glass layer on the Si wafer occurred in the ATF-T Ag conductor after etching the $\mathrm{SiN_x}$ layer, as shown in **Fig. 5-6(b)**. Therefore, it is thought the formation of thin glass layer resulted in low contact resistivity of the ATF-T Ag conductor.

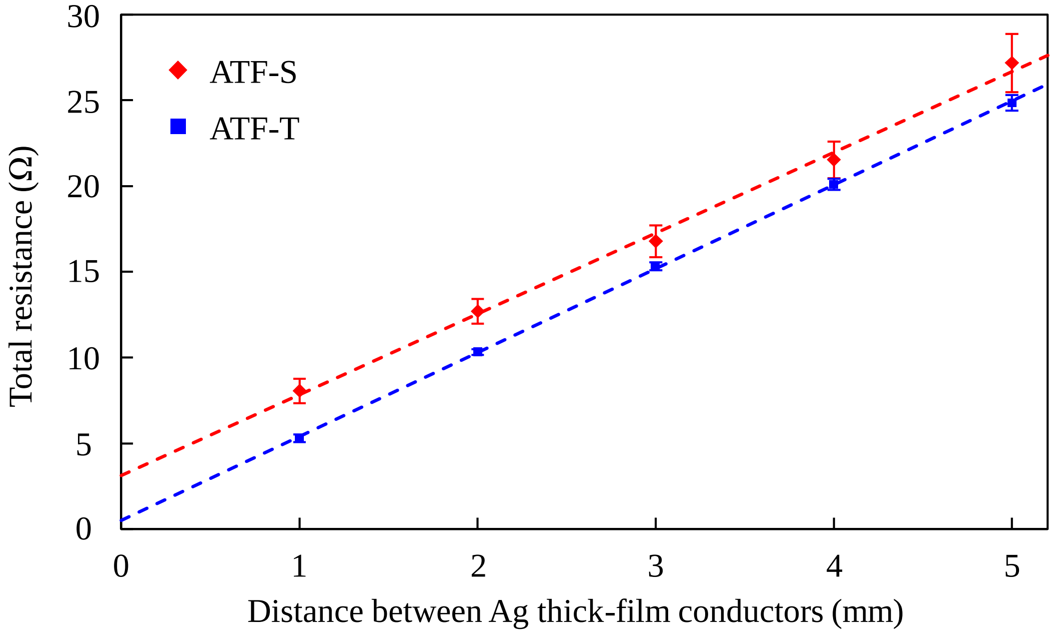

Figure 5-8. Total resistance as a function of the distance between the Ag thick-film conductors of ATF-S and ATF-T fired at 750°C.

Table 5-2. TLM results for the Ag thick-film conductors

Sample name	R^2	R_c (Ω)	ρ_c (mΩ·cm^2)
ATF-S	1.00	1.56	52.0
ATF-T	1.00	0.25	1.32

5.3.5. Solder Leach Resistance of the Ag Thick-Film Conductors on the Si Wafers

Figure 5-9 shows the resistance change ratio (ΔR) of the ATF-S and ATF-T Ag conductor as a function of dipping time in the solder. ΔR of both Ag thick-film conductors increased as increasing the dipping time at 220°C and 240°C, and that was accelerated at high temperature, as shown in **Figs. 5-9(a)** and **5-9(b)**. It is noted that ΔR of the ATF-S and ATF-T Ag conductor was approximately 1.0 at 200°C for 15 s, whereas ΔR of the ATF-S and ATF-T Ag conductor was approximately 2.8 at 240°C for 60 s. It is known that the Ag dissolution rate in the solder is faster as increasing the temperature [32]. These results suggest that the solder reach resistance can be controlled by the soldering temperature and time. The clear difference in ΔR was not observed between the ATF-S and ATF-T Ag conductor. The observation means that the solder leach resistance of the ATF-T Ag conductor was nearly equal to that of the ATF-S Ag conductor.

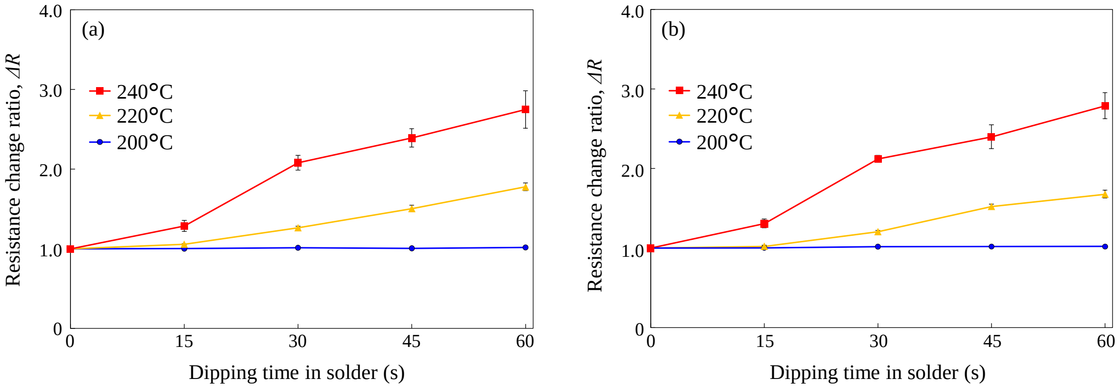

Figure 5-9. Resistance change ratio of the Ag thick-film conductors in the solder at 200°C, 220°C, and 240°C: (a) ATF-S and (b) ATF-T.

5.4. Conclusions

At the interface between the Ag thick-film conductor and Si wafer after the firing process at 750°C, cross-sectional SEM images showed the thin glass layer in the Ag thick-film conductor containing the lead tellurite glass frit. The glass transition temperature of the lead tellurite glass frit was approximately 230°C, and the viscosity of the lead tellurite glass melt was less than 1 Pa·s at 650°C or higher in Chapter 3. In addition, the wettability of the lead tellurite glass on the Si wafer at 750°C was superior to that of the lead borosilicate glass. The results suggest that these properties of the lead tellurite glass frit enabled to form such thin glass layer in the Ag thick-film conductor. The reactivity of the silicon nitride with the lead tellurite glass frit was higher than that with the lead borosilicate glass frit although the Pb content in the lead tellurite glass frit was low in comparison to that in the lead borosilicate glass frit. At the ratio of the Ag powder to glass frit = 9:1 in volume, the contact resistivity of the Ag thick-film conductor containing the lead tellurite glass frit on the Si wafer was estimated at 1.32 $m\Omega\cdot cm^2$ from the transfer length method, which was less than one-tenth of the value for the Ag thick-film conductor containing the lead borosilicate glass frit. The high reactivity of the SiN_x layer with the lead tellurite glass frit and the formation of the thin glass layer finally enabled it to achieve better conductive contacts. The resistance increased as increasing the dipping time in the solder, and the solder leach was accelerated for the Ag thick-film conductors at high temperature. On the other hand, the solder leach resistance of the Ag thick-film conductor containing the lead tellurite glass frit was nearly equal to that containing the lead borosilicate glass frit.

References

[1] T. Kamioka, T. Tachibana, and Y. Ohshita, *J. Plasma Fusion Res.*, **91**(5), pp.354–359 (2015).

[2] A. J. Waldau, *PV Status Report 2019*, European Union, Luxembourg, pp.5–9 (2019).

[3] T. Ibn-Mohammed, S. C. L. Koh, I. M. Reaney, A. Acquaye, G. Schileo, K. B. Mustapha, and R. Greenough, *Renew. Sustain. Energy Rev.*, **80**, pp.1321–1344 (2017).

[4] J. D. Fields, M. I. Ahmad, V. L. Pool, J. Yu, D. G. Van Campen, P. A. Parilla, M. F. Toney, and M. F. A. M. van Hest, *Nat. Commun.*, **7**, 11143 (2016).

[5] G. Beaucarne, G. Schubert, and J. Hoornstra, *Energy Procedia*, **67**, pp.2–12 (2015).

[6] R. Hoenig, M. Duerrschnabel, W. V. Mierlo, Z. Aabdin, J. Bernhard, J. Biskupek, O. Eibl, U. Kaiser, J. Wilde, F. Clement, and D. Biro, *Energy Procedia*, **43**, pp.27–36 (2013).

[7] V. Shanmugam, J. Cunnusamy, A. Khanna, M. B. Boreland, and T. Mueller, *Energy Procedia*, **33**, pp.64–69 (2013).

[8] Y. Yang, S. Seyedmohammadi, U. Kumar, D. Gnizak, E. Graddy, and A. Shaikn, *Energy Procedia*, **8**, pp.607–613 (2011).

[9] G. Schubert, F. Huster, and P. Fath, *Sol. Energy Mater Sol. Cells*, **90**, pp.3399–3406 (2006).

[10] C. Ballif, D. M. Huljic, G. Willeke, and A. Hesseler-Wyser, *Appl. Phys. Lett.*, **82**(12), pp.1878–1880 (2003).

[11] G. Schubert, B. Fischer, and P. Fath, presented at *PV in Europe - From PV Technology to Energy Solutions* (2002).

[12] S. Watanabe, T. Kodera, and T. Ogihara, *J. Ceram. Soc. Jpn.*, **124**(3), pp.218–222 (2016).

[13] H. Okamoto, *Phase Diagrams for Binary Alloys*, Eds. by M. A. Fleming and C. McNeill, ASM International, USA, p19 (2000).

[14] M. M. Hilali, B. To, and A. Rohatgi, presented at *14th Workshop on Crystalline Silicon Solar Cells & Modules: Materials and Processes*, pp.109–116 (2004).

[15] M. Imaoka and T. Yamazaki, *J. Ceram. Assoc. Jpn.*, **76**(5), pp.160–172 (1968).

[16] H. Tokunaga, S. Haruki, S. Sukenaga, N. Saito, and K. Nakashima, *J. Jpn. Inst. Met.*, **74**(5), pp.331–336 (2010).

[17] J. E. Stanworth, *Nature*, **169**, pp.581–582 (1952).

[18] X. Feng, A. K. Mairaj, D. W. Hewak, and T. M. Monro, *J. Lightwave Technol.*, **23**(6), pp.2046–2054 (2005).

[19] Y. Asahara, *New Glass Handbook*, Eds. by T. Sakaino, Y. Asahara, K. Arai, S. Ito, S. Inoue, S. Takahashi, K. Nishizawa, A. Makishima, I. Yasui, and M. Yamane, Maruzen Publishing, Japan, pp.306–308 (1991).

[20] S. Tsuchihashi, *Chemistry of Glass*, Kodansha, Japan, pp.89–90 (1988).

[21] S. Manning, H. Ebendorff-Heidepriem, and T. M. Monro, *Opt. Mater. Express*, **2**(2), pp.140–152 (2012).

[22] K. Tanaka, K. Kashima, K. Kajihara, K. Hirao, N. Soga, A. Mito, and H. Nasu, *J. Jpn. Soc. Powder Powder Metall.*, **42**(1), pp.55–60 (1995).

[23] S. Sakida, *New Glass*, **27**(104), pp.14–20 (2012).

[24] J. Kieffer, J. A. Johnson, O. Nickolayev, and J. D. Bass, *J. Phys.: Condens. Matter.*, **18**, pp.903–914 (2006).

[25] F. Imoto and K. Hirao, *J. Ceram. Assoc. Jpn.*, **67**(11), pp.381–385 (1959).

[26] M. Horteis, T. Gutberlet, A. Reller, and S. W. Glunz, *Adv. Funct. Mater.*, **20**, pp.476–484 (2010).

[27] R. Hoenig, *Dr. Thesis*, Faculty of Engineering, Albert-Ludwigs-Universität Freiburg, Germany (2014).

[28] Y. Tachibana, *CHIP RESISTOR*, US20180061536A1 (2018).

[29] Y. Shih, Y. Lin, J. You, and F. G. Shi, *J. Electron. Mater.*, **42**(3), pp.410–416 (2013).

[30] S. J. Miller, *The Method of Least Squares*, Brown University, USA, pp.1–7 (2006).

[31] A. M. Gabor, G. Gregory, A. M. Payne, R. Janoch, A. Anselmo, V. Yelundur, and K. O. Davis, presented at *the 43rd IEEE Photovoltaic Specialists Conf.*, pp.1–4 (2016).

[32] T. Osawa, *J. Japan Inst. Electron. Packag.*, **5**(3), pp.304–309 (2002).

Chapter 6

General Conclusion

Glass frits in conductor pastes promote the sintering of metal powders during the firing process and binding of the metal film to the substrate. Therefore, low-melting glasses are suitable for thick-film conductors, and lead borosilicate glasses have been extensively used. Recently, material design with Sustainable Development Goals (SDGs) is becoming important, and further function control of thick-film conductors is required. This study took the Pb-free request for environment and health in Chapter 4 and the request of photovoltaic cells as renewable source of energy in Chapter 5. In Chapter 4, Pb-free electronic materials are environmentally required but that makes a problem of acid durability of electroplated Ag thick-film conductors in acidic solutions. This study found the correlation between the acid durability of the Ag thick-film conductors and that of the glass frits by the weight loss characterization of the glasses, SEM images, peel adhesion, and its failure mode analysis of the Ag thick-film conductors on the Al_2O_3 substrates in the acidic solutions. Furthermore, this study found that the micro-crystallization of the alkali and alkaline-earth borosilicate glass was promoted by the addition of MgO powder in the thick films at 850°C at the ratio of the glass frit to MgO powder = 13:1–27:1 in weight, and the micro-crystallized glass improved the acid durability of the Ag thick-film conductor. New underlaying technology was built for Pb-free Ag thick-film conductors with strong acid durability by promoting the micro-crystallization of the low-melting alkali and alkaline-earth borosilicate glass by using the MgO powder in the thick-film conductors during the firing process. In Chapter 5, it is still difficult to remove Pb in Ag thick-film conductors for photovoltaic cells, while further lowering of the contact resistivity on SiN_x-coated Si wafers is required for Ag thick-film conductors to improve the photo-conversion efficiency and increase the renewable source of energy. This study found that the thickness of the interfacial glass layer significantly affected the contact resistivity of the Ag thick-film conductors on the Si wafers by the SEM images of the Ag thick-film conductors containing the lead borosilicate glass frit or the lead tellurite glass frit, and the reactivity test of the silicon nitride and each glass frit using the XRD instrument. The low viscosity of the lead tellurite glass melt and its good wettability on the Si wafer enabled to form the thin glass layer in the Ag thick-film conductor at 750°C. Furthermore, the reactivity of the silicon nitride with the lead tellurite glass frit was high. As a result, the contact resistivity of the Ag thick-film conductor containing the lead tellurite glass frit on the Si wafer was less than one-tenth of the value for the Ag thick-film conductor containing the lead borosilicate glass frit at 750°C at the ratio of the Ag powder to glass frit = 9:1 in volume in the transfer length method. New underlying technology was built for Ag thick-film conductors giving low contact resistivity on SiN_x-coated Si wafers by forming the thin interfacial glass layer after the reaction with the silicon nitride by using the lead tellurite glass frit with low melt viscosity and good wettability on the Si wafers. As a future perspective, it is needed to design Ag thick-film conductors without Pb and Te to meet SDGs further. The detailed summary of the studies is explained in the below paragraphs.

In Chapter 4, this study found that the MgO powder promoted the micro-crystallization of the alkali and alkaline-earth borosilicate glass on the Al_2O_3 substrates during the firing process at 850°C at the ratio of the glass frit to MgO powder = 13:1–27:1 in weight, and the precipitation of $(Ba,Sr)Al_2Si_2O_8$ crystals occurred in the glass thick films. Improved acid durability was observed for the micro-crystalized glass thick films on the basis of the weight loss characterization and SEM images after immersion in a 1 M H_2SO_4 aq. The STEM images showed the micro-crystals in the glass layer of the Ag thick-film conductor with the addition of MgO powder. This observation suggests that the micro-crystallization, promoted by the addition of MgO powder to the glass pastes, occurred in the Ag thick-film conductor. On the other hand, a further study is needed to reveal that the precipitated micro-crystals in the Ag thick-film conductor are the same as those in the glass thick films. The Ag thick-film conductor with the addition of MgO powder exhibited small corrosion behavior of the glass layer (on the basis of the SEM images), small deterioration of peel adhesion in the acidic solutions, and slow change of the failure mode in comparison to the Ag thick-film conductor without the addition of MgO powder. These results suggest that the improved acid durability of the Ag thick-film conductor is correlated with the micro-crystallization of the alkali and alkaline-earth borosilicate glass induced by the addition of MgO powder to the thick-film pastes during the firing process at 850°C. On the other hand, the addition of MgO powder to the Ag thick-film conductor slightly increased the bulk resistivity.

In Chapter 5, at the interface between the Ag thick-film conductor and Si wafer after the firing process at 750°C, cross-sectional SEM images showed the thin glass layer in the Ag thick-film conductor containing the lead tellurite glass frit. The glass transition temperature of the lead tellurite glass frit was approximately 230°C, and the viscosity of the lead tellurite glass melt was less than 1 Pa·s at 650°C or higher in Chapter 3. In addition, the wettability of the lead tellurite glass on the Si wafer at 750°C was superior to that of the lead borosilicate glass. The results suggest that these properties of the lead tellurite glass frit enabled to form such thin glass layer in the Ag thick-film conductor. The reactivity of the silicon nitride with the lead tellurite glass frit was higher than that with the lead borosilicate glass frit although the Pb content in the lead tellurite glass frit was low in comparison to that in the lead borosilicate glass frit. At the ratio of the Ag powder to glass frit = 9:1 in volume, the contact resistivity of the Ag thick-film conductor containing the lead tellurite glass frit on the Si wafer was estimated at 1.32 $\mathrm{m\Omega \cdot cm^2}$ from the transfer length method, which was less than one-tenth of the value for the Ag thick-film conductor containing the lead borosilicate glass frit. The high reactivity of the SiN_x layer with the lead tellurite glass frit and the formation of the thin glass layer finally enabled it to achieve better conductive contacts. The resistance increased as increasing the dipping time in the solder, and the solder leach was accelerated for the Ag thick-film conductors at high temperature. On the other hand, the solder leach resistance of the Ag thick-film conductor containing the lead tellurite glass frit was nearly equal to that containing the lead borosilicate glass frit.

To control the chemical durability and electrical properties of Ag thick-film conductors, it is important to control the properties of glass frits such as micro-crystallization, glass transition temperature, and melt viscosity, and to combine proper compositions.

Research Achievements

Journal publication:

- **Yusuke Tachibana**, Akifumi Matsuda, and Mamoru Yoshimoto, *J. Ceram. Soc. Jpn.*, **128**(3), pp.142-148, DOI: 10.2109/jcersj2.19157 (2020). – This study is included in Chapter 3 and 4.
- **Yusuke Tachibana**, Akifumi Matsuda, and Mamoru Yoshimoto, *Jpn. J. Appl. Phys.*, **59**(9), 090908, DOI: 10.35848/1347-4065/abaebb (2020). – This study is included in Chapter 3 and 5.

Conference presentation:

- **Yusuke Tachibana**, Akifumi Matsuda, and Mamoru Yoshimoto, *Effect of MgO powder addition to alkali and alkaline-earth borosilicate glass paste on the acid durability and peel adhesion characteristics of Ag conductors formed with the glass paste*, The 33rd Fall meeting hosted by The Ceramic Society of Japan (2020).

Patent publication about thick-film conductor pastes

- Esther Kim, Brian J Laughlin, Kurt Richard Mikeska, **Yusuke Tachibana**, and Paul Douglas VerNooy, *CONDUCTIVE PASTE USED FOR SOLAR CELL ELECTRODES*, US9761348 B2.
- Kenneth Warren Hang, Kathryn Lynn Goetschius, **Yusuke Tachibana**, and Paul Douglas VerNooy, *CONDUCTIVE PASTE COMPOSITION AND SEMICONDUCTOR DEVICES MADE THEREWITH*, US10134925 B2.
- Mamoru Murakami and **Yusuke Tachibana**, *CHIP RESISTOR*, US10115505 B2.
- **Yusuke Tachibana**, *CHIP RESISTOR*, US20180061536 A1 (CN107785138 B).

Acknowledgments

This work has been a truly life-changing experience for me, and it would not have been possible without the support and guidance that I received from many people.

I would first like to express my appreciation to my adviser Prof. **Mamoru Yoshimoto** for all the support and encouragement he gave me. His guidance and constant feedback helped me to write this thesis. I cannot imagine a better adviser for my study in the PhD course. He was a chief examiner of this thesis.

I am grateful to Senior Lecturer **Akifumi Matsuda** for his continuous support and thoughtful advice in the PhD course. He was a sub-chief examiner of this thesis.

I would also like to acknowledge with appreciation thoughtful guidance of Prof. **Hiroshi Funakubo**, Prof. **Yoshitaka Kitamoto**, and Associate Prof. **Hiroyuki Wada** who were examiners of this thesis.

This work would not have been possible without the support and corporation with DuPont group. I am indebted to **Tsutomu Mutoh** who has been supportive of my goals. I also would like to express my gratitude to **Hiroaki Noda** for always encouraging me.

I gratefully acknowledge the work of past and present project members. My deepest appreciation goes to **Mamoru Murakami** for his insightful comments and hard questions. The advice from him was very helpful. I am grateful to **Toshifumi Fujii** for his support and encouragement. I would also like to thank the assistance given by **Mari Ishii** and **Emi Yasuda**. Their excellent work made an invaluable contribution to this thesis.

Finally, I would like to express my very profound gratitude to my parents: **Kimito Tachibana** and **Kumiko Tachibana**, my wife: **Yumi Tachibana**, and my child: **Yusei Tachibana** for providing me with unfailing support and continuous encouragement.

Yusuke Tachibana
February 2022